# TRION-BASED OPTICAL PROCESSES IN SEMICONDUCTOR QUANTUM WELLS

by

THOMAS KENDRICK BALDWIN

A DISSERTATION

Presented to the Department of Physics
and the Graduate School of the University of Oregon
in partial fulfillment of the requirements
for the degree of
Doctor of Philosophy

December 2015

DISSERTATION APPROVAL PAGE

Student: Thomas Kendrick Baldwin

Title: Trion-based Optical Processes in Semiconductor Quantum Wells

This dissertation has been accepted and approved in partial fulfillment of the requirements for the Doctor of Philosophy degree in the Department of Physics by:

| | |
|---|---|
| Daniel A. Steck | Chair |
| Hailin Wang | Advisor |
| Dietrich Belitz | Core Member |
| George Nazin | Institutional Representative |

and

| | |
|---|---|
| Scott L. Pratt | Dean of the Graduate School |

Original approval signatures are on file with the University of Oregon Graduate School.

Degree awarded December 2015

DISSERTATION ABSTRACT

Thomas Kendrick Baldwin

Doctor of Philosophy

Department of Physics

December 2015

Title: Trion-based Optical Processes in Semiconductor Quantum Wells

In a semiconductor, negative charge is carried by conduction-band electrons and positive charge is carried by valence-band holes. While charge transport properties can be understood by considering the motion of these carriers individually, the optical properties are largely determined by their mutual interaction. The hydrogen-like bound state of an electron with a hole, or exciton, is the fundamental optical excitation in direct-gap materials such as gallium arsenide (GaAs) and cadmium telluride (CdTe).

In this dissertation, we consider charged excitons, or trions. A bound state of an exciton with a resident electron or hole, trions are a relatively pure manifestation of the three-body problem which can be studied experimentally. This is a subject of practical as well as academic interest: Since the trion is the elementary optical excitation of a resident free carrier, the related optical processes can open pathways for manipulating carrier spin and carrier transport.

We present three experimental investigations of trion-based optical processes in semiconductor quantum wells. In the first, we demonstrate electromagnetically induced transparency via the electron spin coherence made possible by the trion transition. We explore the practical limits of this technique in high magnetic fields. In the second, we present a direct measurement of trion and exciton oscillator strength at high magnetic fields. These data reveal insights about the structure of the trion's three-body wavefunction relative to that of its next excited state, the triplet trion. In the last, we investigate the mechanism underlying exciton-correlated tunneling, an optically-controllable transport process in mixed-type quantum wells. Extensive experimental studies indicate that it is due to a local, indirect interaction between an exciton and a hole, forming one more example of a trion-mediated optical process.

This dissertation includes previously published co-authored material.

CURRICULUM VITAE

NAME OF AUTHOR: Thomas Kendrick Baldwin

GRADUATE AND UNDERGRADUATE SCHOOLS ATTENDED:

University of Oregon, Eugene, OR
Grinnell College, Grinnell, IA
Albert-Ludwigs Universität, Freiburg, Germany

DEGREES AWARDED:

Doctor of Philosophy in Physics, 2015, University of Oregon
Bachelor of Arts in Physics, 2008, Grinnell College

AREAS OF SPECIAL INTEREST:

Optics of low-dimensional semiconductor systems (wells and dots). Quantum information hardware, especially diamond nitrogen vacancy centers.

PROFESSIONAL EXPERIENCE:

Research Assistant, Hailin Wang, Department of Physics, University of Oregon, 2008-2015

Teaching Assistant, Department of Physics, University of Oregon, 2008-2010, 2015

Technical Student Intern, Carlos Ruiz, Sandia National Laboratories, 2004-2005

GRANTS, AWARDS AND HONORS:

Science Literacy Program Fellow, Department of Physics, University of Oregon, 2015

National Science Foundation GK-12 Fellow, Materials Science Institute, University of Oregon, 2010-2012

Summer Undergraduate Research Fellow, Kevin Silverman, National Institute of Standards and Technology, 2008

Summer Undergraduate Research Fellow, Pavel Kabos, National Institute of Standards and Technology, 2006

PUBLICATIONS:

D. A. Golter, T. K. Baldwin, and H. Wang, "Protecting a solid-state spin from decoherence using dressed spin states", Physical Review Letters **113**, 237601 (2014)

T. K. Baldwin, C. Phelps, H. Wang, and J. P. Prineas, "Persistence of trions and quenching of excitons in optically induced two-dimensional electron gases in mixed-type GaAs/AlAs quantum wells", Journal of the Optical Society of America B **31**, 3138 (2014)

T. K. Baldwin, S. A. McGill, and H. Wang, "Exciton-correlated hole tunneling in mixed-type GaAs quantum wells", Physical Review B **90**, 035304 (2014)

D. Golter, T. K. Baldwin, and H. Wang, "Suppression of Spin Dephasing in Diamond NV Centers with Microwave-Dressed Spin States", in Conference on Lasers and Electro-Optics 2014 (2014), FW1B.3

T. K. Baldwin, S. McGill, and H. Wang, "Manybody-Correlated Tunneling in Mixed-Type Quantum Wells at High Magnetic Field", in Conference on Lasers and Electro-Optics 2013 (2013), QM2D.2

T. K. Baldwin, S. O'Leary, and H. Wang, "Electromagnetically Induced Transparency of Spin Ensembles in a Two-Dimensional Electron Gas", in Conference on Lasers and Electro-Optics 2012 (2012), QM3G.5

T. M. Sweeney, T. Baldwin, and H. Wang, "Probing Heavy-Hole and Light-Hole Excitonic Beats in a GaAs Quantum well with Phase-Locked Raman Pulse Pairs", in Conference on Lasers and Electro-Optics 2010 (2010), QFI4

A. Imtiaz, T. Baldwin, H. T. Nembach, T. M. Wallis, and P. Kabos, "Near-field microwave microscope measurements to characterize bulk material properties", Applied Physics Letters **90**, 243105 (2007)

ACKNOWLEDGEMENTS

This dissertation would not exist were it not for the many wonderful people who helped me to complete it – whether by contributing directly to the scientific work, or by encouraging me when I needed motivation, or by shaping me into the scientist I am today.

My adviser, Hailin Wang, has supported me in all three of these ways. His relentless energy and keen insight have been instrumental in my growth as a scientist and the success of this project. The years I've spent working in his lab have been my greatest opportunity. I am grateful to have been well prepared for this undertaking by my schoolteachers, my college professors, my summer research mentors, and other people who guided my development.

I learned much of what I know from my labmates. Carey Phelps, Tim Sweeney, and Nima Dinyari mentored me when I was getting started in the lab. Mark Kuzyk, Thein Oo, Andrew Golter, Victor Fiore, Russell Barbour, and Chunhua Dong helped generously whenever I was stuck on a problem. Mayra Amezcua worked with me in my last year of experiments and read an advance copy of this dissertation. I am thankful for these and the many other students and postdocs who helped me along the way.

I wish to thank the people of the National High Magnetic Field Laboratory (NHMFL): Stephen A. McGill, Dima Semenov, and others helped me generously during my frenzied time conducting experiments in Tallahassee. John Prineas and Ronald T. Cox provided the semiconductor samples used, for which I am grateful. I thank the faculty of the UO Physics department for their input, especially Dan Steck, Georgy Nazin, and Dietrich Belitz, who comprise my faculty advisory committee.

These experiments would not have been possible without the work and the wisdom of the UO Technical Science Administration. Jeffrey Garman built many parts for these experiments, including the Faraday sample holder for use at the NHMFL. Kris Johnson lent his sage-like cryostat expertise. I drew upon the machining knowledge of John Boosinger and the electronics expertise of Cliff Dax countless times as well.

I thank the administrative staff of the Oregon Center for Optics and the Department of Physics. I owe special thanks to those who had the most headaches on my behalf: Jen Weber (who arranged my travel), Jani Scallion (who handled equipment purchasing), and Jodi Myers (who never let

me miss a deadline). I knew I could come to Brandy Todd or Bonnie Grimm with absolutely anything and they would help me find my way.

I thank the agencies who supported me financially: The UO Department of Physics, the National Science Foundation Division of Materials Research (NSF DMR), the NSF GK-12 program, and the UO Science Literacy program. The coordinators for these latter two programs helped develop me as a teacher: Anae Rosenberg, Christine Butler, Dean Livelybrooks, and Elly Vandergrift.

I am thankful for the people I've come to know throughout my time in Eugene, inside and outside the university, for their friendship and support. There are too many to name, but I must thank Mike Taormina, Paul Martin, Liza Brost, and Rick Montgomery, who were my closest confidants in my most challenging times.

During the writing of this dissertation, Cheri Young held me to a strict regimen of sanity-preserving picnics, hikes, and camping trips. She also signed me up for an elite ultimate frisbee league despite my never having played a game in my life. I'm grateful for her patience, support, and confidence in my ability to figure things out on the fly.

Finally, I thank my family for supporting me from the very beginning. My mother, Kathleen Baldwin, always helped me keep my life in perspective. My father, George T. Baldwin, advised me on every science project up to and including this one. My sisters, Anne Baldwin and Emily Baldwin, were unwavering in their support and encouragement, as were my aunts, uncles, cousins, and grandparents. This dissertation is dedicated to the memory of my grandfather, George C. Baldwin, who would have read the entire thing. Winnifred Baldwin wouldn't have wanted a part in any dedication, but I still think about her example every day.

For George C. Baldwin, the first physicist I ever met.

TABLE OF CONTENTS

Chapter Page

LIST OF FIGURES

Figure Page

# LIST OF TABLES

Table Page

# CHAPTER I

# INTRODUCTION

Semiconductors form the basis for applications in a broad range of technology, including sensing, lighting, energy generation, communication, and computation. Advances in the scientific understanding of semiconductors have in large part brought about the information age, and in the coming decades promise to bring about much more. Spintronics, quantum information processing, and highly efficient solar energy generation are among the future innovations driving continuing research in semiconductors.

Semiconductors also form a compelling platform for the study of physics. Questions involving many-body interactions between particles are frequently far too complex to be treated with existing theoretical or computational tools. This motivates experimental study, and quasiparticle excitations in semiconductors form a suitable model system for examining these intricate interactions.

In solid state physics, much can be understood by introducing the concept of quasiparticles: elementary excitations of the crystal ground state which behave like particles in a vacuum. Conduction-band electrons and valence-band holes are two examples which act as charge carriers in semiconductors. Coulomb attraction between these quasiparticles leads to formation of a a bound state called an *exciton*. Like the hydrogen atom does for electrons and protons, this two-body system forms the building block for interaction physics in semiconductors.

An advantage of using semiconductor charge carriers to study many-body interactions, as opposed to simply using real particles in free-space, is that the latter case would demand access to prohibitively high energy scales. Chemla and Shah [9] illustrate this with a stark comparison:

> For example, the exciton Rydberg in the model semiconductor gallium arsenide (GaAs) is only $4.2$ meV, about 3,000 times smaller than the hydrogen Rydberg ($13.6$ eV). Consequently, in GaAs the exciton ionization field, about $1\ \mathrm{V}\,\mu\mathrm{m}^{-1}$, can be easily achieved. Similarly, the magnetic field for which the cyclotron radius is equal to the Bohr radius (about $3.5$ T in GaAs) is easily delivered by commercial magnets, whereas for hydrogen it is about $10^4$ T, and is only found at the surface of neutron stars.

In short, semiconductor quasiparticle interactions make it possible to study the limits of interaction physics in tabletop experiments. In addition to expanding our understanding of complex

systems in general, such studies contribute to our knowledge of semiconductor systems in particular, which has relevance to a multitude of current and future technologies.

### 1.1. Trions

This dissertation concerns itself with the next building block beyond the exciton: the charged exciton, or *trion*. This complex is formed by the binding of an additional conduction-band electron or valence-band hole to the exciton, forming a three-body bound state. This structure lends itself to unique optical properties which will be examined in the chapters to follow.

Structurally, the trion is a manifestation of the three-fermion problem, which famously defies a closed-form solution. In contrast to the analogous atomic problems, the three-body nature of the problem is more fully evident in trions due to their having a mass ratio that is much closer to $1$. This is summarized by Israel Bar-Joseph [10]:

> The hydrogen ions are characterized by a very small mass ratio $m_e/m_p \approx 5 \times 10^{-4}$, and as a result, $H_2^+$ and $H^-$ are very different objects. $H_2^+$ is a strongly bound object, in which the electron orbits around the two protons. [...] In $H^-$ the two electrons orbit around the proton, and the repulsion between them is only marginally overwhelmed by the attraction to the nucleus. The resulting binding energy is 3.6 times smaller. Trions, on the other hand, are characterized by a large mass ratio, $m_e/m_h \approx 0.15$ in GaAs. Hence, one cannot neglect the motion of any of the particles and the three body nature of the structure is fully expressed.

Although the existence of trions was postulated by Lampert in 1958 [11], they were not observed in optical spectra until 1993, in CdTe [12]. This is in part because the binding energy of the third carrier is vanishingly small in a bulk crystal, and is not observable without the aid of dimensional confinement [13]. The eventual observation of trions in semiconductors relied on the development of growth techniques for high-quality quantum well heterostructures.

An excellent review on the optical signature of the trion is given in Ref. [10]. It appears as a resonance on the low-energy shoulder of the exciton peak when resident carriers are present in the system, offset by an amount equal to the binding energy of the additional electron or hole. When the resident carrier density is low, this peak is frequently small in absorption, since direct creation of

the three-body state is unlikely. In photoluminescence it is much more obvious, since photoexcited exciton states can subsequently bind to a free carrier, forming a trion before they decay.

### 1.1.1. Optical access to spin coherence

In the case where they are excited directly, trions can be thought of as an optical excited state of resident carriers, in the same way that excitons form an optical excited state for the crystal vacuum state. This opens avenues for optical manipulation of electron spins, a system that holds promise as the basis for future semiconductor devices [14]. In contrast to neutral exciton-based approaches, processes involving the trion resonance give direct control of a long-lived resident carrier spin.

Trion transitions form the basis for recent realizations of ultrafast control [15, 16] and electromagnetically induced transparency (EIT) [17] in quantum wells, utilizing electron spins. Coherent population trapping (an EIT-related process) of a single quantum dot emitter has been demonstrated via the trion transition [18]. Spin coherence times of electrons and holes is up to $10$ ns and $500$ ps, respectively, as determined by Kerr rotation techniques by way of the trion transition [19]. Chapter III of this work presents further examinations of the trion's relevance for EIT purposes.

### 1.1.2. Trions in high magnetic fields

Investigations of trions frequently leverage magnetic fields, since this can help reveal more about mixing processes within the valence band [20] and about the orbital structure of the trion itself [21].

In high magnetic fields, a spin-triplet form of the trion becomes bound, having an antisymmetric spatial wavefunction. This secondary trion state was observed in GaAs starting in 1995 [22, 23] and a detailed theoretical description given in 1997 [24]. Theoretical calculations of the triplet trion binding energy are complex; involving three interacting bodies in which the magnetic field and confining well width both play an important role. Obtaining accurate answers from theoretical models requires judicious selections with regard to the number of subbands to include, their non-parabolicity, and the effects of valence band mixing [25–28].

While theoretical models agreed that the triplet would cross the singlet to become the ground state of the system at particularly high magnetic fields, the precise point of crossing (whether at $20$ T, $30$ T, or even higher) was not clear. Experiments failed to confirm this crossing, or did so

inconclusively [29]. It was eventually found that multiple orbital states of the triplet exist, one of which becomes the ground state and one of which is optically bright [30]. Furthermore, the spectral lines do not actually cross, due to differences in energies due to Zeeman splitting, leading to a "hidden transition". The subject of trion triplets has continued to attract attention from theorists [31–35] and experimentalists [36–38].

### 1.1.3. Mediating bilayer interaction

Many recent efforts surrounding excitons have surrounded bilayer systems, in which electrons and holes reside in spatially separated wells. Excitons in these systems, called indirect excitons, have greatly extended lifetimes and can be more effectively cooled [39, 40]. Research in this area is motivated by the possibility of exciton Bose-Einstein condensation, although careful consideration is necessary to distinguish a condensate from simple biexciton formation in experiments [41].

Indirect exciton formation requires a relatively thin barrier between the two wells. In one recent experiment, the host structure featured a 4 nm barrier positioned between two 8 nm wells [42]. When the barrier is larger, the cross-barrier exciton interaction is weaker, but it can still have dramatic effects on the rate of carrier tunneling between layers [43]. In quantum Hall regime bilayers, in which two 18 nm quantum wells are separated by a 10 nm barrier, a giant increase in the tunneling rate occurs when every electron is positioned opposite a hole across the barrier [44, 45]. In these electron bilayer systems, "holes" refer to unoccupied Landau states in the conduction band, not valence-band holes.

Formation of indirect trions in bilayers has not been observed. However, the cross-barrier interaction of an exciton with an isolated carrier, the same interaction that leads to trion formation, has been shown to have a profound influence on carrier tunneling. Exciton-correlated tunneling, a transport process in mixed-type quantum wells, occurs when the tunneling of holes through a barrier is enchanced by a population of excitons [46]. We have shown that this originates in a local interaction between excitons and holes, the same interaction which gives rise to trions [3]. The novelty of this manifestation of the exciton-hole interaction is that it occurs indirectly through a barrier. As a practical matter, it may open a pathway for optical control of an electron transport process.

## 1.2. Dissertation Overview

This dissertation will present three distinct optical processes mediated by trions in semiconductor quantum wells. A review of the physics relevant to this topic is presented next, in Chapter II. Following this, Chapter III describes how the trion enables optical access to the robust electron spin coherence, evidenced by an experiment demonstrating electromagnetically induced transparency. In Chapter IV the structure of the trion is examined in high magnetic fields, including direct measurement of the density of states for its triplet state using optical absorption. Chapter V reports a detailed study of a novel tunneling phenomenon in a bilayer system, mediated by a three-body interaction that is suggestive of scattering through a trion-like state spanning two wells. The unique and subtle interactions underlying this process open a new avenue for optical control of semiconductor transport processes. Taken together, these three studies present a comprehensive picture of the importance of trions in semiconductor optics, summarized in Chapter VI.

Two appendices supplement the main thread of work. Appendix A contains a theoretical review that highlights the relevance of optical absorption spectroscopy in determining the state of the underlying quantum system, relevant for several chapters in the main text. Appendix B outlines a simple technique for reducing nonradiative decoherence by mixing states with a stable optical field. This is not specifically related to any experiment concerning trions, but is reflective of a contribution to Ref. [1], in which this technique is implemented in diamond nitrogen-vacancy centers.

Chapters II and V contain material previously published with co-authors Stephen A. McGill and Hailin Wang [3]. Portions of Chapter III were previously published in proceedings of the Quantum Electronics and Laser Science Conference (CLEO: QELS) with co-authors Shannon O'Leary and Hailin Wang [6].

# CHAPTER II

# THEORETICAL BACKGROUND

The research presented in this dissertation concerns the study of trions, a bound state of three charge carriers in semiconductors. This chapter presents a review of the underlying physics related to excitons and trions, and the semiconductor heterostructures which facilitate their study using optical techniques. Portions of this chapter were previously published with co-authors Stephen A. McGill and Hailin Wang [3].

## 2.1. Physics of Semiconductors

Semiconductors are composed of a crystalline lattice of covalently bonded atoms. Electron states within the lattice are characterized by semicontinuous bands of allowed energies, formed from hybridization of atomic orbitals to form molecular orbitals that extend over the entire crystal [47, chapters 1 and 7]. Conceptually, the broadening of discrete atomic energy levels into bands is an extension of the bonding-antibonding splitting in diatomic molecules: Overlap between outer-lying atomic orbitals leads to an exchange interaction, causing the stationary electron wavefunctions to take on the symmetry of the crystal, rather than being centered at individual lattice sites. The magnitude of the associated energetic splitting is set by the degree of wavefunction overlap, and its multiplicity by the number of sites involved. When this is of order $10^{23}$, it is considered a quasicontinuous band, with the lower-energy half having bonding character and higher-energy part having antibonding character.

Semiconducting properties emerge when the level broadening exceeds the level spacing of the constituent atoms. Depending on symmetry, certain bonding states in the $p$-orbital derived band may cross the antibonding states from the adjacent $s$-orbital derived band below it, while others experience anticrossing behavior [48]. This leads to further mixing of the electron states and opens ranges in energy where no electron states exist, or *band gaps*. For crystals in column IV of the periodic table, or compound materials composed of III-V and II-VI elements, these gaps can perfectly divide the electron occupation in the valence shell, so that the highest occupied electron state sits right below a large gap.

Within each band, states are labeled by the continuous variable $\vec{k}$, the crystal momentum. The corresponding wavefunctions permeate the entire crystal and may be thought of a set of giant molecular orbitals. Treatment of these states is in many ways analogous to the treatment of free electrons having real momentum $\vec{p}$, but this relationship is purely formal: In fact, $\vec{k}$ labels a set of phase modulations, $e^{i\vec{k}\cdot\vec{r}}$, applied to a wavefunction that is invariant under translation by any of the lattice vectors. These phase modulations, called the *Bloch wavefunctions*, are sufficient to construct the full set of crystalline electron states, since the full wavefunctions all share a modulation having periodicity of the crystal.

The total wavefunctions have two periodicities, then: the periodicity of the crystal (which is fixed) and an additional periodicity having wavenumber $\vec{k}$ (which is the Bloch part). Note that $\vec{k}$ becomes a redundant label above some bound where it aliases with the crystal lattice. The geometry-dependent range of distinct $\vec{k}$ values is called the Brillouin Zone. The center ($\vec{k} = 0$) point of the zone is labeled $\Gamma$, with points of maximal $\vec{k}$ along important crystal directions labeled by $X$, $L$, etc.

Frequently, dispersion around $\Gamma$ (the $\left|\vec{k}\right| = 0$ state) is to first approximation parabolic,

$$H = \frac{\hbar^2 \vec{k}^2}{2m_{\text{eff}}}, \tag{2.1}$$

with the effective mass parameter $m_{\text{eff}}$ quantifying its curvature. Like $\vec{k}$, this is a purely formal designation, and need not equal the electron rest mass. Indeed, it has more to do with the breadth of the band: Broad bands, spanning a large range of energies, contain a steeper dispersion curve, corresponding to a lighter mass. A narrow band has a smaller range of energies labeled by the same range of $\vec{k}$, so it has a shallower (heavier) dispersion curve.

Two important caveats exist: First, although it is for the semiconductors in this dissertation, the energetic minimum need not occur at $\vec{k} = 0$: It can also occur at the edge of the Brillouin zone. In real space, this is equivalent to saying that the lowest-energy molecular orbital may have its antinodes at various places within the unit cell: at one of the (possibly multiple) atomic sites, or at certain interstitial sites. Second, the effective mass can be anisotropic, a consideration we return to in section 2.2.

The Bloch wavefunctions can be used to construct spatially localized electron wavepackets in the same manner as states for free particles: by constructing a superposition from states having some

range of crystal momenta $\Delta k$, limited by the wave uncertainty relation

$$\Delta x \Delta k \approx 1, \tag{2.2}$$

where $\Delta x$ is the range over which the wavepacket is localized. The set of spatially-localized wavepackets constructed in this way also forms a (non-stationary) basis for the electron states.

### 2.1.1. Conduction properties

We could represent a moving charge by such a wavepacket centered at nonzero $k$. To represent a net movement of charge, this must involve both full and empty $k$ states. But if every state in a band is full (or if every one is empty), there is no way to represent charge transport without incorporating states from another band that is empty (or full). When separated by a band gap, this is energetically expensive. For this reason, intrinsic semiconductors are not conducting.

In contrast, if a few states are occupied in the lowest empty band (conduction band), then they can readily conduct charge by displacing empty states around them. Alternatively, unoccupied states in the highest occupied band (valence band) can conduct charge by being displaced by occupied ones. From this point of view, we can consider the vast number of actual electrons participating in the bonding as a *crystal vacuum* and think only about *conduction-band electrons* carrying net negative charge, and *valence-band holes* carrying net positive charge.

The introduction of extra electrons or holes to the lattice is referred to as "doping." Doping can originate from the inclusion of impurities or via thermal or optical excitations. The ability of small adjustments in the carrier balance to dramatically alter the conduction properties is the key to semiconductors' usefulness as transistors.

Henceforth in this dissertation, the term "electron" will refer to the crystal excitation, not the fundamental particle, unless specifically designated by the term "free electron".

### 2.1.2. Optical properties

We have described a renormalization of the complicated business of crystal lattice excitations into two quasiparticles, electrons and holes, which carry charge and have (effective) mass. In addition, electrons and holes carry angular momentum, derived from both the intrinsic spin of the electron and from the orbital angular momentum of the underlying atomic orbitals. This results in certain

$s$-like bands where electrons carry spin $\pm\frac{1}{2}$, and $p$-like bands where holes carry both $\pm\frac{1}{2}$ and $\pm\frac{3}{2}$. The materials used in this dissertation, GaAs and CdTe, have an $s$-like conduction band and a $p$-like valence band. In the valence band, the holes carrying $\pm\frac{3}{2}$ spin are heavy, and the holes carrying $\pm\frac{1}{2}$ spin are light. Therefore, one commonly refers separately to the heavy-hole (HH) or light-hole (LH) valence bands.

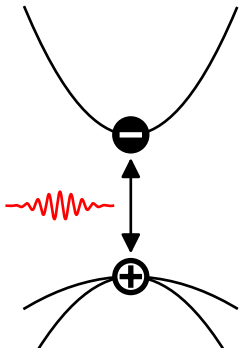

FIGURE 2.1. Dispersion diagram for a direct-gap semiconductor with HH and LH valence bands. A photon can promote a valence-band electron to the conduction band, leaving a valence-band hole. Note that the energy scale shown is for electrons, so that holes in the valence band have an inverted energy scale.

Electrons and holes may be created in pairs when a valence-band electron absorbs a photon with an energy exceeding that of the band gap. Spatial overlap of the starting VB state and ending CB state is required. In practice this requires that the generated electron and hole have the same $\vec{k}$, that is, optical transitions couple states vertically on the dispersion diagram (Fig. 2.1). Angular momentum conservation determines the optical selection rules between bands, since circularly-polarized photons carry spin $\pm 1$.

Optical properties are most pronounced in direct-gap semiconductors, such as GaAs, in which the bottom of the conduction band has the same $k$ as the top of the valence band. Here, the highest density of electron and hole states can be linked by an optical dipole transition. While this is the case in direct-gap materials such as GaAs and CdTe, it is not so for indirect-gap materials such as Si. In these materials, transitions between the band edges require a phonon as well as a photon.

## 2.2. Effective-Mass Anisotropy

As mentioned in section 2.1, the effective mass can be anisotropic. For example, for a simple cubic lattice of atoms having $p_x$ orbitals, nearest neighbors along $x$ will have lobes of opposite sign adjacent to one another, causing their wavefunction-overlap integral to be relatively small. Orbitals of nearest neighbors along $y$ will have adjacent lobes with the same sign, leading to larger overlap (and larger energetic splitting). As a result, the band formed from these orbitals will be broader for electrons with crystal momentum along $y$, necessitating a larger curvature of $k_y$ and hence a lighter effective mass [49, chapter 8]. The same band would appear heavy in the $x$ direction, since the wavefunction overlaps are smaller: so a phase modulation along $k_x$ wouldn't have as much of an effect.

Of course, if those same atoms also have $p_y$ orbitals, they will form a degenerate band that is light along $x$ and heavy along $y$. In $k$-space, equal-energy manifolds of each of these bands can be pictured as three oblate, concentric surfaces with their short axes aligned along each of the coordinate axes. Spin-orbit couplings cause lift degeneracies at the crossing points, leading to an outer surface corresponding to a "heavy" band and an inner surface that is "light".

In semiconductors with the zincblende structure, the conduction band is $s$-like while the valence band has this more complex $p$-type structure. Anisotropy in the valence band is determined from $k \cdot p$ perturbation theory, which results in the *Luttinger-Kohn Hamiltonian* given by

$$H = \begin{bmatrix} P+Q & 0 & -S & R & \frac{\sqrt{2}S}{2} & \sqrt{2}R \\ 0 & P+Q & -R^* & -S^* & -\sqrt{2}R^* & \frac{\sqrt{2}S^*}{2} \\ -S^* & -R & P-Q & 0 & \sqrt{2}Q & \frac{\sqrt{6}S}{2} \\ R^* & -S & 0 & P-Q & -\frac{\sqrt{6}S^*}{2} & \sqrt{2}Q \\ \frac{\sqrt{2}S^*}{2} & -\sqrt{2}R & \sqrt{2}Q & -\frac{\sqrt{6}S}{2} & \Delta_{SO}+P & 0 \\ \sqrt{2}R^* & \frac{\sqrt{2}S}{2} & \frac{\sqrt{6}S^*}{2} & \sqrt{2}Q & 0 & \Delta_{SO}+P \end{bmatrix} \tag{2.3}$$

where

$$P = \left(\frac{\hbar^2}{2m_0}\right)\gamma_1\left(k_x^2 + k_y^2 + k_z^2\right) \tag{2.4}$$

$$Q = \left(\frac{\hbar^2}{2m_0}\right)\gamma_2\left(k_x^2 + k_y^2 - 2k_z^2\right) \tag{2.5}$$

$$R = \left(\frac{\hbar^2}{2m_0}\right)\sqrt{3}\left[-\gamma_2\left(k_x^2 - k_y^2\right) + 2i\gamma_3 k_x k_y\right] \tag{2.6}$$

$$S = \left(\frac{\hbar^2}{2m_0}\right)2\sqrt{3}\gamma_3 k_z k_- \tag{2.7}$$

and where $k_- = k_x - ik_y$, which $m_0$ the electron rest mass in vacuum. This gives the energy of a hole with arbitrary $\vec{k}$ in each of the three bands. Each set of two rows (columns) represents a pair of two spin states in each of the bands. The ***Luttinger parameters*** $\gamma_1$, $\gamma_2$, and $\gamma_3$ are dimensionless material parameters which give the shape of the bands. One of the three orbitals has been shifted by spin-orbit coupling, parametrized by $\Delta_{SO}$. Numerical values for these parameters are given in Table 2.1.

TABLE 2.1. Lattice and material parameters for GaAs, reproduced from Ref. [50].

| Quantity | GaAs value |
|---|---|
| Band gap , $E_g$ (eV) | 1.426 |
| Dielectric constant, $\epsilon/\epsilon_0$ | 13.2 |
| Electron effective mass, $m_e/m_0$ | .067 |
| Heavy-hole effective mass,† $m_{hh}/m_0$ | .62 |
| $\gamma_1$ | 6.98 |
| $\gamma_2$ | 2.06 |
| $\gamma_3$ | 2.93 |

† Spherically averaged.

It's instructive to examine this Hamiltonian to further understand mass anisotropy. First of all, at $\vec{k} = 0$, the matrix is diagonal, with the first two bands (four states) energetically degenerate (having $E = 0$) and the third "split-off" band having $E = \Delta_{SO}$. Since every other term in the Hamiltonian besides $\Delta_{SO}$ goes as $\left|\vec{k}\right|^2$, the first-order corrections to these energies for nonzero $\vec{k}$

can be read directly off the diagonal. We are especially interested in the two $E = 0$ bands:

$$P \pm Q = \frac{\hbar^2}{2m_0} \left[ (\gamma_1 \pm \gamma_2) \left( k_x^2 + k_y^2 \right) + (\gamma_1 \mp 2\gamma_2) k_z^2 \right]. \tag{2.8}$$

Along $k_z$ ($k_x = k_y = 0$), the $P + Q$ band varies parabolically with a "heavy" effective mass

$$m_{\mathrm{hh}}^{(z)} = \frac{m_0}{\gamma_1 - 2\gamma_2} \tag{2.9}$$

relative to the $P - Q$ band, which is "light":

$$m_{\mathrm{lh}}^{(z)} = \frac{m_0}{\gamma_1 + 2\gamma_2}. \tag{2.10}$$

Since all off-diagonal terms are zero except for one coupling between the $P - Q$ band and the split-off band, these are designated the ***heavy-hole*** and ***light-hole*** valence bands. However, this is only with respect to $z$: In the $x - y$ plane, with $k_z = 0$, the heavy holes are light:

$$m_{\mathrm{hh}}^{(x,y)} = \frac{m_0}{\gamma_1 + \gamma_2} \tag{2.11}$$

and the light holes are heavy:

$$m_{\mathrm{lh}}^{(x,y)} = \frac{m_0}{\gamma_1 - \gamma_2}. \tag{2.12}$$

Numerical values for GaAs are given in Table 2.2. Of course, there are many more off-diagonal terms when $k_x$ or $k_y$ is nonzero, and a full diagonalization (which changes the spin basis) recovers the curvatures that were evident along $z$. Like spin, effective mass is only definitely "heavy" or "light" along a certain direction, chosen here to be the spin quantization direction $z$. This ***mass reversal*** property will play an important role when considering systems that break spherical symmetry.

TABLE 2.2. Transverse and longitudinal effective mass parameters for GaAs, computed from the Luttinger parameters in Table 2.1, illustrate the magnitude of mass anisotropy.

| GaAs | $m^{(z)}/m_0$ | $m^{(x,y)}/m_0$ |
|---|---|---|
| HH | 0.35 | 0.11 |
| LH | 0.09 | 0.20 |

## 2.3. Excitons and Trions

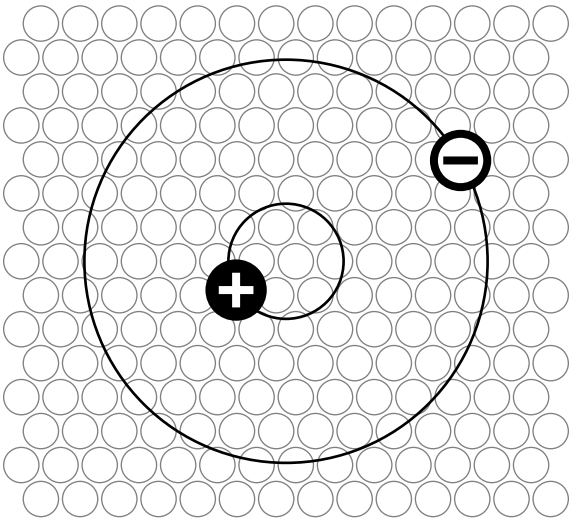

FIGURE 2.2. Conceptual view of an exciton. An electron and hole, orbiting around their mutual center of mass, form a Wannier exciton. The spatial extent of their wavefunction spans many lattice sites.

Since they carry opposite charge, electrons and holes feel a mutually attractive Coulomb force which can result in a bound state, called a Wannier exciton (Fig. 2.2). Another exciton formulation, the Frenkel exciton, is relevant when the length scales are too small to justify the use of an effective mass, but that is not relevant for this work.

In the effective-mass approximation, a Hamiltonian for an electron-hole pair is

$$H = \frac{p_e^2}{2m_e} + \frac{p_h^2}{2m_h} - \frac{e^2}{4\pi\epsilon}\frac{1}{|r_e - r_h|} \tag{2.13}$$

Where the last term gives their mutual Coulomb potential, with $e$ the fundamental charge and $\epsilon$ the permittivity of the medium. By defining a ***reduced mass*** $\mu = m_e m_h/(m_e + m_h)$ and changing to center-of-mass coordinates $R = \mu\left(r_e/m_h - r_h/m_e\right)$ and $r = r_e - r_h$, the Hamiltonian becomes

$$H = \frac{P^2}{2\left(m_e + m_h\right)} + \frac{p^2}{2\mu} - \frac{e^2}{4\pi\epsilon}\frac{1}{|r|} \tag{2.14}$$

where $P$ and $p$ are the conjugate momenta to $R$ and $r$, respectively. The first term gives free motion of the two quasiparticles' center of mass, and the second two terms are the same as the Hamiltonian

for hydrogen with the replacement $m_e \to \mu$. In three dimensions, this leads to the same spectrum of bound states

$$E_n^{\mathrm{3D}} = -\frac{\mu}{2\hbar^2}\left(\frac{e^2}{4\pi\epsilon}\right)^2 \frac{1}{n^2} \tag{2.15}$$

where $n = 1, 2, 3...$ is the principal quantum number. This energy is relative to that of the unbound electron-hole pair, which is the band gap energy $E_g$ required to create the pair in the first place. The most strongly bound $1s$ exciton, with $n = 1$, has the spherically symmetric wavefunction

$$\psi(r, \theta, \phi) = \frac{1}{\sqrt{\pi a^3}} e^{-r/a} \tag{2.16}$$

having Bohr radius

$$a = \left(\frac{4\pi\epsilon}{e^2}\right)\frac{\hbar^2}{\mu}. \tag{2.17}$$

As in the case of hydrogen, excited states are counted by two more quantum numbers, $l$ (which ranges from $0$ to $n-1$) and $m$ (which ranges from $-l$ to $l$.) In this work we will primarily be concerned with the $1s$ exciton only.

In GaAs, where $\epsilon = 13.2\epsilon_0$, and using a spherically averaged value of the heavy-hole effective mass, this yields a binding energy $E_1$ of $-4.7$ meV and a Bohr radius of $115$ Å [50]. The fact that the exciton is so large relative to the lattice spacing confirms that we are in the Wannier regime, and justifies the use of the effective-mass approximation in obtaining this result.

While structurally similar to hydrogen, the exciton is orders of magnitude more weakly bound and larger (relative to the Rydberg and Bohr radius for hydrogen, which are $-13.6$ eV and $0.53$ Å, respectively). This is a due to both the large permittivity of GaAs and to a larger mass ratio, $m_e/m_h$.

### 2.3.1. Optical excitation of excitons

Being antiparticles, the electron and hole have a finite lifetime, typically on the order of picoseconds, before they recombine, possibly emitting a photon. In this respect, the exciton is more directly analogous to positronium than it is hydrogen, with the crystal lattice serving as a vacuum state that can be ionized at the energy scale of an infrared laser rather than that of gamma rays.

By considering in detail the structure of the crystal vacuum, one can arrive at an expression for the optical absorption of an exciton. The electron-hole pair susceptibility, when accounting for the

exciton interaction, is given by Haug and Koch [51] as

$$\chi(\omega) = -2\left|d_{cv}\right|^2 \sum_n \left|\psi_n\left(r=0\right)\right|^2 \left[\frac{1}{\hbar(\omega+i\delta)-E_g-E_n} - \frac{1}{\hbar(\omega+i\delta)+E_g+E_n}\right]. \tag{2.18}$$

The absorption coefficient follows as the imaginary part. The term in brackets gives the Lorentzian shape of the line having width $\delta$, with prefactors giving amplitudes (oscillator strengths). The $d_{cv}$ term is the dipole matrix element for transitions between the conduction ($c$) and valence ($v$) bands, independent of any exciton effects. The term involving $\psi_n(r)$, the exciton wavefunction of principal quantum number $n$, evaluated at $r = 0$, is what limits optically accessible exciton states to the ones with $s$-like wavefunctions. In three-dimensional hydrogen,

$$\left|\psi_n(r=0)\right|^2 = \frac{1}{\pi a_0^3 n^3} \tag{2.19}$$

which scales with the inverse of the cube of the Bohr radius. Hence, the strength of optical absorption can be considered a measure of the exciton's physical size.

Another respect in which the exciton is more akin to positronium than hydrogen is its having a mass ratio much closer to 1: $m_e^{\text{eff}}/m_h^{\text{eff}} \approx 0.11$ in GaAs, whereas $m_e/m_p \approx 5 \times 10^{-4}$ [10]. In positronium, the mass ratio is exactly 1.

This is exceptionally important when considering the charged exciton, or trion, since it stymies approximation of any one participant particle as a fixed central potential. For this reason, the trion an even purer manifestation of the three-body problem than the frequently-studied $H^-$ atom, since the motion of all three bodies is important.

### 2.3.2. Effects of dimensional confinement

When restricted to move in a two-dimensional plane, hydrogenic complexes are more strongly bound. This is demonstrated by a theoretical treatment of the 2D hydrogen atom [52], which has the modified spectrum

$$E_n^{\text{2D}} = -\frac{\mu}{2\hbar^2}\left(\frac{e^2}{4\pi\epsilon}\right)^2 \frac{1}{\left(n-\frac{1}{2}\right)^2} \tag{2.20}$$

which for the $n = 1$ ground state is four times greater, $E_1^{2D} = 4E_1^{3D}$. Likewise, excitons are much more strongly bound when the dimensionality of space is reduced. This is also true of trions [13, 31, 34], for reasons that are less straightforward to understand.

### 2.4. Quantum Well Heterostructures

Quantum wells implement dimensional confinement for carriers by sandwiching a thin (~10 nm) layer of semiconductor material between barriers composed of a similar material having a larger band gap. Smooth, lattice-matched interfaces are achieved in the case of $Al_xGa_{1-x}As$ by sharply varying the Al content during the growth process in molecular beam epitaxy. Depending on the band alignment between the two, this results in finite square well confinement for one or both species of carrier along the growth direction $z$. A Type-I quantum well confines both conduction band electrons and valence band holes. This is shown schematically in Fig. 2.3.

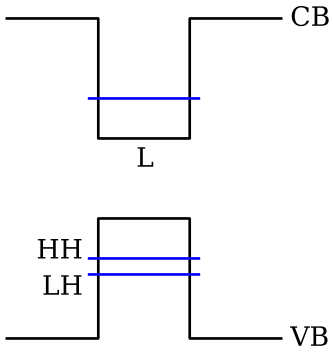


FIGURE 2.3. Band-edge profile of a Type-I quantum well in real space. For each band, only one subband is shown. Finite square well confinement results for electrons and holes. Recall that for the valence band, the energy axis for holes is inverted.

This leads to quantization of the $k_z$ component of the crystal momentum into the discrete particle-in-a-box spectrum. The $k_x$ and $k_y$ are not quantized, and retain their parabolic dispersion in those transverse dimensions. Hence, the quantization of $k_z$ serves to break the 3D continuum of Bloch states into discrete subbands of 2D continuums, each having an energetic offset from the band edge by an amount equal to the well confinement energy along $z$.

In $Al_xGa_{1-x}As$, the band gap varies from $1.4$ eV (at $x = 0$) to $3.0$ eV (for pure AlAs), with the mismatch distributed $2 : 1$ between the conduction and valence bands. Bound states can be found by solving the Schrödinger equation in the $z$ direction for the spatially-dependent potential

given by the band edge, taking care to account for effective-mass mismatches. Common numerical approaches include the shooting method (in the effective-mass approximation) and transfer matrix method utilizing the full Luttinger-Kohn Hamiltonian (which includes effects of non-parabolic valence bands) These are considered in detail in Ref. [50].

This quantization lifts the degeneracy between the heavy-hole and light-hole bands at the zone center (where $\vec{k} = 0$). For wells $10$ to $20$ nm wide, which is typical, confinement energies in the valence band are typically of order $5$ meV for the lowest heavy hole state, and $10$ meV for the lowest light hole state. The heavy hole, now the ground state for holes, now lies the at the top of the valence band. This is expected since $m_h^{(\mathrm{eff})}$ appears in the denominator of the kinetic energy expression (2.1), and $k_z$ is quantized to approximately the same value for both HH and LH bands.

### 2.4.1. Quantum well excitons

In the limit where only the lowest subband is populated, the carriers are effectively constrained to move in two dimensions, and we expect to observe the properties of the two-dimensional confinement described in 2.3.2.

Recall from 2.2 that the in-plane masses are reversed in GaAs. In a quantum well, the quantum-confined heavy holes will be lighter than the light holes with regard to their lateral motion in the well, and mass related to this in-plane motion is the relevant quantity for determining the wavefunctions of excitons.

Using the expression for the exciton binding energy (2.20) with the values for the in-plane masses of Table 2.2, we estimate the HH and LH 2D excitons to have Rydbergs of $-13$ and $-16$ meV, respectively. Combined with the $5$ and $10$ meV subband offsets computed previously, we expect to observe HH and LH exciton resonances separated by $2$ meV in GaAs QWs.

This is shown in the optical absorption spectra of Fig. 2.6, with the heavy hole exciton appearing lower in energy. Each transition is spin-degenerate, with cross-circularly polarized selection rules shown in Figs. 2.4 and 2.5. These are confirmed experimentally by applying a red-detuned pump pulse and measuring ac stark shifts in the absorption spectrum.

In addition to confinement, successful optical observation of the trion calls for a reservoir of excess electrons or holes. For this, the quantum well will need to be doped with a gas of excess carriers.

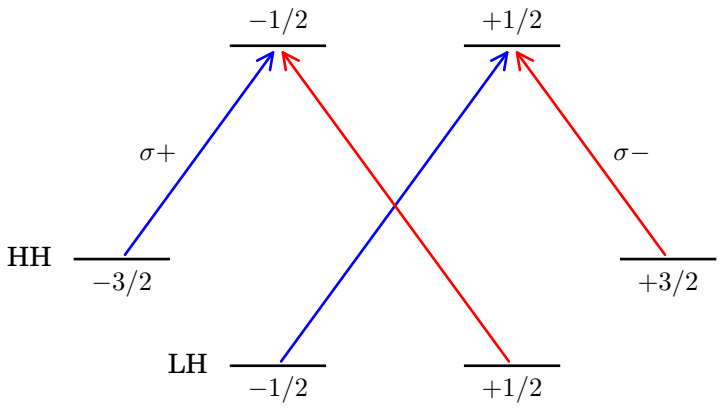


FIGURE 2.4. Optical selection rules for interband transitions. Circularly-polarized photons promote electrons to conduction-band states from the heavy- and light-hole bands.

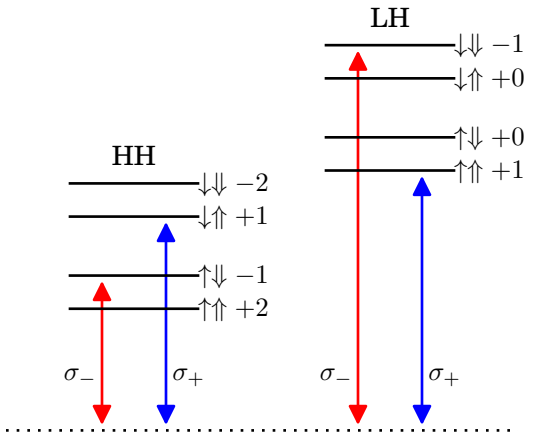


FIGURE 2.5. Optical selection rules for interband transitions, electron-hole picture. Same transitions as in Fig. 2.4, in the view where a fully populated valence band forms a vacuum state (dotted line) from which heavy- and light-hole excitons are generated. Note that hole spin is opposite that of the electron state from which it is generated.

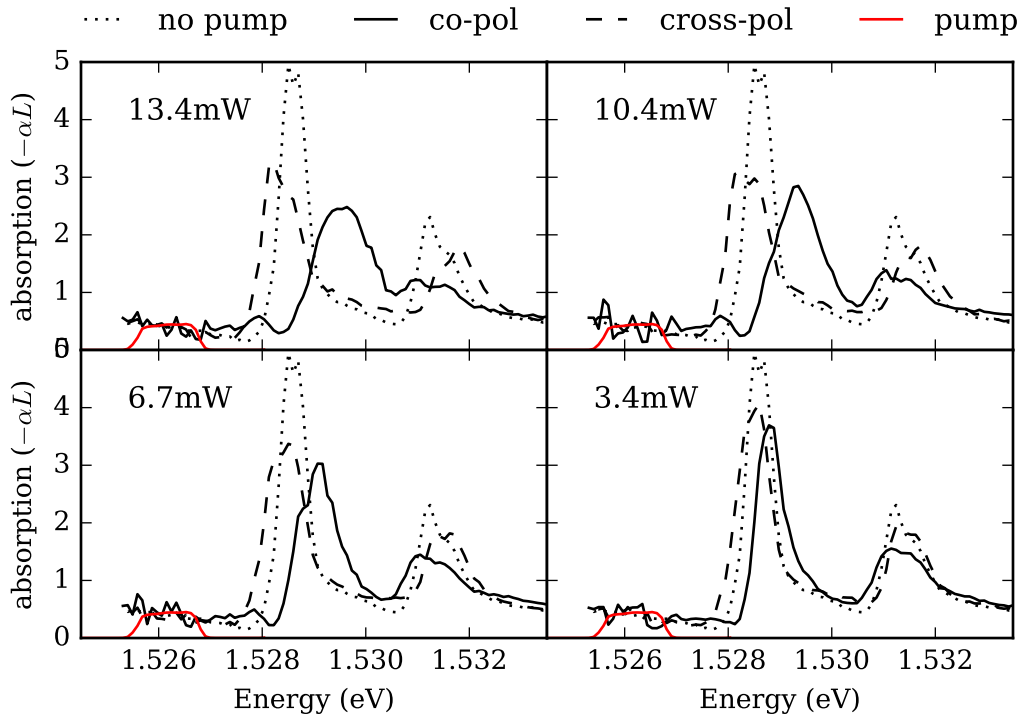


FIGURE 2.6. AC stark shifts of exciton absorption resonances. Linear absorption spectra (dotted lines) reveal both heavy- and light-hole exciton species. Spin degeneracy is lifted in the presence of a red-detuned, circularly polarized pumping beam (red profile), with the shifted line appearing in absorption of either cross-polarized (dashed line) or co-polarized (solid lines) light. The direction of shift confirms the optical selection rules laid out in Figure 2.4. Sample: 10 periods undoped GaAs multiple quantum well at 10.5 K. Four plots show four values of the pump power.

## 2.5. Two-dimensional Carrier Gases

When quantum wells contain a reservoir of excess electrons or holes, this is referred to as a two-dimensional electron (or hole) gas (2DEG/2DHG). While this arrangement makes possible the formation of trions, presence of such a charged gas also screens the interaction between an exciton's constituent electron and hole. Since the exciton is large (of order 100 Å), a 2DEG creates an interstitial mean field of negative charge that results in a reduced oscillator strength for their optical absorption profile.

Generation of such a carrier gas is achieved by doping the quantum well. One advantage of QWs is that they can be doped without introducing impurity scattering to carriers in the well. By implanting donor ions in the barrier material, donated electrons or holes are free to settle into the QW while the ionic scattering sites remain spatially separated in the well. This process is referred to as *modulation doping*.

The drawback of this technique is that it depends on crystal growth parameters, so injected carrier gases are difficult to adjust in the context of an experiment. For experiments in this dissertation where a dynamically adjustable 2DEG is desired, *optical doping* is employed, utilizing a novel multiple-well structure called the *mixed-type quantum well*.

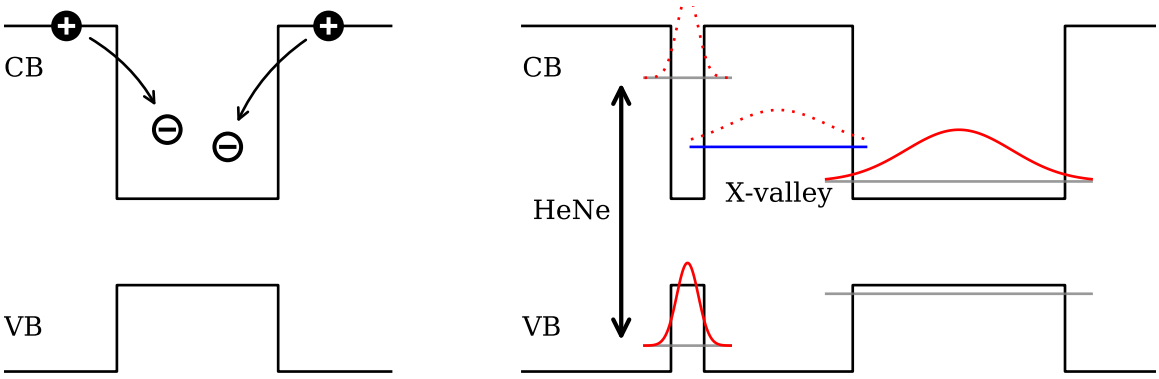


FIGURE 2.7. Two approaches to quantum-well doping. Left: Modulation doping, in which electrons from donor ions implanted in the barrier thermalize into the well. The dopants form a 2DEG that is free from scattering from the donor sites. Right: Optical doping using a mixed-type quantum well (MTQW). Photoexcited electrons in the narrow well thermalize and transfer via the AlAs $X$-valley into the wide well. The resulting 2DEG in the wide well persists until the holes tunnel through the barrier.

### 2.5.1. Mixed-type quantum wells

The mixed-type quantum well (MTQW) is a multiple-QW heterostructure designed to exhibit low power optical nonlinearities based on 2DEGs [53, 54]. In place of doping with impurities, MTQW are doped by an optical excitation in a secondary QW. This "optical doping" requires relatively little optical power, which makes it of interest for application in optical switching devices.

In a GaAs MTQW, a narrow GaAs well is separated by a thin AlAs barrier from a wide GaAs well (see the right side of Fig. 2.7). Since AlAs is an indirect-gap material having a conduction band minimum at the $X$ point of the Brillouin zone, the barrier acts like a well for conduction-band electrons having $\vec{k}$ near $X$, resulting in a bound state called the $X$-valley.

The narrow well (NW) is a type-II QW, in which quantum confinement raises the bottom of the conduction band to a higher energy than the X-valley in the AlAs barrier. After an optical excitation of electron-hole pairs in the NW having $\vec{k} = 0$, electrons can thermalize and transfer via the X-valley to the conduction band of the wide well (WW). The holes have no such intermediary state, so they remain trapped in the NW [53, 54].

Carrier densities ranging from $10^7/\text{cm}^2$ to $10^{10}/\text{cm}^2$ can be generated and controlled via the optical excitation. The excess electrons and holes separated by the thin barrier form an electron-hole bilayer, with the lifetime of the carriers determined by the tunneling of the holes from the narrow to the wide well [55, 56]. Within this lifetime, a 2DEG persists in the WW, the excitonic properties of which have been extensively investigated [46, 57–64].

The specific sample used in our studies in Chapters IV and V consists of three periods of narrow (2.5 nm) and wide (16 nm) GaAs wells separated by an 11.2 nm AlAs barrier. Two NWs have been placed symmetrically on both sides of the WWs in order to minimize space-charge fields due to buildup of spatially separated carriers. The valence-band structure of each well, computed by Phelps [46] from the 6-level Luttinger-Kohn Hamiltonian, is shown in Fig. 2.8. The overlap between NW and WW dispersion curves is important in determining the tunneling rate, since holes leaving the NW must tunnel into an available WW state. In our sample, this is the fifth HH subband. The crossing points between the first subband in the NW and fifth HH subband in the WW in the diagram are states at which a energy- and momentum-conserving tunneling event can occur.

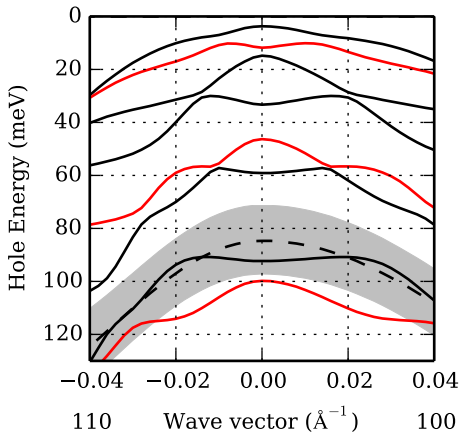


FIGURE 2.8. Calculated subband dispersion in MTQW sample, for narrow (dashed lines) and wide (solid lines) wells. Red lines indicate LH bands, others HH. Tunneling occurs where the ground NW state and the fifth excited WW HH state overlap. The gray band indicates the energetic difference made by monolayer fluctuations in the NW.

## 2.6. Magnetic Field Properties

An external magnetic field affects carriers in two important ways. The first is by lifting spin degeneracy via the Zeeman effect, which is modeled by including the Hamiltonian term

$$H_B = \frac{g\mu_B}{\hbar}\vec{S}\cdot\vec{B} \tag{2.21}$$

which contributes a linear $\pm g\mu_B B$ to the energy, with a slope set by the $g$-factor of the carrier.

The second influence is via the Lorentz interaction on moving electrons and holes. Classically, a moving charge feels a sideways force $\vec{F} = q\vec{v}\times\vec{B}$, causing it to move in a circular orbit in the plane perpendicular to $\vec{B}$. Quantum mechanically, the harmonic motion of these orbits is quantized into discrete, equally spaced levels called Landau levels.

This is incorporated into the quantum Hamiltonian by making the replacement

$$\vec{k} \to \frac{\hbar}{i}\vec{\nabla} + e\vec{A} \tag{2.22}$$

rather than the typical replacement $\vec{k} \to \frac{\hbar}{i}\vec{\nabla}$. Here, $\vec{A}$ is a vector potential which generates the field by $\vec{B} = \vec{\nabla}\times\vec{A}$. This affords a certain freedom in the choice of gauge: For a $\vec{B}$ aligned along the $z$ axis,

we typically proceed in either the Landau gauge

$$\vec{A} = Bx\hat{y} \tag{2.23}$$

or the symmetric gauge $\vec{A} = \frac{Bx}{2}\hat{y} - \frac{By}{2}\hat{x}$. Both yield the same energy spectrum, but with different forms for the resulting set of wavefunctions. A lucid treatment of several approaches is given in [65, ch22] and [66]. Here we sketch the derivation in the Landau gauge, using cartesian coordinates.

Ignoring spin for the moment, we start by making the replacement (2.22) using the explicit form (2.23), resulting in the Hamiltonian

$$H = -\frac{\hbar^2}{2m}\left[\frac{\partial^2}{\partial x^2} + \left(\frac{\partial}{\partial y} + i\frac{eB}{\hbar}x\right)^2 + \frac{\partial^2}{\partial z^2}\right]. \tag{2.24}$$

Recognizing that this form preserves translational invariance in the $y$ and $z$ directions, we proceed to solve the eigenvalue problem using the ansatz

$$\psi(x, y, z) = u(x)e^{ik_y y}e^{ik_z z} \tag{2.25}$$

where $u(x)$ is the (currently undetermined) function in the $x$ direction. This results in

$$-\frac{\hbar^2}{2m}\frac{d^2u(x)}{dx^2} + \frac{1}{2}m\omega_c^2\left(x - x_0\right)^2 u(x) = \left(E - \frac{\hbar^2 k_z^2}{2m}\right)u(x) =: E_\perp u(x) \tag{2.26}$$

where we have designated the cyclotron frequency $\omega_c = eB/m$. Apart from the motion in $z$, where the free-particle behavior is retained, we recognize the rest as the harmonic-oscillator Hamiltonian. In-plane motion is characterized by harmonic motion in $x$, centered at $x_0$, where

$$x_0 = -\frac{\hbar}{eB}k_y =: -l_0^2 k_y \tag{2.27}$$

and where we've defined the *magnetic length*

$$l_0 = \sqrt{\hbar/eB}. \tag{2.28}$$

This is the only way in which the quantum number $k_y$ enters the Hamiltonian: by determining the spatial coordinate $x_0$ at which the oscillator is centered in the $x$ direction. Since this does not affect the oscillator's energy, $k_y$ now only labels degeneracy. In contrast, the continuous quantum number $k_x$ is replaced by the principal quantum number $n$ in the oscillator spectrum

$$E_\perp = \left(n + \frac{1}{2}\right)\hbar\omega_c \tag{2.29}$$

which labels an infinite series of equally-spaced levels. The $x$ part of the wavefunction is given by

$$u_n(x) = \frac{1}{\sqrt{l_0\sqrt{\pi}2_n n!}} H_n\left(\frac{x - x_0}{l_0}\right) e^{-(x-x_0)^2/2l_0^2} \tag{2.30}$$

where $H_n$ is the Hermite polynomial. We can visualize these wavefunctions as being localized (by the exponential decay term) in a stripe around $x_0$, with equal probability for detection anywhere along $y$. In that direction, the wavefunction varies only with a phase modulation set by the fixed ($x_0$-dependent) value of $k_y$.

If the sample has finite size given by the lengths $L_x$ and $L_y$, $k_y$ is quantized in (very small) units of $2\pi/L_y$. Hence we could relabel these states with an integer label $m$ given by

$$k_y = m\left(\frac{2\pi}{L_y}\right). \tag{2.31}$$

Recalling (2.27), the possible $x_0$ values can be expressed

$$x_0 = -l_0^2(m)\frac{2\pi}{L_y}. \tag{2.32}$$

Now $x_0$ must itself lie within the sample (be less than $L_x$), so $m$ is constrained to range from zero to $-m_{\max}$, with

$$L_x = l_0^2(m_{\max})\frac{2\pi}{L_y} \tag{2.33}$$

and hence $m_{\max}$ is the total number of states available for each $n$

$$m_{\max} = \frac{L_x L_y}{2\pi l_0^2}. \tag{2.34}$$

This quantifies the degeneracy of each of the harmonic-oscillator levels. Incidentally, this is the same number of levels that would exist within a segment of the $k$ quasicontinuum of energetic width $\hbar\omega_c$ in the absence of a magnetic field. So the Landau levels can be thought of as a grouping of a closely-spaced, non-degenerate 2D continuum into a coarsely-spaced degenerate ladder, with the size of the groups increasing with the magnetic field. As these harmonic energy gaps become larger, they begin to behave as subbands, having conductor- or insulator-like properties depending on the subband fullness (quantified by the level "filling factor" $\nu$).

The explicit form of the wavefunctions derived in this section – of stripes with some width in $x$, extending infinitely in the $y$ direction – bear no resemblance to the electron orbits we expect classically. We have a freedom in choosing the basis wavefunctions we use to represent the degenerate states in each Landau level, which comes from the freedom in the gauge choice when starting this problem. By solving the problem in the symmetric gauge, as in [65, ch22], we can obtain wavefunctions that better reflect the axial symmetry of the problem.

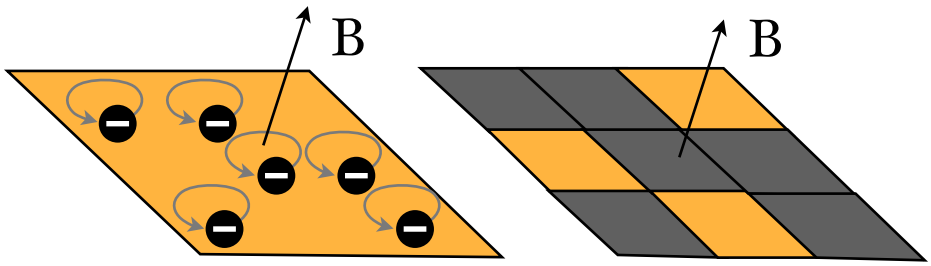


FIGURE 2.9. Cartoon picture of Landau levels. Each level of the harmonic motion has degeneracy associated with the size of the sample relative to the magnetic length $l_0$, given by $A_{\text{sample}}/2\pi l_0^2$

In a cartoon picture (Fig. 2.9), it is common to visualize the area of the sample divided into chunks of real space with area $2\pi l_o^2$, each of which can either be occupied or unoccupied by an

electron at each harmonic level. The linear scale of the segmentation scales linearly with the field strength. This intuitive picture is used, for example, in [45].

The specific form of the wavefunctions is not as important as the general result that a magnetic field $\vec{B}$, applied along $z$, replaces the $k$-space basis in the perpendicular plane with two new quantum numbers: $n$, the occupation nuber for the harmonic motion, and $m$, which labels the position of the oscillator center in real space. Because they transform the $k$-space picture into a real-space picture, localizing electrons on the length scale of $l_0$, magnetic fields are a useful probe of locality in the physics of interacting particles.

### 2.7. Magnetoexcitons

The effect of the magnetic field on exciton formation can be treated from two angles: either by treating the magnetic field as a perturbation to the exciton states, or by treating the Coulomb interaction as a perturbation to the Landau levels. Both regimes are accessible experimentally, and the behavior of the transition is a subject of ongoing theoretical research.

#### 2.7.1. Field as perturbation (low magnetic field)

A theoretical treatment of the exciton under a magnetic perturbation is given in Ref. [67]. Here, the expectation value of the Hamiltonian is expanded in the field strength $B$, so that

$$E(B) = E_0 + \gamma_1 B + \gamma_2 B^2 ... \tag{2.35}$$

with the coefficients $\gamma$ quantifying the shifts of the exciton. The authors find explicit forms for these coefficients and utilize a variational approach to minimize each coefficient in the expansion. Particular attention is paid to $\gamma_2$, the diamagnetic shift, since linear dependence on the field is already wrapped up in the exciton $g$ factor.

Symmetries of a quantum well are such that the second-order contribution to $\gamma_2$ can be made to vanish in the variational parameters, resulting in the expression

$$\gamma_2 = \frac{e^2}{8\mu c^2} \left\langle r^2 \right\rangle$$

where $\mu$ is the in-plane reduced mass of the exciton, and $\langle r^2 \rangle$ is the expectation value of the square of the electron-hole separation coordinate. In this way, the diamagnetic coefficient $\gamma_2$ serves as a measure of the electron-hole Bohr radius.

### 2.7.2. Interaction as perturbation (high magnetic field)

It is relatively easy to achieve magnetic field strengths where the quantization scale $l_0$ (2.28) becomes comparable to the exciton size. In this regime, the magnetic field can no longer be treated perturbatively, so we must consider the full Hamiltonian for the electron and hole in a magnetic field:

$$\frac{1}{2m_e}\left(-i\hbar\vec{\nabla}_e + e\vec{A}(\vec{r_e})\right)^2 + \frac{1}{2m_h}\left(-i\hbar\vec{\nabla}_h - e\vec{A}(\vec{r_h})\right)^2 - \frac{e^2}{4\pi\epsilon\left|\vec{r_e} - \vec{r_h}\right|}. \tag{2.36}$$

In the high-field limit, the approach is to proceed as if deriving the Landau levels, treating the interaction term as a perturbation. Gor'kov and Dzyaloshinskii [68] showed that, in the symmetric gauge $\vec{A} = \vec{B} \times \vec{r}/2$, the center-of-mass motion can be separated by introducing an operator

$$\hat{P} = \left(-i\hbar\vec{\nabla}_e + e\vec{A}(\vec{r_e})\right) + \left(-i\hbar\vec{\nabla}_h - e\vec{A}(\vec{r_h})\right) - \frac{e}{\mu_0}\left[\vec{B} \times (\vec{r}_e + \vec{r}_h)\right] \tag{2.37}$$

which commutes with the Hamiltonian. The corresponding conserved quantity is the total momentum of the exciton. In two dimensions, Lerner [69] showed that this results in an exciton wavefunction

$$\psi(\vec{r_e}, \vec{r_h}) = \exp\left[i\vec{R} \cdot \left(\vec{P} + \frac{e}{\mu_0}\vec{B} \times \vec{r}\right)\right] \exp\left(\frac{1}{2}i\gamma\vec{r} \cdot \vec{P}\right) \phi(\vec{r} - \vec{r_0}) \tag{2.38}$$

where $\vec{R}$ is the center-of-mass coordinate, $\vec{r} = \vec{r_e} - \vec{r_h}$ is the relative coordinate of electron and hole, and

$$\vec{r_0} = \left(\frac{\vec{B}}{\left|\vec{B}\right|} \times \vec{P}\right) l_0^2. \tag{2.39}$$

The parameter

$$\gamma = \frac{m_h - m_e}{m_h + m_e}, \tag{2.40}$$

not to be confused with the expansion coefficient in the previous section, quantifies the mass asymmetry, and the relative-motion wavefunction $\phi$ satisfies the Schrödinger equation in the form

$$\left(-\frac{\vec{\nabla}_r^2}{2\mu}+\frac{ie}{2\mu}\gamma\left[\vec{B}\times\vec{r}\right]\vec{\nabla}_r-\frac{e^2}{8\mu}B^2r^2-\frac{e^2}{\epsilon\left|\vec{r}+\vec{r}_0\right|}\right)\phi(\vec{r})=E\phi(\vec{r}) \tag{2.41}$$

where $\mu = m_e m_h/(m_e + m_h)$ is the reduced mass. Without the Coulomb term, solutions to this involve Laguerre polynomials. One proceeds by solving in orders of that term.

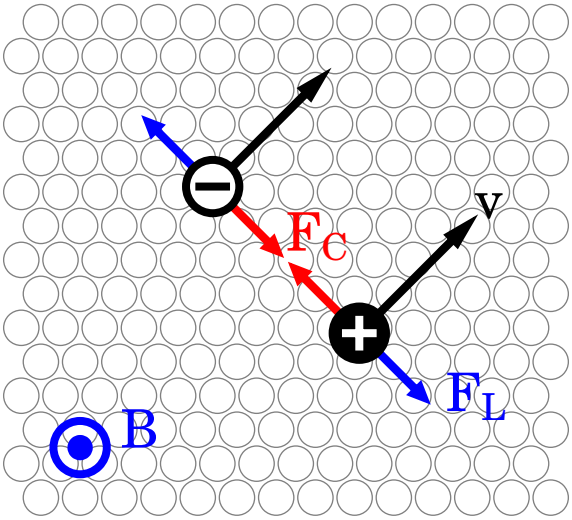


FIGURE 2.10. Conceptual view of a magnetoexciton: an electron and hole, traveling in tandem such that their mutual Coulomb interaction cancels the Lorentz force. The spatial extent of their wavefunction scales with the magnetic length.

Intuitively, this is motivated by the semiclassical picture shown pictorally in Fig. 2.10. In a strong magnetic field, the ground exciton state does not resemble a stationary hydrogenic system but instead a pair of carriers in motion, traveling side by side, with their Coulomb attraction serving to cancel out the Lorentz force applied by the magnetic field [70]. In this configuration they are called magnetoexcitons. This stands in contrast to what happens to single carriers: Whereas charge carriers transition from a free-particle continuum to localized Landau orbits, neutral excitons' wavefunctions are instead compelled to stop orbiting one another and move in straight lines instead [71].

The theoretical treatment results in the following magnetoexciton properties, summarized by Lozovik [70]: Their binding energy

$$E_B=\sqrt{\frac{\pi}{2}}\frac{e^2}{\epsilon l_0} \tag{2.42}$$

scales with $\sqrt{B}$. In terms of their shared momentum $\vec{P}$, they have a dispersion curve given by

$$E_X(\vec{P}) = -E_B e^{-\beta} I_0 \beta \tag{2.43}$$

where

$$\beta = \left(\frac{P l_0}{2\hbar}\right)^2 \tag{2.44}$$

and $I_0$ is the modified bessel function. For small $P$ this is parabolic dispersion with effective mass

$$M_{\text{eff}} = \sqrt{\frac{8}{\pi}} \frac{\epsilon \hbar^2}{e^2 l_0} \tag{2.45}$$

scaling as $\sqrt{B}$. At large $P$ the binding energy tends asymptotically to zero, relative to the Landau-level energy of the constituent carriers. Strictly speaking, there are no unbound states of the magnetoexciton, but in practical terms the large $P$ states are essentially broadly separated electron and hole Landau states. As $P$ tends to infinity so, too, does the mean electron-hole separation.

The magnitude of the electron-hole dipole is proportional to $\left|\vec{P}\right|$, and near zero the spatial extent of the wavefunction is characterized by the magnetic length $l_0$. This has the effect that an increased magnetic field effectively shrinks the exciton.

Of particular note for magnetoexciton is that the effective-mass dependence expressions has dropped completely out of the expressions for energy and dispersion, with the length scale being set entirely by the magnetic length $l_0$. This is a dramatically different picture than the case of the hydrogenic exciton, where the reduced mass was an important parameter.

The interplay between these two limits is a challenging theoretical problem, particularly with regard to the question of whether the heavy or light hole exciton is more strongly bound. For details, see Refs. [72–74].

# CHAPTER III

# SPIN COHERENCE IN A CDTE QW

Several of the most compelling future technologies mentioned in the introduction to this dissertation focus on the application of electron or hole spin. Spintronics, a re-imagining of electronics in which information is encoded by carrier spins rather than charge, promises to usher in a new class of devices. Spins also form an attractive candidate for encoding a bit of quantum information (qubit), since their comparatively long coherence times relative to other quantum systems in solids.

Spins in solids owe their relative robustness to decoherence in part to the fact that they form a non-radiative coherence. Since optical selection rules prohibit radiative relaxation, the system is not subject to optical mechanisms of decoherence.

This property also prevents direct optical manipulation of the spin, but the trion state forms a bridge through which this is possible using 2-photon transitions. Electromagnetically induced transparency (EIT), a coherent optical phenomenon which occurs in 3-level quantum systems, can demonstrate the quality of the spin coherence as a starting point for more advanced optical manipulations of the system. It also provides a potentially useful mechanism for implementing optical switching in quantum networks on its own [75].

In this chapter we explore this technique and its limits for a CdTe quantum well. As we will see, manybody interactions and external magnetic fields play an important role in semiconductor EIT. Portions of this chapter were previously published in proceedings of the Quantum Electronics and Laser Science Conference (CLEO: QELS) with co-authors Shannon O'Leary and Hailin Wang [6].

## 3.1. Electromagnetically Induced Transparency

Electromagnetically induced transparency (EIT) occurs in three-level quantum systems where two of the states are not dipole-coupled except through an intermediary third state. When a pumping electromagnetic field prepares a coherent superposition of these two states, transition amplitudes to the third state can destructively interfere with one another, rendering the medium transparent [76].

This is most effective in a so-called $\Lambda$-type quantum system, shown schematically in Fig. 3.1. Here, two lower-lying states $|a\rangle$ and $|b\rangle$ couple to a shared excited state $|e\rangle$ via two transitions $\Omega_a$

and $\Omega_b$ (where $\Omega$ denotes a rotating-frame Rabi frequency). In the following section, we derive a theoretical framework for this system and show that it exhibits EIT.

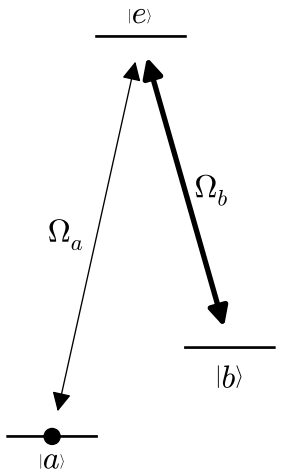


FIGURE 3.1. Schematic for a 3-level $\Lambda$ system. Two dipole transitions are coupled by fields having Rabi frequencies $\Omega$. Ideal EIT conditions exist when the population (black dot) lies initially in the state coupled by the probe (thin line) and not the more intense pump (thick line).

### 3.1.1. A three-level $\Lambda$-system

We are interested in three-level $\Lambda$ systems, where two states $|a\rangle$ and $|b\rangle$ are dipole-coupled through a shared excited state $|e\rangle$, but not to one another. Taking $|e\rangle$ to be at $E = 0$, the free evolution Hamiltonian is given by

$$H_0 = -\hbar\omega_{0a}|a\rangle\langle a| - \hbar\omega_{0b}|b\rangle\langle b|. \tag{3.1}$$

We can write the interaction terms separately for each of the two states, $V = V_a + V_b$. In the rotating-wave approximation,

$$V_a = -\vec{d_{ae}} \cdot \hat{\varepsilon}\frac{E_{0a}}{2}(\sigma_a \exp(+i\omega_a t) + \sigma_a^\dagger(\exp(-i\omega_a t))). \tag{3.2}$$

Or, adopting a Rabi frequency $-\vec{d_{ae}} \cdot \hat{\varepsilon}E_{0a}/\hbar$,

$$V_a = \frac{\hbar\Omega_a}{2}(\sigma_a \exp(+i\omega_a t) + \sigma_a^\dagger(\exp(-i\omega_a t))) \tag{3.3}$$

and likewise for $V_b$. There are two fields, $E_{0a}$ and $E_{0b}$, each coupling to only one transition, and we've chosen the phases so that each one is real. The total Hamiltonian is

$$H = H_0 + V_a + V_b. \tag{3.4}$$

We transform into a rotating frame with respect to the ground states, using the unitary transformation operator

$$U = \exp(-i\omega_a t|a\rangle\langle a| - i\omega_b t|b\rangle\langle b|). \tag{3.5}$$

Recalling that Hamiltonians transform according to (A.16), we obtain the transformed Hamiltonian

$$\tilde{H} = \hbar\Delta_a|a\rangle\langle a| + \hbar\Delta_b|b\rangle\langle b| + \frac{\hbar\Omega_a}{2}(\sigma_a + \sigma_a^\dagger) + \frac{\hbar\Omega_b}{2}(\sigma_b + \sigma_b^\dagger) \tag{3.6}$$

where we have defined $\Delta_a := (\omega_a - \omega_{0a})$ and $\Delta_b := (\omega_b - \omega_{0b})$. The first two terms represent free evolution in the ground states, and the second two represent coupling to the EM field.

### 3.1.2. An alternate basis

Consider using superpositions of the two ground states as an alternate basis. For example, we could rotate the $|a\rangle$ and $|b\rangle$ amplitudes through some real angle $\theta$.

$$|+\rangle = \cos\theta|a\rangle + \sin\theta|b\rangle \tag{3.7}$$

$$|-\rangle = -\sin\theta|a\rangle + \cos\theta|b\rangle. \tag{3.8}$$

This is a reversible transformation, with inverse:

$$|a\rangle = \cos\theta|+\rangle - \sin\theta|-\rangle \tag{3.9}$$

$$|b\rangle = \sin\theta|+\rangle + \cos\theta|-\rangle. \tag{3.10}$$

By substituting this into the free-evolution part of our Hamiltonian, we get

$$\begin{aligned}\tilde{H_0} =&\hbar \underbrace{(\Delta_a \cos^2\theta + \Delta_b \sin^2\theta)}_{=:\Delta_+} |+\rangle\langle+| + \hbar \underbrace{(\Delta_a \sin^2\theta + \Delta_b \cos^2\theta)}_{=:\Delta_-} |-\rangle\langle-| \\ &+ \hbar \underbrace{(\sin\theta\cos\theta(\Delta_b - \Delta_a)}_{=:\Omega_g}(|+\rangle\langle-| + |-\rangle\langle+|),\end{aligned} \tag{3.11}$$

where the extra term represents Rabi flopping at a rate $\Omega_g$ (since this new basis is not made of eigenstates). The twiddles still represent the rotating frame – we're denoting this second change of basis by explicitly writing out the new kets.

As for the interaction terms, recalling $\sigma_a := |a\rangle\langle e|$ etc., and defining $\sigma_\pm := |\pm\rangle\langle e|$, we can write

$$\tilde{V} = \frac{\hbar}{2}\underbrace{(\Omega_a\cos\theta + \Omega_b \sin\theta)}_{=:\Omega_+}(\sigma_+ + \sigma_+^\dagger) + \frac{\hbar}{2}\underbrace{(-\Omega_a\sin\theta + \Omega_b\cos\theta)}_{=:\Omega_-}(\sigma_- + \sigma_-^\dagger) \tag{3.12}$$

Notice that $\Omega_- = 0$ when $\Omega_b\cos\theta = \Omega_a\sin\theta$, that is, when

$$\tan\theta = \frac{\Omega_b}{\Omega_a}. \tag{3.13}$$

When we choose the appropriate angle for $\theta$, the $|-\rangle$ state has no direct coupling to the electric field. That is, both the $\Omega_a$ and $\Omega_b$ fields work only on population in $|+\rangle$, and $|-\rangle$ is affected solely through the Rabi rotation in $H_0$.

When this condition is met, we can further simplify the Rabi frequency corresponding to the effective field

$$\Omega_+ = \sqrt{\Omega_a^2 + \Omega_b^2} \tag{3.14}$$

and the free flopping frequency

$$\Omega_g = \frac{\Omega_a\Omega_a}{\Omega_a^2 + \Omega_b^2}(\Delta_b - \Delta_a). \tag{3.15}$$

The interaction term is

$$V = \frac{\hbar}{2}\sqrt{\Omega_a^2 + \Omega_b^2}(\sigma_+ + \sigma_+^\dagger). \tag{3.16}$$

### 3.1.3. Raman resonance

Even though the $|-\rangle$ state is formally decoupled from the electric field, it is still affected indirectly due to the Rabi flopping $\Omega_g$ in equation 3.11. This can be eliminated by matching the detunings of the two fields:

$$\Delta_a = \Delta_b =: \Delta. \tag{3.17}$$

This condition is known as Raman resonance. Here, the flopping frequency $\Omega_g = 0$, and $|-\rangle$ is entirely decoupled from effects of the optical field. It becomes a ***dark state***. Under these conditions, the Hamiltonian takes on the simplified form

$$H = \hbar\Delta(|+\rangle\langle+| + |-\rangle\langle-|) + \frac{\hbar}{2}\Omega_+(\sigma_+ + \sigma_+^\dagger). \tag{3.18}$$

As in the case of the two-level system (Appendix A), optical absorption results from having a substantial population available in the ground state of a dipole transition. However, if the population were to occupy this special superposition state, it would become invisible to the coupling laser fields ***even though*** that superposition is composed of two ground states. This is the basis of electromagnetically induced transparency.

### 3.1.4. 3-level optical Bloch equations

Returning to the Hamiltonian for the general case (3.6), we can obtain the equations of motion from the Heisenberg equation, adding phenomenological decay rates $\Gamma_{a,b}$ for spontaneous emission through either of the dipole transitions, and $\gamma_g$ for pure dephasing within the ground states. The master equation takes the form

$$\dot{\tilde{\rho}} = \frac{-i}{\hbar}[\tilde{H}, \tilde{\rho}] + \Gamma_a\mathcal{D}[\sigma_a]\tilde{\rho} + \Gamma_b\mathcal{D}[\sigma_b]\tilde{\rho} + \gamma_g\mathcal{D}[\sigma_g]\tilde{\rho} \tag{3.19}$$

where $\tilde{\rho}$ is the density matrix in the rotating frame, $\sigma_a = |a\rangle\langle e|$ and $\sigma_b = |b\rangle\langle e|$ are the dipole lowering operators. $\sigma_g = |b\rangle\langle b| - |a\rangle\langle a|$, and and $\mathcal{D}$ is the Lindblad superoperator (A.28). Note that, for simplicity, we are not including any extra dephasing terms for the radiative coherences.

By taking matrix elements of this master equation we arrive at three-level optical Bloch equations:

$$\dot{\tilde{\rho}}_{aa} = \frac{i\Omega_a}{2}\left(\tilde{\rho}^*_{ea} - \tilde{\rho}_{ea}\right) \qquad +\Gamma_a\tilde{\rho}_{ee} \tag{3.20}$$

$$\dot{\tilde{\rho}}_{bb} = \frac{i\Omega_b}{2}\left(\tilde{\rho}^*_{eb} - \tilde{\rho}_{eb}\right) \qquad +\Gamma_b\tilde{\rho}_{ee} \tag{3.21}$$

$$\dot{\tilde{\rho}}_{ea} = \frac{i}{2}\left(2\Delta_a\tilde{\rho}_{ea} - \Omega_a\tilde{\rho}_{aa} + \Omega_a\tilde{\rho}_{ee} - \Omega_b\tilde{\rho}_{ba}\right) \qquad -\tilde{\rho}_{ea}\gamma \tag{3.22}$$

$$\dot{\tilde{\rho}}_{eb} = \frac{i}{2}\left(2\Delta_b\tilde{\rho}_{eb} - \Omega_a\tilde{\rho}^*_{ba} - \Omega_b\tilde{\rho}_{bb} + \Omega_b\tilde{\rho}_{ee}\right) \qquad -\tilde{\rho}_{eb}\gamma \tag{3.23}$$

$$\dot{\tilde{\rho}}_{ba} = i\left(\Delta_a\tilde{\rho}_{ba} - \Delta_b\tilde{\rho}_{ba} + \frac{\Omega_a\tilde{\rho}^*_{eb}}{2} - \frac{\Omega_b\tilde{\rho}_{ea}}{2}\right) \qquad -\tilde{\rho}_{ba}\gamma_g \tag{3.24}$$

where $\gamma = \frac{\Gamma_a}{2} + \frac{\Gamma_b}{2} + \frac{\gamma_g}{4}$. The excited-state population is given by $\tilde{\rho}_{ee} = 1 - (\tilde{\rho}_{aa} + \tilde{\rho}_{bb})$, and the other coherence terms by complex conjugation.

### 3.1.5. Steady state

To obtain the absorption profile of either dipole transition, we need to solve for the steady state of the corresponding coherence term ($\tilde{\rho}_{ea}$ or $\tilde{\rho}_{eb}$). Rather than solve the system of five coupled equations, we will treat this perturbatively in the dark-state limit.

Informed by the basis change in the preceding section, we see that the ground state $|a\rangle$ is the dark state $|-\rangle$ in the limit where $\Omega_a << \Omega_b$. Physically, this corresponds to a very weak "probe" beam coupling the $\sigma_a$ transition and a stronger "pump" beam coupling the $\sigma_b$ transition. Accordingly, $\Omega_a$ will serve as the small parameter in our perturbative expansion around an initial state where all population is in state $|a\rangle$. To zeroth order in $\Omega_a$, $\rho^{(0)}_{aa} = 1$ and all other matrix elements are are zero.

We are interested in the radiative coherence underlying the probe transition. To first order, this is

$$\dot{\tilde{\rho}}^{(1)}_{ea} = -\frac{i\Omega_a}{2}\left(\tilde{\rho}_{aa} - \tilde{\rho}_{ee}\right) - \frac{i\Omega_b}{2}\tilde{\rho}_{ba} + \tilde{\rho}_{ea}\left(i\Delta_a - \gamma\right) \tag{3.25}$$

$$= -\frac{i\Omega_a}{2} - \frac{i\Omega_b}{2}\tilde{\rho}_{ba} + \tilde{\rho}_{ea}\left(i\Delta_a - \gamma\right) + \mathcal{O}\left(\Omega_a^2\right). \tag{3.26}$$

This is still coupled to the equation for the nonradiative coherence, which is

$$\dot{\tilde{\rho}}_{ba}^{(1)} = \frac{i\Omega_a}{2}\tilde{\rho}_{be} - \frac{i\Omega_b}{2}\tilde{\rho}_{ea} - \tilde{\rho}_{ba}\left(-i\Delta_a + i\Delta_b + \gamma_g\right) \tag{3.27}$$

$$= \quad - \frac{i\Omega_b}{2}\tilde{\rho}_{ea} - \tilde{\rho}_{ba}\left(-i\Delta_a + i\Delta_b + \gamma_g\right) + \mathcal{O}\left(\Omega_a^2\right). \tag{3.28}$$

It is straightforward to solve this system of two coupled equations in steady state. Setting $\dot{\tilde{\rho}}_{ba}^{(1)} = 0$,

$$\tilde{\rho}_{ba} = \frac{i\Omega_b\tilde{\rho}_{ea}}{2i\Delta_a - 2i\Delta_b - 2\gamma_g} \tag{3.29}$$

We can plug this into the equation of motion for the radiative coherence

$$0 = -\frac{i\Omega_a}{2} + \tilde{\rho}_{ea}\left(i\Delta_a + \frac{\Omega_b^2}{4i\Delta_a - 4i\Delta_b - 4\gamma_g} - \gamma\right) \tag{3.30}$$

which yields an expression for the steady-state coherence term

$$\tilde{\rho}_{ea} = \frac{2\Omega_a\left(-\Delta_a + \Delta_b - i\gamma_g\right)}{-4\Delta_a^2 + 4\Delta_a\Delta_b - 4i\Delta_a\gamma - 4i\Delta_a\gamma_g + 4i\Delta_b\gamma + \Omega_b^2 + 4\gamma\gamma_g} \tag{3.31}$$

The refractive index (A.61) and absorption coefficient (A.60) follow from this as $n \propto \mathrm{Re}\left[\tilde{\rho}_{ea}/\Omega_a\right]$ and $\alpha \propto \mathrm{Im}\left[-\tilde{\rho}_{ea}/\Omega_a\right]$. In Fig. 3.2 we plot the latter, which is proportional to the absorption coefficient seen by the probing beam as a function of $\Delta_a$.

### 3.1.6. Observing EIT in absorption spectroscopy

For small values of the pump coupling $\Omega_b$, the absorption spectrum shows the same Lorentzian lineshape as for a 2-level system, except for a sharp dip where $\Delta_a = \Delta_b$, the Raman resonance condition. This is electromagnetically induced transparency, resulting from the entire population residing in the dark state $|a\rangle$ while $\Omega_b$ pumps the "empty" transition $\sigma_b$.

The width of the absorption dip is reflective of the quality of the nonradiative coherence in the ground states. On the right side of Fig. 3.2 this is shown for several values of the ground-state dephasing rate $\gamma_g$: the absorption dip is sharper and deeper as the dephasing approaches zero.

In the presence of nonzero ground-state dephasing, EIT is less sensitive to the Raman resonance condition, but the degree of transparency is reduced. This can be compensated somewhat

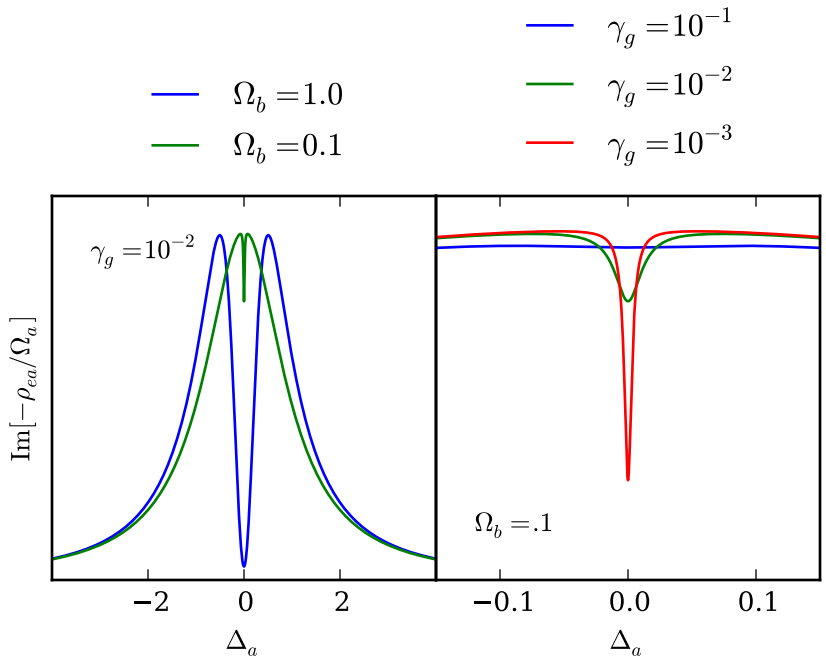


FIGURE 3.2. Simulated absorption spectrum with electromagnetically induced transparency. Imaginary part of the scaled steady-state coherence term, $\tilde{\rho}_{ea}/\Omega_a$, computed to first order in the probe power $\Omega_a$, as a function of the probe detuning $\Delta_a$. Decay rates are fixed at $\Gamma_a = \Gamma_b = 1$, setting the scale of the simulation, and $\Delta_b = 0$. In the left graph, the pump power $\Omega_b$ is varied between traces, and in the right graph, the ground-state dephasing rate $\gamma_g$ is varied between traces.

by increasing the pump power, at the expense of power broadening. This is evident on the left side of Fig 3.2, where for $\gamma_g = 0.01$ and $\Omega_b = 0.1$ the absorption is reduced by only 20%. By increasing the power to $\Omega_b = 1$, the transparency is nearly perfect but the dip width is no longer reflective of the nonradiative coherence.

### 3.1.7. Applications of EIT

EIT is of particular interest among nonlinear optical phenomena because of its coherent nature: it is a quantum interference phenomenon that renders the medium transparent. Any optical nonlinearity in which a pumping beam controls the absorption of another can lead to applications in all-optical switching. Since EIT is controlled by a quantum system, it may be considered a precursor to spintronic and quantum information applications. As a practical matter, EIT can be used to measure the quality of the nonradiative coherence using an optical experiment.

## 3.2. Implementing EIT in Semiconductors

Previous research has explored the multiple avenues for realizing EIT in semiconductors [77]. The most compelling approach utilizes the spin states of the carrier as the ground states $|a\rangle$ and $|b\rangle$, since they are relatively robust against decoherence. The excited state is provided by the heavy-hole trion.

A special property is responsible for the trion's role as the shared excited state. Like the electron, the trion has two spin configurations $\pm\frac{3}{2}$, each individually coupled to an electron having spin $\pm\frac{1}{2}$ respectively by absorbing a circularly-polarized photon (carrying angular momentum $\pm 1$) traveling along the spin axis. In this configuration, shown in Fig. 3.3, the system looks more like two independent 2-level systems than the 3-level $\Lambda$ system necessary for EIT.

In quantum dots and wells, confinement induces hole spins to quantize along the growth axis of the heterostructure, an effect which can outcompete the influence of an external magnetic field [78]. By applying an in-plane magnetic field (Voigt geometry), electrons quantize along the transverse axis $x$, while holes remain "pinned" in the growth direction $z$. For light incident along $z$, this introduces linearly-polarized cross-couplings between the up- and down-spin halves of the system. As shown in Fig. 3.4, this results in the formation of two optical $\Lambda$ systems with cross-polarized selection rules.

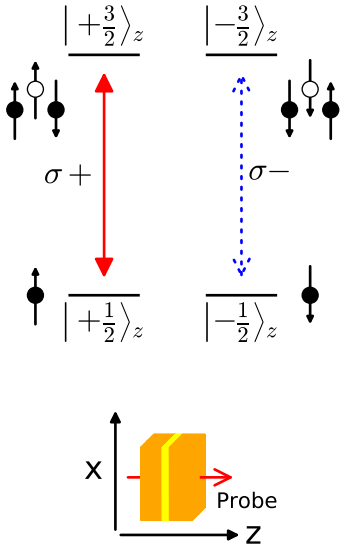


FIGURE 3.3. Spin selection rules for trions in the absence of magnetic field.

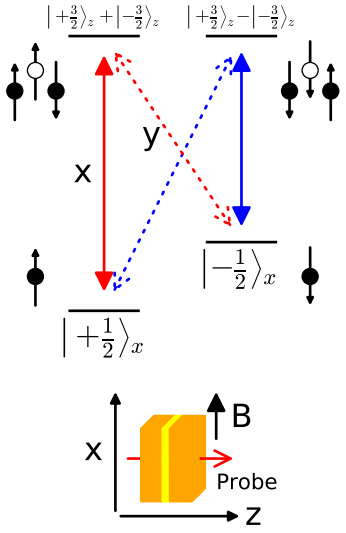


FIGURE 3.4. Spin selection rules for trions in a Voigt magnetic field.

### 3.3. Experimental Study: EIT in a CdTe QW

In this section we demonstrate EIT that utilizes the spin coherence of resident carriers in an n-doped CdTe QW. Pursuing this in wells, as opposed to dots, is of special interest since some applications of EIT require an optically dense ensemble, rather than a single emitter. For these applications, a QW-confined spin ensemble presents greater optical density, and less inhomogeneous broadening, than an ensemble of QDs.

A high quality n-doped CdTe QW is used in our study. The sample consists of $10$ periods of $10$ nm CdTe wells and $45$ nm $Cd_{0.84}Zn_{0.16}Te$ barriers, grown on a $Cd_{0.88}Zn_{0.12}Te$ substrate that is transparent near the band edge. The modulation doping density is estimated to be $3 \times 10^{10}/\text{cm}^2$. Both neutral and charged excitons (trions) have been observed in this sample previously [12]. Fig. 3.5 plots the absorption spectrum of the sample obtained at $T = 10\,\text{K}$, showing clearly resolved heavy-hole (HH) exciton and trion (charged exciton) resonances, in the absence of a magnetic field. This picture is qualitatively unchanged for small magnetic fields and small changes in temperature, apart from some energetic shift. The electron $g$-factor, determined from separate spin precession measurements, is $|g_e| = 1.6$.

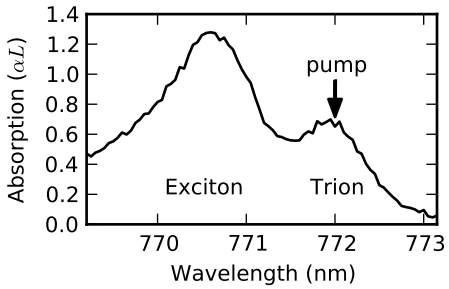


FIGURE 3.5. Linear absorption spectrum of a modulation-doped CdTe QW obtained at $10$ K.

A similar study was conducted by O'Leary in a GaAs mixed-type quantum well [17]. Relative to that prior work, much larger Zeeman splittings are possible in CdTe due to its higher $g$-factor. In addition to greater spectral separation of the relevant resonances, this can thermally depopulate the upper spin state and result in greater spin polarization. Recall from section 3.1 that a maximally polarized starting state is ideal for generating EIT.

### 3.3.1. Results: Continuous-wave EIT at low field

Continuous-wave EIT experiments were carried out on the trion transition with a small in-plane magnetic field of $B = 0.6\,\mathrm{T}$ and with the pump and probe beams having orthogonal linear polarizations. Figure 3.6 shows the differential transmission (DT) spectrum obtained at $T = 10\,\mathrm{K}$, with the pump centered at 772 nm. Two spectrally-sharp coherent Raman resonances are observed, corresponding to the two $\Lambda$-type three-level systems shown in the insets. The separation between the two resonances, $\pm 13\,\mathrm{GHz}$, is consistent with $|g_e| = 1.6$ in CdTe. Neither has a magnitude exceeding $0.2\%$ of the trion absorption.

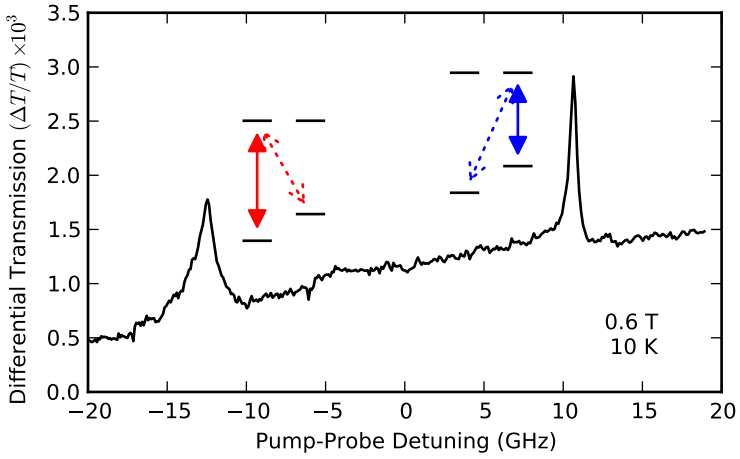


FIGURE 3.6. Coherent Raman resonances in CdTe QW, continuous-wave experiment. DT response obtained by pumping near the trion absorption resonance at $10$ K in the presence of a $0.6$ T in-plane magnetic field.

This small value of the electron splitting is insufficient to thermally depopulate one of the electron spin states. In this limit, increasing the pump intensity beyond the $\chi(3)$ regime leads to excessive optical excitations of excitons and trions, leading to collision-induced decoherence of the dipole transiton rather than stronger transparency. This may be avoided by applying still higher magnetic fields.

### 3.3.2. Results: Pulsed EIT at increased field

In a second experiment, a $5$ T magnetic field was applied using a superconducting magnet, while EIT was induced using a pulsed picosecond laser. In a pulsed configuration, high field intensities can be achieved for short times, without heating the sample as much as in a CW EIT experiment.

The drawback is that the widths of EIT dips is limited by the bandwidth of the pulse, and not by the spin coherence time. However, at 5 T, Zeeman splittings of the spin are big enough to be spectrally resolved. This, combined with a lower operating temperature, should manifest an improved EIT signal.

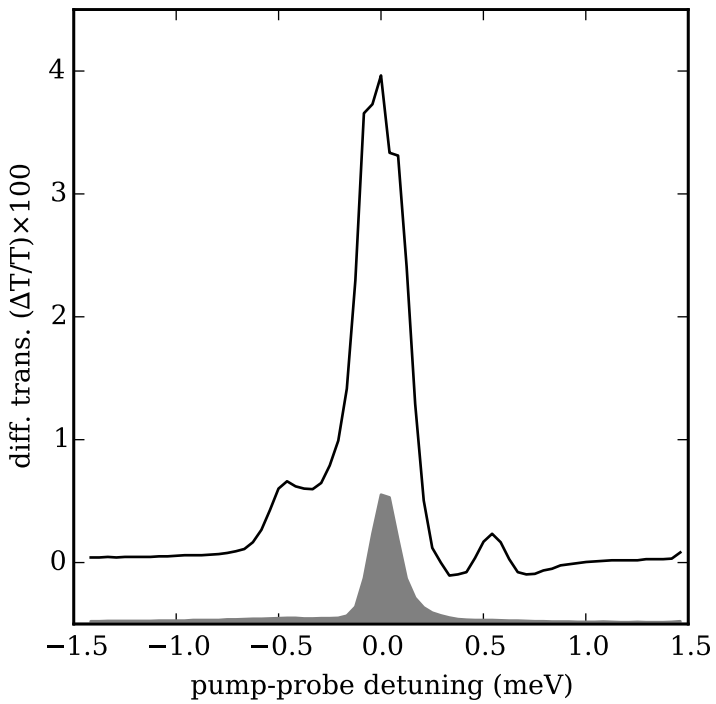


FIGURE 3.7. Coherent Raman resonances in CdTe QW, pulsed experiment. Differential transmission of CdTe QW, as a percentage of the trion absorption, when pumped by a 2 mW pulse centered at 771 nm. The sample is held at 5.3 K, with a 530 ps pump-probe delay and a 5 T magnetic field applied in the Voigt direction. Pump spectrum shown schematically in gray (arbitrary units, not to scale).

A differential transmission spectrum is shown in Fig. 3.7. The central peak corresponds to spectral hole burning by the pump, an incoherent effect. As in the CW experiment, EIT manifests as two spikes in transmission when over- or under-tuned by the $\sim 0.5$ meV Zeeman splitting. These EIT signals, while larger than the CW case, are still less than $1\%$ of the total absorption. Other researchers

[79] achieved EIT signals of several percent by using slightly different conditions. Even so, absorption reductions of less than $10\%$ can hardly be considered "transparency".

### 3.4. In Search of Spectrally-Resolved EIT

The results in the preceding section display clearly the spectrally-sharp Raman resonances that form the basis for EIT in semiconductors. However, the degree of transparency is limited to less than $10\%$ due to a variety of factors.

Most importantly, **the transition being pumped on is not empty**. Even when $\Delta E \leq k_B T$, as in the pulsed-EIT experiment, it is still less than the linewidth of the trion transition. Hence, when the upper spin state becomes depopulated, the pumping field is still resonantly exciting trions of the opposite spin orientation. Spectral resolution of the spin states would be necessary to avoid this.

Secondly, **strong optical excitations induce detrimental manybody effects**. As shown in Fig. 3.5, trion and exciton resonances overlap strongly, and this is the case at both zero field and at $5$ T. Therefore, strong pumps on the trion also generate excitons, which scatter with the electron gas and lead to reduced dipole coherence in both of the relevant transitions [17].

In principle, there is reason to believe that both quandries may be addressed by using still higher magnetic fields. Increasing the electron Zeeman splitting to the point where it exceeds the trion linewidth would enable spectral resolution of the individual spin states. In addition, trions are known to be more strongly bound at high fields, leading to lessened overlap with the exciton resonance and potentially fewer manybody excitations.

For these reasons, high magnetic fields hold the promise of creating an ideal EIT platform in semiconductors. However, the precise behavior of excitons and trions in high Voigt fields is understudied with respect to longitudinal magnetic fields (Faraday geometry), for reasons detailed in the next chapter. In the next section we conduct our own study excitons and trions in high Voigt fields as a precursor to their application as an EIT platform.

#### 3.4.1. Spectroscopic survey: High Magnetic Field

Absorption spectra of the CdTe QW were measured using attenuated pulses from a broadband Ti:Sapphire laser. An Optical Parametric Amplifier (OPA) was used to tune the pulses to the appropriate wavelength. In-plane magnetic fields (Voigt geometry) were applied using the $25$ T Split

Florida-Helix resistive magnet at the National High Magnetic Field Laboratory in Tallahassee, Florida. The sample was cooled to 6 K using the cryogenic insert.

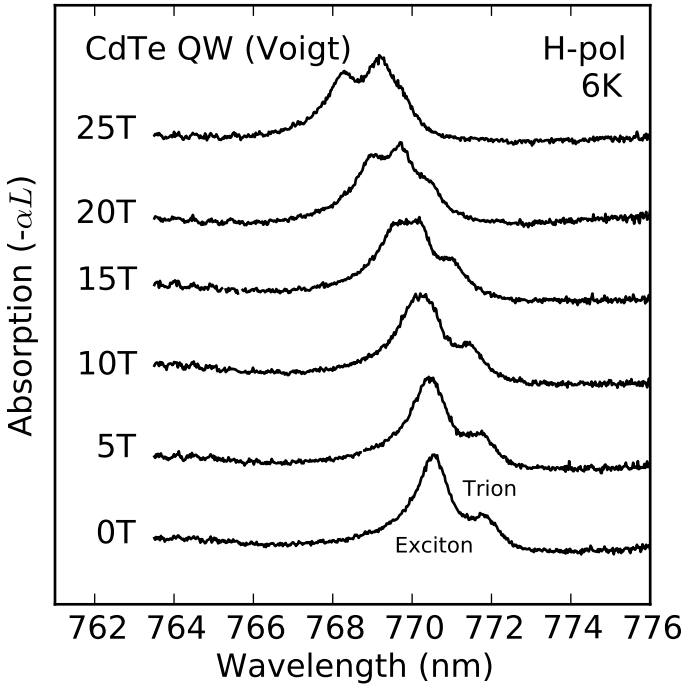


FIGURE 3.8. Absorption spectra of CdTe QW in increasing Voigt fields. Sample held at 6 K. A horizontally-polarized probe was used (perpendicular to the magnetic field axis); vertically-polarized spectra were qualitatively the same. Lines have been vertically offset for clarity.

Fig. 3.8 shows the CdTe absorption spectrum as a function of the applied field. The oscillator strength of the trion is observed to reduce as the field is increased. A splitting in the exciton resonance leads to a greater overlap with the trion. This behavior is independent of polarization of the probing field. The spectral center of each resonance, determined by fitting to the sum of several Lorentzian distributions, is shown in Fig. 3.9.

### 3.5. Trionic Instability in High Voigt Fields

The dramatic reduction of the trion oscillator strength with increasing magnetic field precludes its use as an ideal EIT platform. These results indicate that the trion complex becomes unstable at high magnetic fields, before splittings of the desired magnitude are achieved. This was not an anticipated result.

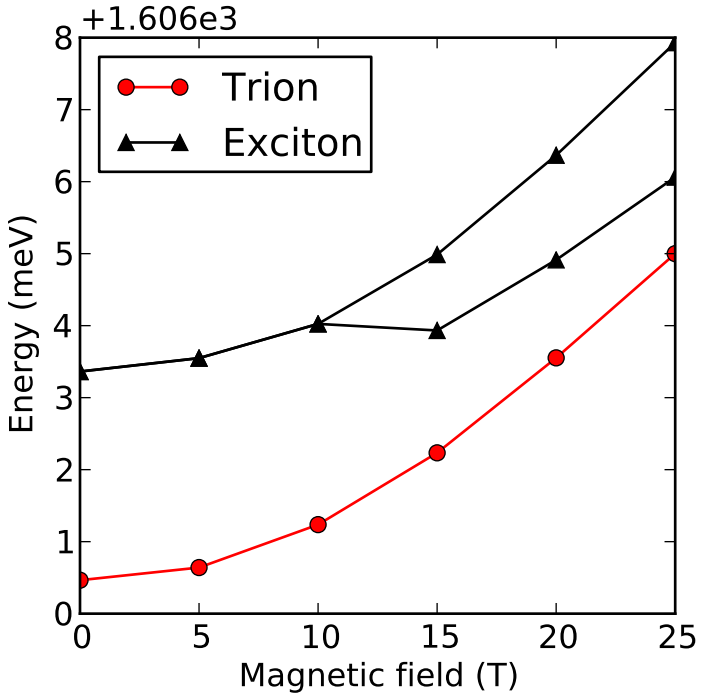


FIGURE 3.9. Spectral position of CdTe absorption resonances vs. magnetic field. Values obtained by fitting Lorentzian functions to the absorption spectra in the previous figure. All are subject to a shift to higher energies, with increasing exciton-trion overlap.

Even if this were not the case, however, the strongly overlapping exciton would likely mask optical access to the trion via manybody effects. The exciton is seen to exhibit a strong Zeeman splitting, as had been previously observed in an undoped sample [80]. The trion, in contrast, disappears before any splitting may be clearly seen. This effect overwhelms any increase in the trion's binding energy, meaning that CdTe QWs in are likely not a viable candidate for high-magnitude EIT, even at intermediate field strengths (e.g. 15 T).

### 3.6. Conclusions: No Ideal EIT Platform

In this chapter, we pursued an ideal platform for high-transparency EIT in a CdTe QW. While this system exhibits the basic structure for EIT at low magnetic fields, the low degree of transparency achieved limits its relevance for applications requiring a high optical density. Although marginal improvements can be made at magnetic fields of 5 T, these do not scale to high magnetic fields. We observed two effects that preclude an ideal EIT platform at high Voigt fields, including a breakdown in the trion complex.

# CHAPTER IV

# EXCITONS AND TRIONS IN HIGH MAGNETIC FIELDS

In the previous chapter, we ventured into the realm of high magnetic fields. Here we saw the creation probability for trions vanish, overwhelming the Zeeman splitting that was desired as part of the experimental design. This highlights an important consideration: the optical "excited state" of the electron spin system is not a reconfiguration of the electron within a fixed orbital structure – as would be the case for atoms – but instead the creation of a distinct quasiparticle that is bound to it. The circumstances of that pair's creation event are impacted not only by its binding to the existing electron, but also by the density of screening carriers and the presence of an applied magnetic field.

The orbital structure of the trion has been extensively studied in both theoretical [28, 32, 81] and experimental contexts [10, 29, 30, 38]. As a true manifestation of the three-body problem, a closed-form expression of its wavefunction is generally not possible. Experimental approaches to the problem have largely focused on photoluminescence (PL) measurements, which are an effective probe of trion state occupation, but yield only partial information about its structure. In particular, the density of states can be obtained from PL only by making rate-equation models.

In this chapter, we examine how the structure of exciton and trion complexes is modified by an external field. Our focus is an experimental study in which we measure direct absorption of the quasiparticle spectrum in fields up to $25$ T.

## 4.1. Electronic Motion in Applied Magnetic Fields

As we saw in Section 2.6, an external magnetic field breaks an important symmetry with regard to the spatial part of carrier wavefunctions. In the absence of magnetic fields, these are the Bloch wavefunctions, which describe a continuum of free-particle-like eigenstates labeled by (and with the energy solely determined by) the crystal momentum $\vec{k}$. This picture completely changes in a magnetic field, where motion perpendicular to the field vector $\vec{B}$ becomes quantized into Landau levels. With $\vec{B}$ along the $z$ axis, transverse motion is described not by momentum-space vectors $k_x$ and $k_y$ but by $n$, labeling the Landau level that is occupied, and $m$, which labels degeneracy related to a real-space coordinate. In this way, the field localizes the motion of carriers.

In a bulk semiconductor, the new expression for the energy is

$$E_{n,m}(k_z) = \hbar\omega_c \left(n + \frac{1}{2}\right) + \frac{\hbar^2 k_z^2}{2m_e}$$

where $k_z$ remains a continuous variable. In a quantum well, this can be quantized by the spatial confinement, provided the growth axis is parallel to the magnetic field (Faraday geometry). Magnetic field effects are most pronounced in this arrangement, since the carrier states are now quantized in all three dimensions.

Exciton wavefunctions are also transformed by the field, which we surveyed in Section 2.7. When the magnetic length scale, $l_0 = \sqrt{\hbar/eB}$, becomes smaller than the Bohr radius, excitons gradually lose their hydrogenic resemblance in favor of a new structure, the magnetoexciton, in which the Coulomb attraction is counterbalanced by opposite Lorenz forces. The crossing-over between these two regimes is a challenging theoretical problem [72, 82].

The trion state, too, takes on a richer structure in the presence of magnetic fields. As we will see, the presence of Landau degeneracy is instrumental in binding the triplet state of the trion, which has been shown to eventually become the trion's ground state [30]. We do not examine the singlet-triplet crossing in this chapter, but focus instead on detailed measurements surrounding its emergence. Spin plays a crucial role in identifying this new trion state.

### 4.2. Fine Structure of Excitons and Trions

While the magnetic field has the effect of introducing degeneracy in the spatial wavefunctions of carriers, it also lifts the degeneracy associated with their intrinsic spin. As seen in the preceding chapter, intrinsic spin is an important consideration for determining the optical selection rules of exciton and trion transitions.

In the previous chapter's experiment we saw the exciton split with an in-plane g-factor of $|g| = 1.6$, which primarily came from the electron, since the hole is pinned in the growth direction. In the Faraday geometry, hole pinning is not a factor, so the Zeeman splitting of excitons and trions follows from the g-factors of the individual carriers in a more straightforward way.

This section follows the convention of Ref. [38], where for $g > 0$ the spin-up (spin-down) state is higher (lower) in energy, for both electrons and holes. We assume $g_e < g_h < 0$. Exciton energies are

given by

$$E_X(B) = \left(g_e S + \frac{g_h}{3} J\right) \mu_B B$$

where the electron spin $S = \pm\frac{1}{2}$ and the heavy-hole spin $J = \pm\frac{3}{2}$. Note that in this the g-factor applies to the sign of the spin only.

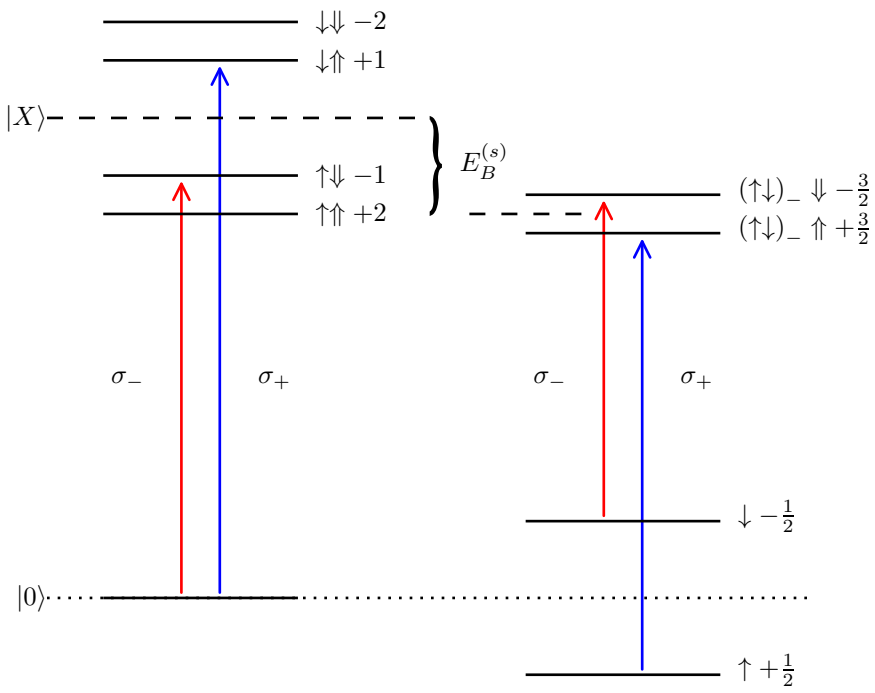


FIGURE 4.1. Optical selection rules for excitons and singlet trions. Fine structure shown for heavy-hole excitons (left side) and singlet trions (right side) with $g_e < g_h < 0$. Electron spin states are denoted with $\uparrow$ and $\downarrow$ and hole states by $\Uparrow$ and $\Downarrow$. The spin singlet state $(\uparrow\downarrow - \downarrow\uparrow)/\sqrt{2}$ is abbreviated $(\uparrow\downarrow)_-$.

The four possible states are shown on the left side of Fig. 4.1. Since circularly-polarized light can only carry spin of $\pm 1$, only two of them are optically accessible. Because the electron and hole have differing g-factors, the ordering of exciton states does not necessarily follow the total spin of the

complex, and in this case they do not. By limiting ourselves to the two optically-accessible exciton states we can define an exciton g-factor

$$g_X = g_h - g_e.$$

Trion states are shown on the right side of Fig. 4.1. These lie lower than the exciton states by an amount equal to the binding energy of the "extra" electron. For reasons explained in the next section, the two electrons form a singlet state, and the two trion states are separated only by the hole Zeeman splitting, which is typically small. However, the optical transitions are still separated by an amount equal to the exciton splitting due to the field dependence of the electrons, which form the ground state of the transition.

### 4.3. Triplet State of the Trion

Because the electrons in the trion are two indistinguishable fermions, they are described by a wavefunction that is antisymmetric when interchanging their coordinates. This asymmetry can be carried either by the spatial part of the wavefunction, or by the part labeling intrinsic spin. As a result, two classes of trions exist: singlet trions and triplet trions, where the name refers to the intrinsic spin configuration of the two electrons.

As in other two-electron atoms like helium, exchange symmetry is the most important consideration in determining how strongly each class of trion is bound. A variational proof shows that in the absence of a magnetic field, the ground state of a two-fermion system necessarily has a symmetric spatial wavefunction, and therefore forms a spin singlet [83]. The electrons need not interact for this to be true, except via exchange. In keeping with this, singlet trions form the ground state (and indeed the only bound trion state) at zero field.

The constraints imposed by exchange are loosened dramatically when degeneracy exists in the spatial part of the wavefunction, to the point where interaction terms become important. In that scenario, electrons can occupy separate orbitals at no cost in energy, and by doing so in an antisymmetrical way they maximize their mean separation in space. This in turn minimizes Coulombic repulsion and screening of the central positive charge. As a result, it is energetically advantageous for the spatial wavefunction to carry the asymmetry, with the spin part forming a triplet.

This principle, known as the first of Hund's rules, explains why triplets typically lie lower than singlets in the structure of atoms like carbon. In that case, triplets lie lower due to the threefold degeneracy of the $p$ orbital, but it is applicable whenever the spatial part of the wavefunction has some degeneracy. In our case, this comes from Landau quantization.

Because the trion carries charge, its spatial wavefunction becomes quantized into Landau levels by an applied magnetic field, inducing a degeneracy that scales linearly with the field strength. For this reason, triplet trions become bound in a magnetic field, and can even cross the singlet to become the ground state in the high-field limit [10].

### 4.3.1. Fine structure

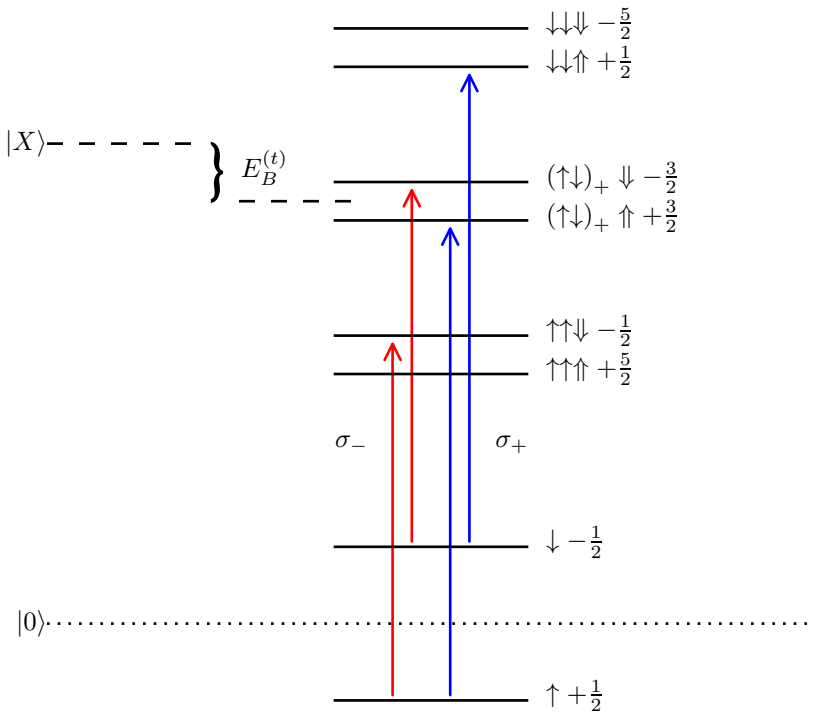


FIGURE 4.2. Optical selection rules for triplet trions. Notation and parameters are as in Fig. 4.1, with the spin state $(\uparrow\downarrow + \downarrow\uparrow)/\sqrt{2}$ is abbreviated $(\uparrow\downarrow)_+$. $E_B$ is not to scale with the zeeman splittings shown.

The six possible spin configurations of the triplet trion are shown in Fig. 4.2. Only four are optically accessible, and because the extra-electron binding energy $E_B$ is so small for the triplet states, most are not even bound. The lowest-lying optically-accessible state has spin $-\frac{1}{2}$, and is coupled by a field that is co-polarized with the lower-energy exciton and trion transitions (shown in Fig. 4.1).

It's important to note that multiple orbital configurations exist for the triplet trion, with potentially stronger binding energy $E_B$. These states are labeled by the orbital magnetic quantum number $m$, and for nonzero values of $m$, all six states can be optically forbidden. Even so, these so-called "dark triplets" are regularly observed in photoluminescence studies due to phonon-assisted decay processes.

## 4.4. Experimental Study

We have conducted an experimental study of excitons and trions in high magnetic fields. In contrast to prior work in this area, which typically make use of modulation-doped samples, we utilize a GaAs Mixed-Type Quantum well (MTQW), the structure of which was described in Section 2.5.1. This gives us optical control of the carrier density in the well, which is useful for distinguishing resonances of excitons (which dominate for low electron densities) and trions (which appear only when excess electrons are present). Optical doping was provided by a continuous wave HeNe laser at $632$ nm, with intensity controlled by an acousto-optic modulator.

The choice of GaAs has other structure-independent considerations: Most notably, a $g$-factor of $|g_e| = 0.27$, which is much smaller than in CdTe [17]. In addition to a smaller spin splitting, the light-hole and heavy-hole excitons lie much closer together, and there is an increased role of valence band mixing, which we will also examine.

This work is also distinct from many prior studies in that we measure this spectrum in optical absorption, not photoluminescence. This provides a direct measurement of the density of states for each complex, independent of its population. Peak sizes in the measurement unambiguously represent the oscillator strength of the transition, making other features (such as the Zeeman splitting) more clear. To this end, an $800$ nm pulsed Ti:Sapphire laser (Coherent Vitesse) provided a probing field, whose FWHM of approximately $10$ nm is broad enough to serve as a white light source for our purposes. High-resolution spectra were obtained by a liquid nitrogen-cooled CCD camera mounted to

a 750 mm spectrometer (Princeton Instruments Acton SP2750), with a grating having 1200 grooves per mm.

The sample was held at 10 K inside a helium flow cryostat. Magnetic fields were applied using the 25 T Split Florida-Helix resistive magnet at the National High Magnetic Field Laboratory in Tallahassee, Florida. This split-bore magnet is designed to apply fields in the Voigt geometry. To apply a field in the Faraday direction, a specialty sample holder mounted the sample flat between a bottom prism implementing a 90-degree turn and a top retro-reflecting prism. The bottom prism made use of a silvered hypotenuse to maintain circular polarization, while the top prism reflected light directly back toward the sample. Ultimately the probing field passes through the sample twice before being measured, with the polarization reversal by the prism countering the effective change in direction of the magnetic field.

### 4.4.1. Spectroscopic survey

The evolution of the absorption spectrum with magnetic field is shown in Fig. 4.3. For each field strength, traces are shown in the presence and absence of optical doping, which distinguishes peaks associated with excitons from those associated with trions. The intensity of the doping laser, 4.8 mW/cm², is estimated to inject on the order of $10^{10}$ electrons/cm².

Without doping, we observe two peaks identifiable as heavy- and light-hole excitons. In the presence of doping, exciton lines weaken (due to screening by the electron gas), and heavy-hole trion peaks appear to the low-energy side of the corresponding excitons. At exceptionally high fields, a second peak emerges from the low-energy shoulder of the exciton, for $\sigma_-$ polarized light only. This is what we expect to see for the trion's triplet state becoming bound.

Fig. 4.4 plots how the exciton peaks' positions evolve in a magnetic field, illustrating that they both become stronger and shift to higher energies (diamagnetic shift). This view of the data is obtained from spectra of the undoped well by fitting them to the sum of several Lorentzian functions. Both species of exciton are subject to a Zeeman splitting that is opposite for light-hole excitons as it is for heavy-hole excitons, confirming the spin structure of the transitions shown in Fig. 2.4.

The evolution of lines in the optically-doped well is shown in Fig. 4.5, where the diamagnetic shift of the heavy-hole exciton has been subtracted for clarity. The Zeeman splitting of the trions matches that of the heavy-hole excitons, offset by an amount equal to the binding energy of the

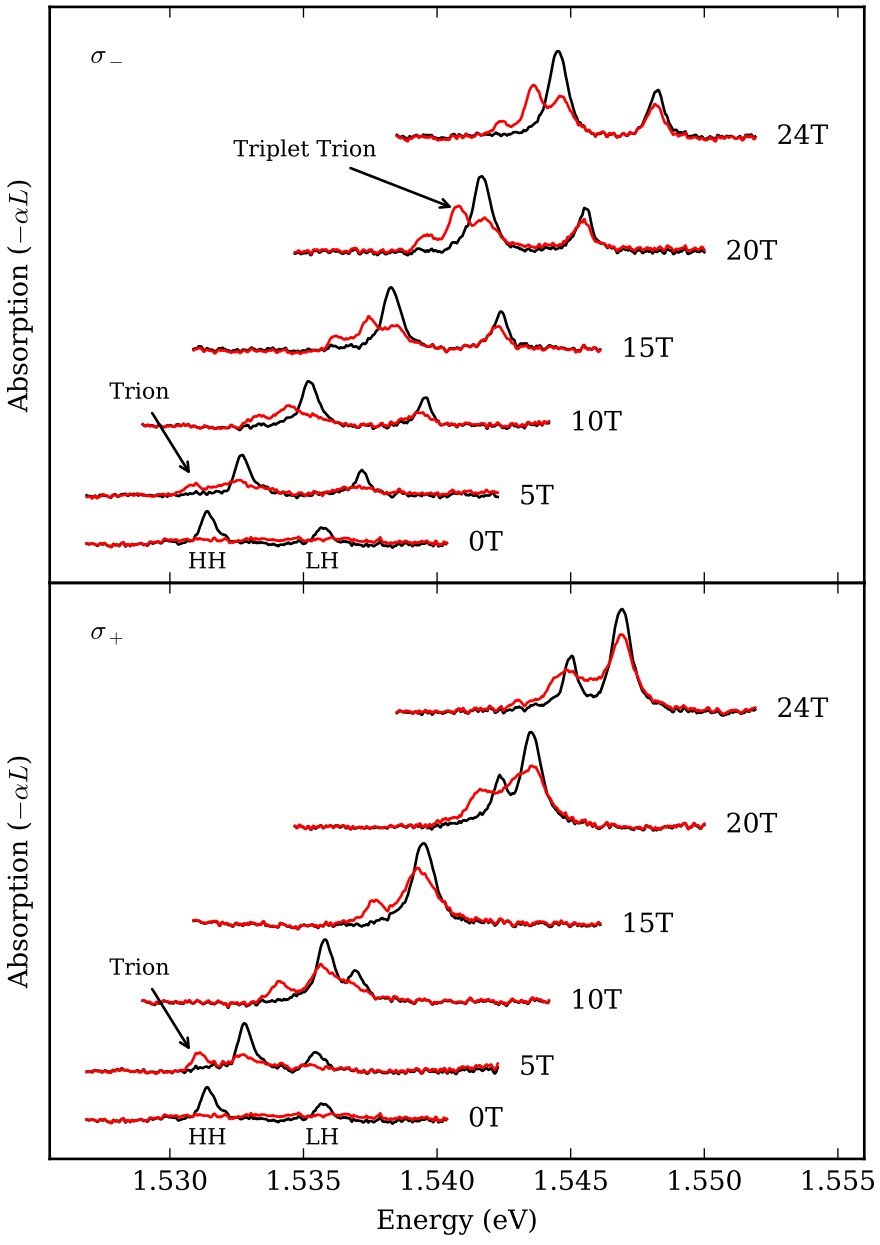


FIGURE 4.3. Magnetic field dependence of MTQW absorption spectrum with (red lines) and without (black lines) optical doping, in the Faraday geometry. Lines have been offset vertically for clarity. Shown separately for left- and right-hand circularly polarized light. Sample was held at 10K, with the electron-injection laser intensity tuned to 4.8 mW/cm$^2$.

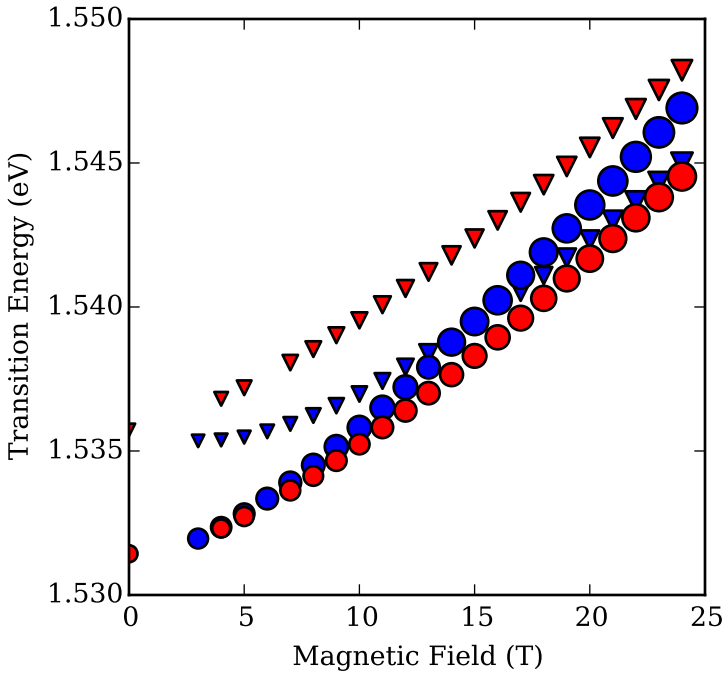


FIGURE 4.4. Spectral position of MTQW exciton absorption resonances vs. magnetic field. These are extracted from absorption spectra obtained without optical doping, in which no trion lines are observed. Heavy-hole excitons are denoted by circles, and light-hole excitons by triangles, with the size of the marker illustrating the relative strength of the absorption line. Marker color indicates two values of cross-circularly polarized light used in the experiment.

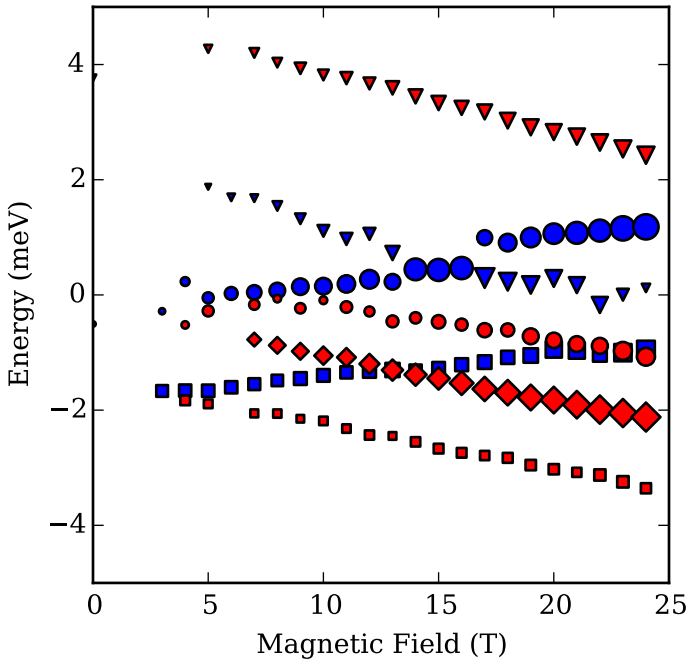


FIGURE 4.5. Energy of exciton and trion absorption peaks relative to the overall diamagnetic shift of the exciton. Obtained with optical doping, with the electron-injection laser intensity tuned to 4.8 mW/cm². Marker sizes, colors and shapes are as in the previous figure, with the addition of singlet trions (squares) and triplet trions (diamonds).

additional electron. The triplet trion, which appears for one polarization only, is co-polarized with the lower energy singlet trion, as expected from the energy levels detailed in Figs. 4.1 and 4.2.

Two important physical parameters may be isolated from these data: the $g$-factors and binding energies. These are visualized in Figs. 4.6 and 4.7.

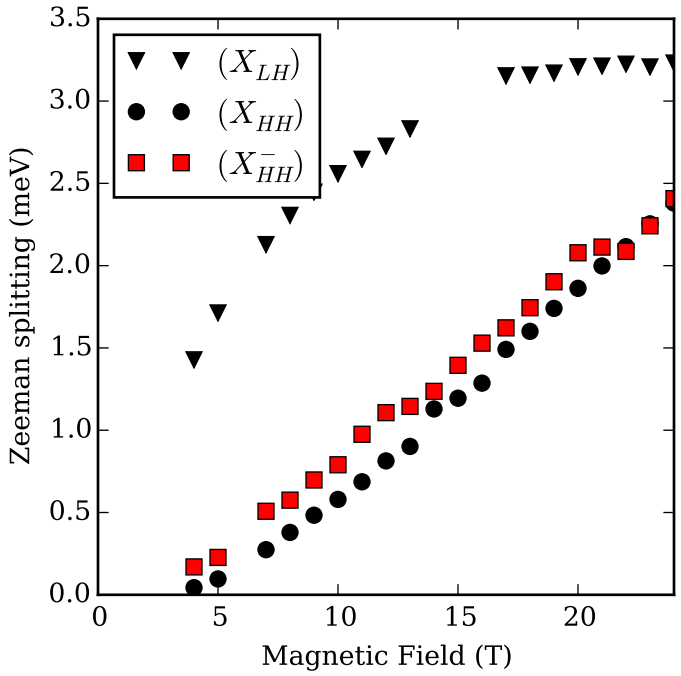


FIGURE 4.6. Zeeman gap of LH excitons, versus that of HH excitons and trions. Exciton Zeeman gaps obtained from spectra of the undoped well; singlet trion Zeeman gap obtained from spectra where the doping field is active.

Fig. 4.6 plots the magnitude of the splittings for the three bodies which appear in pairs. This behavior is matched for the heavy-hole exciton and its charged state, the singlet trion. Both bodies display a $g$-factor of approximately 2 at fields above 5 T, but exhibit a much smaller one at lower fields. In contrast, the light-hole exciton splits readily at low fields before the splitting becomes saturated at a value of 3.2 meV. This opposite behavior is be reflective of an underlying band-mixing process between the two, resulting in a field-dependent $g$-factor for the hole. This behavior is consistent with observations in a prior study [38].

Fig. 4.7 plots the energy of the trion peaks, alone, with both the diamagnetic and Zeeman terms subtracted. This is the binding energy for the second electron in either body. It is clear that both

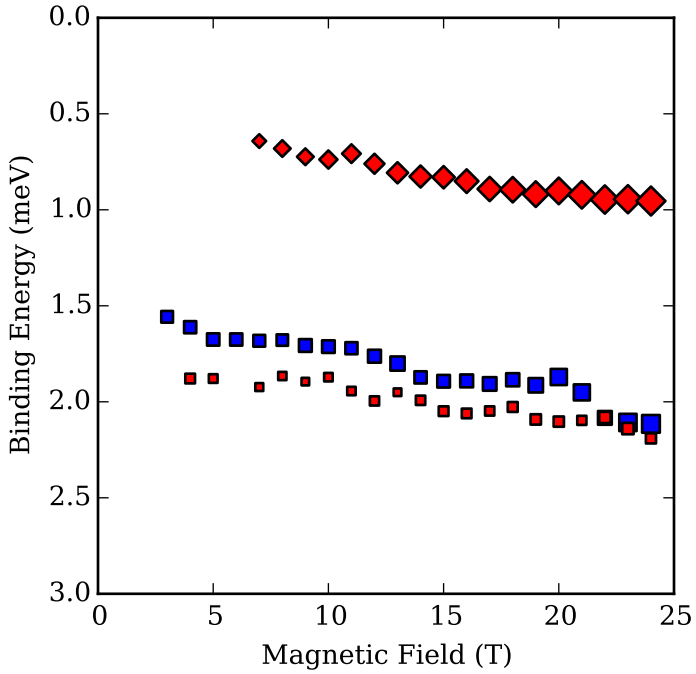


FIGURE 4.7. Observed binding energy of second electron in singlet and triplet trions. Obtained from the spectral position of the trions relative to the exciton with which they are co-polarized.

singlets and triplets become more tightly bound in a magnetic field, at a seemingly comparable rate. At the maximum field accessible in this experiment, the observed triplet line is only half as strongly bound as the singlet trion. However, its oscillator strength is approximately three times that of the co-polarized singlet.

## 4.5. Discussion

The carrier localization induced by the magnetic field leads to stronger, more local interactions, leading to much stronger absorption by excitons and trions alike. Increased oscillator strengths are reflective of tighter binding and reduced itinerant electron screening overall.

Out of the various peaks identified in the preceding data, all appear in polarization pairs except for the trion triplet. This is not surprising in the context of the selection rules shown in Fig. 4.2, where the lowest-energy triplet trion state (in which both electrons align with the field) is only optically accessible through one polarization. We expect the next spin configuration to be quite weakly bound, and have not observed it.

### 4.5.1. Oscillator strength

In the presence of doping, the strongest absorption lines are consistently those which couple states containing field-aligned electrons. In the case of the singlet trion, the $\sigma+$ variant has twice the oscillator strength of its counter-polarized counterpart. This is expected since spin-up resident carriers form the ground state of this transition, and these are more plentiful when the Zeeman splitting is on the order of $k_B T$. A simple estimation of the thermal spin polarization is shown in Fig. 4.8.

The ratio of oscillator strengths of the neutral exciton is also 2, favoring the $\sigma+$ transition, for a different reason. Here, the photoexcited electron is aligned counter to the field. While in an undoped semiconductor we expect both spin states to be equally dense, in our case the spin-up electron state has higher occupation, rendering this state less available when generating excitons. This Pauli blocking effect is not evident in the absence of the doping laser: in that case, the ratio between oscillator strengths of the exciton is very close to 1.

Both excitons and singlet trions have weaker oscillator strength than the triplet trion, which is surprising because the triplet trion is a less tightly bound state. Like the singlet trion, it has the (highly-available) spin-up state of the resident carrier as its ground state, and excites a spin-up electron

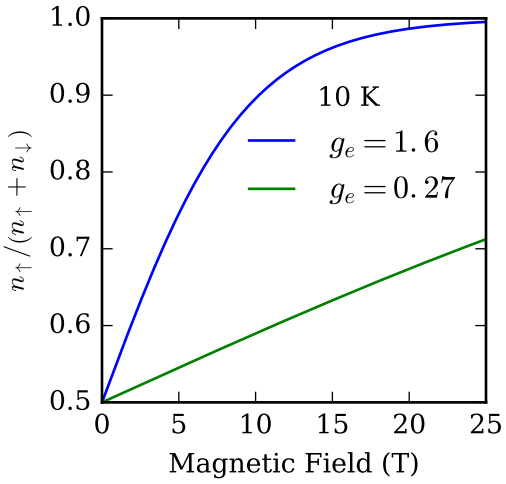


FIGURE 4.8. Estimation of thermal spin polarization of electrons at 10 K. Shown as a function of magnetic field, for two values of the electron $g$-factor. In the GaAs sample of this experiment, $g_e \approx 0.27$; the CdTe value $g_e \approx 1.6$ is shown for a basis of comparison. Computed from Boltzmann statistics with $n_\uparrow/(n_\uparrow + n_\downarrow) = 1/(1 + \exp(-\Delta E/(k_B T)))$.

(as does the Pauli-blocked neutral exciton transition in $\sigma-$). Evidently, the orbital state associated with the trion triplet is denser than that of the singlet or neutral exciton in the presence of Landau levels, evidenced by our direct measurement of the oscillator strengths.

### 4.5.2. Absence of the dark triplet

A transition to a regime in which a triplet forms the ground state of the trion is not observed in these data, which is not surprising for a number of reasons. The observed trion triplet line, which does not cross the singlet line, is almost certainly the 'bright' triplet, whose orbital angular momentum state allows it to appear in absorption spectroscopy. The 'dark' triplet, which has the same spin configuration but a different orbital angular momentum, is almost always more strongly bound. Whether or not a more strongly bound triplet state exists in this sample cannot be said definitively without a set of photoluminescence data, which was not obtained in our experiment.

Previous observations of a triplet becoming the trion ground state involved either much higher field strengths [29] or materials having higher $g$-factors [30]. In that work, the triplet-ground state crossing was "hidden" in the sense that the relevant spectral lines did not actually cross due to complications from a field-dependent $g$-factor, an effect which is also present in our data.

### 4.5.3. Field-dependent $g$-factor and hole mixing

While at small fields the exciton and trion lines barely split, in keeping with the small value of the $g$-factor that is expected for GaAs, they exhibit a $g$-factor of approximately 2 at high fields. Since the inflection point coincides with the field strength at which the heavy- and light-hole excitons cross, it is plausible that valence-band mixing is leading to this behavior. Light hole excitons are known to exhibit giant Zeeman splitting [84]. However, this is unlikely to be hiding a transition to a trion-triplet ground state, as in Ref. [30], since the sign of the $g$-factor does not change.

Fig. 4.7 reveals one other property of interest with regard to the binding energy of the singlet trions. The trion energy depends weakly on the Landau level filling factor, reaching local maxima and minima [29]. An oscillation in the singlet trion binding energy is clear in the data, and may be a means of verifying the injected carrier density.

## 4.6. Conclusion

We have presented a direct measurement of the density of states for excitons and trions in a high magnetic field. We have identified the emergence of the triplet line, and determined that it displays unexpectedly high oscillator strength. Zeeman splitting of the other species has been unambiguously measured, revealing a nonlinear splitting that is indicative of a hole-mixing process.

# CHAPTER V

# EXCITON-CORRELATED TUNNELING

In the preceding chapter, mixed-type quantum wells (MTQW) were utilized to study excitonic physics under a range of doping conditions. In particular, this enabled optical injection of a two-dimensional electron gas (2DEG) to the well of interest. Since the presence of a 2DEG is necessary for trion formation, but screens the exciton interaction, this is a straightforward way to distinguish between excitonic species in absorption spectra, especially at high magnetic fields where many resonances are present.

However, MTQW play host to a multitude of other interaction phenomena arising from its dual-well structure. In particular, carrier tunneling between the narrow well (NW) and wide well (WW) has been shown to be linked to the WW exciton population [46]. In this chapter we examine this exciton-correlated tunneling effect, and explore its behavior at high magnetic fields.

This chapter contains material previously published with co-authors Stephen A. McGill and Hailin Wang [3].

## 5.1. Reverse Bleaching in Optically Doped Samples

In contrast to atomic spectra, excitonic resonances are subject to bleaching: a reduction in the oscillator strength of the resonance as it is driven harder. This is due to collisional decoherence of the dipole transition as the pumping laser introduces large populations of excitons to the sample.

This is not to be confused with screening, a process by which a 2DEG weakens the exciton binding by creating a mean field of negative charges. Screening manifests itself as a broadening and weakening of the exciton line. In certain MTQW samples, pumping on this weakened line results in a nearly perfect recovery of its oscillator strength, rather than further broadening. This is counter to the intuition that this should result in bleaching, as it would for the undoped line. While bleaching does eventually occur, at low pump intensities it is overwhelmed by a competing process that reverses the screening effects.

An example of this is shown in Fig. 5.1. Two resonances correspond to the heavy-hole (HH) and light-hole (LH) excitons. Optical doping is effected by a HeNe laser having intensity $0.15$ mW/cm$^2$, estimated to inject less than $10^9$ electrons/cm$^2$. This dilute 2DEG screens the excitonic interaction,

leading to weaker and broader exciton absorption lines. No shift in the absorption lines is observed that would imply a buildup of charges outside the well structure.

This effect is reversed, however, by applying a 2 mW/cm² CW pump beam to the LH exciton resonance, estimated to inject on the order of $10^9$ excitons/cm². LH excitons injected by this pump quickly decay to HH excitons. In this case, the absorption is only partially recovered, but stronger excitonic pumps have been shown to almost prefectly recover the HH resonance, even for much denser 2DEGs [46].

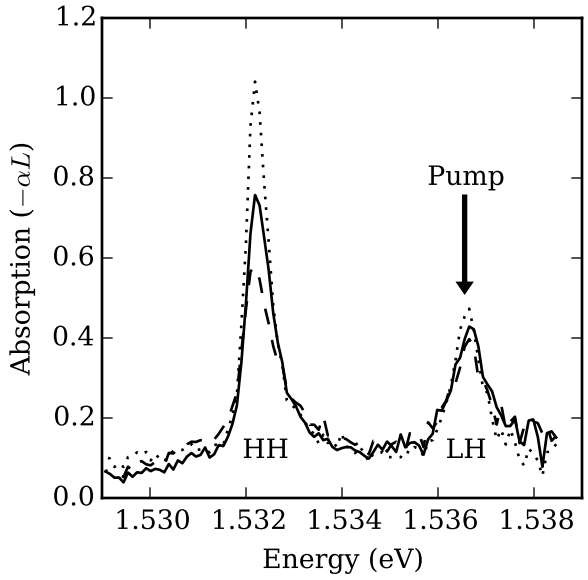


FIGURE 5.1. Reverse bleaching of exciton absorption spectra in optically-doped GaAs MTQW. At 12 K, HH and LH exciton absorption resonances are visible in the presence (dashed line) and absence (dotted line) of a HeNe laser having intensity 0.15 mW/cm². A strengthened HH exciton line (solid line) is seen by applying a cw pump beam to the LH resonance, having power 2 mW/cm².

The origins of this screening-reversal process lie in a peculiar correlated-tunneling process first reported by Carey Phelps [46, 85]. The optically-injected 2DEG in a MTQW has a finite lifetime, set by the rate at which holes tunnel through the interwell barrier. Presence of excitons accelerates the hole tunneling, thereby reducing the 2DEG lifetime. In the case of the experiment shown above, a shortened lifetime results in a lower steady-state 2DEG density, and therefore reduced screening. This *exciton-correlated tunneling* effect is a surprising result, since tunneling is generally viewed as a

single-particle transport process [86–88]. To understand exciton-correlated tunneling it is necessary to consider the WW and NW together, which form a bilayer system.

## 5.2. Correlated Tunneling in Bilayers

A bilayer is any system in which electrons and holes are separated by a thin barrier. These systems are of interest as a platform for studying the collective behavior of excitons since the physical separation of carriers leads to longer exciton lifetimes [39, 42]. Cross-layer Coulomb potentials can be manipulated to create artificial lattices [89], while interlayer correlations between carriers can lead to other subtle behaviors, as shown by recent studies on the Kondo effect [90] and biexciton formation [41].

Studies of other bilayer systems have revealed that the tunneling of the electrons or holes across the barrier can depend on the interlayer Coulomb correlation between the carriers. As beautifully demonstrated in an earlier experimental study on bilayers formed in modulation-doped GaAs quantum wells in the quantum Hall regime, a giant increase in the tunneling rate occurs when every electron is positioned opposite a hole across the barrier [44]. This giant increase in the tunneling rate was also taken as evidence for the Bose-Einstein condensation of the electron-hole pairs in the bilayer system [45].

Observation of correlated-tunneling processes in MTQW is surprising because the barrier thickness is much greater than it is in other bilayer systems. In the remainder of this chapter, we present detailed experimental studies on the dependence of the hole tunneling rates on temperature, carrier density, exciton density, and external magnetic fields. These studies form a systematic survey of the interwell tunneling behaviors in MTQW, helping to elucidate more information about the microscopic origins of exciton-correlated tunneling.

## 5.3. Optical Measurement of Interwell Tunneling

Hole tunneling rates in MTQW can be measured entirely with optical techniques. As described in section 2.5.1, MTQW samples are optically doped with a 2DEG by applying pump laser that excites carriers in the narrow well (NW). A measure of this lifetime can be obtained by switching off the NW pump, and then performing time-resolved absorption spectroscopy at the exciton line. Because the

exciton absorption is screened proportionally to the 2DEG density, the strength of transmission will decay exponentially as the 2DEG decays.

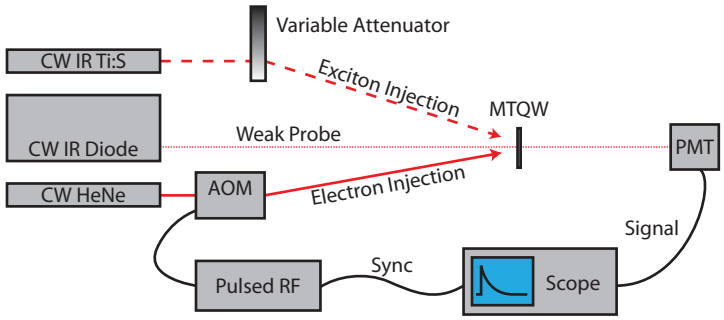


FIGURE 5.2. Experimental configuration for tunneling measurements. A continuous-wave infrared (CW IR) diode laser serves as a probe to monitor sample transmission at the HH exciton resonance, while a HeNe laser, gated by an acousto-optic modulator (AOM), periodically injects electrons to the WW from the NW. For studies involving exciton injection, a third beam (a CW Ti:Sapphire laser) was added at the LH exciton resonance. PMT: photomultiplier tube.

In Fig. 5.2 a schematic view of the experimental apparatus for such a measurement is shown. HeNe laser pulses are generated by gating a continuous-wave (CW) HeNe laser with an acousto-optic modulator. We probe the rate of hole tunneling using a weak CW probe beam tuned to the HH exciton resonance. The time-resolved transmission of this beam is measured by a fast detector (photomultiplier tube) and fast oscilloscope. The third beam, labeled "exciton injection" in the diagram, is relevant for the studies described in the next section, and is not active for the results described presently. Unless otherwise specified, all experiments were performed with the sample held at 10 K in a helium flow cryostat. Magnetic field dependence was studied using the 25 T Split Florida-Helix resistive magnet at the National High Magnetic Field Laboratory in Tallahassee, Florida.

## 5.4. Hole Tunneling Characteristics

Results of a typical tunneling measurement are shown in Fig. 5.3. This plots the time-resolved recovery of the same HH exciton absorption resonance shown being screened in Fig. 5.1. This recovery reflects the decay of excess electron population in the WW, which results from interlayer tunneling of the holes followed by radiative recombination. The decay of the electron population is double exponential in nature, characterized by a fast component with a decay time of several milliseconds and a slow component with a decay time of tens of milliseconds. Since the electron-hole or exciton recombination time (on the order of nanoseconds) is orders of magnitude faster than the

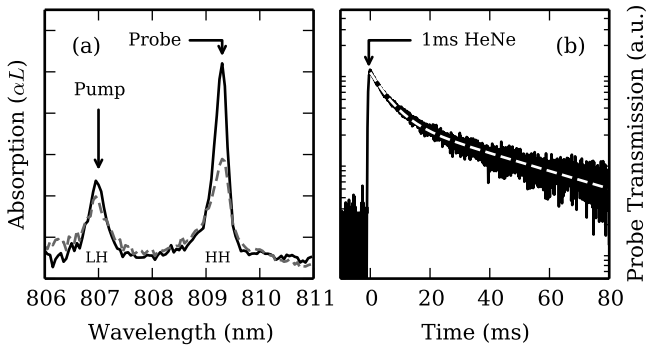


FIGURE 5.3. Results of a typical optical tunneling measurement. (a) Absorption spectrum shows wide-well heavy-hole (HH) and light-hole (LH) exciton resonances (solid lines) at 10 K. A continuous-wave HeNe laser of intensity 0.1 mW/cm² injects an electron gas, which bleaches the exciton resonances (dashed lines). (b) Time-resolved optical transmission at the HH exciton line in response to 1 ms pulsed HeNe excitation of 5 mW/cm². Decay is well-described by a double-exponential function (dashed line).

hole tunneling time, the decay of the electron population measures directly the interlayer tunneling rate of the holes.

Recall from Section 2.5.1 that the hole tunneling process must satisfy energy and momentum conservation. Unless assisted by a phonon, it only occurs where valence subbands of the two wells cross in Fig. 2.8. Well width fluctuations in a QW lead to an inhomogeneous broadening of the QW energy levels. A width fluctuation of one monolayer induces a much greater energy variation in the NW than that in the WW [91]. We estimate that NW bands are inhomogenously broadened by up to 10 meV, as illustrated by the gray band in Fig. 2.8. Holes in the NW are expected to be thermally distributed in the HH1 band within this spectral range, overlapping to varying degrees with the HH5 band of the WW. Note that these holes are spatially localized by the fluctuations in the confinement potential [91].

The double-exponential character of the tunneling curve in Fig. 5.3b can be attributed to this inhomogeneous distribution of the holes in the NW. Specifically, we associate the slow decay component with the holes at the bottom of the thermal distribution. Absorption of phonons with a relatively large energy to compensate the energy between the relevant HH5 and HH1 bands are needed in order for the tunneling process to take place. Conversely, the fast component is associated with holes that are near the higher energy region of the inhomogeneous distribution, which nearly overlaps with the HH5 band in the WW. This interpretation is supported by our earlier experimental

study, which shows that at relatively low temperatures ($T < 30$ K), the fast tunneling rate depends more sensitively on the temperature than does the slow tunneling rate [46].

In the following experiments, two decay rates are extracted from these tunneling curves by way of a least-squares fitting.

### 5.4.1. Electron density

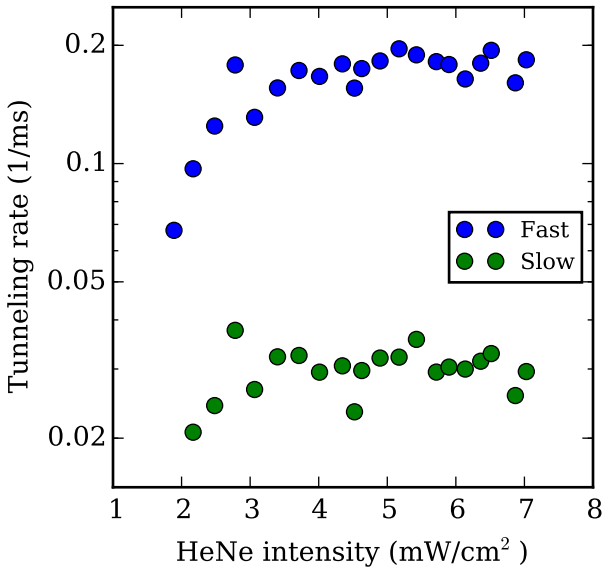


FIGURE 5.4. Extracted hole tunneling rates as a function of electron density, as controlled by the peak intensity of a 1 ms HeNe laser pulse.

Figure 5.4 shows the dependence of the fast and slow hole tunneling rates on the excess electron density in the WW, controlled here by the intensity of the HeNe laser. A HeNe pulse, with a duration of 1 ms and with a peak intensity of 4 mW/cm², is estimated to inject on the order of a few times $10^9$ electrons/cm² to the WW [46, 59]. As shown in Fig. 5.4, the tunneling rates are largely insensitive to the electron density when the HeNe laser intensity exceeds 3 mW/cm². This indicates that, within this range, buildup of space-charge fields associated with the injected electron population does not affect the measurement. For the rest of the tunneling experiments presented in this chapter, the experiments were performed at sufficiently high electron densities such that the tunneling rates are nearly independent of the electron density.

The flat dependence of the hole tunneling rate on the HeNe laser intensity shown in Fig. 5.4 indicates that shifts in the subband alignment due to electric fields associated with the electron-hole separation are small. The falloff at low intensity can be understood in a similar way to the temperature dependence, since the lower-energy states in the HH1 are expected to fill prior to the higher-energy states associated with the fast tunneling rate. At these low densities the tunneling curve would be better described by a single exponential at the slow rate.

### 5.4.2. Magnetic field

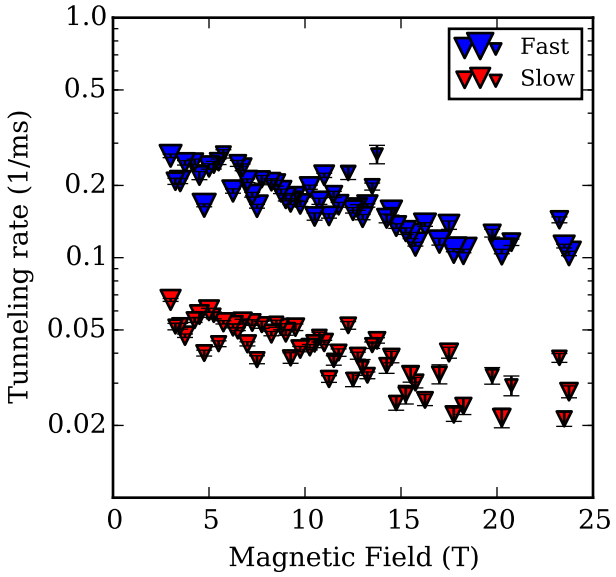


FIGURE 5.5. Dependence of the hole tunneling rates on magnetic field. A 1 ms HeNe laser pulse with a peak intensity of 4 mW/cm² was used.

Fig. 5.5 shows the dependence of the hole tunneling rate on the magnitude of a magnetic field applied perpendicular to the QW (Faraday geometry). The tunneling rates decrease monotonically with the increasing magnetic field.

In the presence of a magnetic field perpendicular to the QW plane, both the electron and hole energy levels in the QW are quantized into discrete Landau levels. However, even at the highest magnetic field used, the quantization energy ($\sim$ 2 meV at 20 T for electrons, estimated from $E = \hbar eB/m_e$) is still small compared with the large inhomogeneous broadening of the NW hole

bands. As shown in Fig. 5.5, the magnetic field leads to a gradual decrease in the tunneling rate with increasing magnetic field, a result consistent with prior studies on interwell tunneling [43]. Although the magnetic field leads to no qualitative changes in the overall behavior of the hole tunneling, it does lead to major changes in how the exciton injection in the WW affects the hole tunneling rate, as will be discussed in detail later.

## 5.5. Exciton-Correlated Tunneling

Having established the double-exponential structure of tunneling, and completed a thorough study of how the two rates vary with respect to temperature and WW electron density, we now turn our attention to its dependence on the exciton density. The correlation between WW excitons and the interwell hole tunneling rate is known to give rise to the surprising reverse-bleaching behavior described at the beginning to this chapter, but the particular interactions underlying this unexpected correlation are not well understood. In this section, we present evidence that exciton-correlated tunneling is a result of a local interaction between excitons and holes via Coulomb forces extending across the barrier. Specifically, we posit that a NW hole is much more likely to tunnel when positioned directly opposite a WW exciton, in analogy to the quantum Hall results mentioned earlier [44, 45].

For these experiments, a third "exciton injection" beam is added to the apparatus shown in Fig. 5.2. To avoid optical interference with the probing beam, this is tuned to the light hole (LH) exciton resonance rather than the HH exciton. The LH excitons injected by this beam relax to HH excitons on a timescale of a few ps.

### 5.5.1. Exciton density and temperature

The inset of Figure 5.6 shows an example of time-resolved transmission at the HH resonance with and without the pump beam at 10 K. As shown in the figure, the exciton injection enhances the tunneling of the holes. The pump intensity used in the experiment is 0.2 W/cm$^2$, corresponding to an estimated exciton density on the order of $10^8$/cm$^2$.

At these low densities, heating induced by the injected excitons should be negligible. However, to confirm that the enhanced tunneling arising from exciton injection is not due to heating, we measured the dependence of the hole tunneling rate on the pump intensity obtained at temperatures

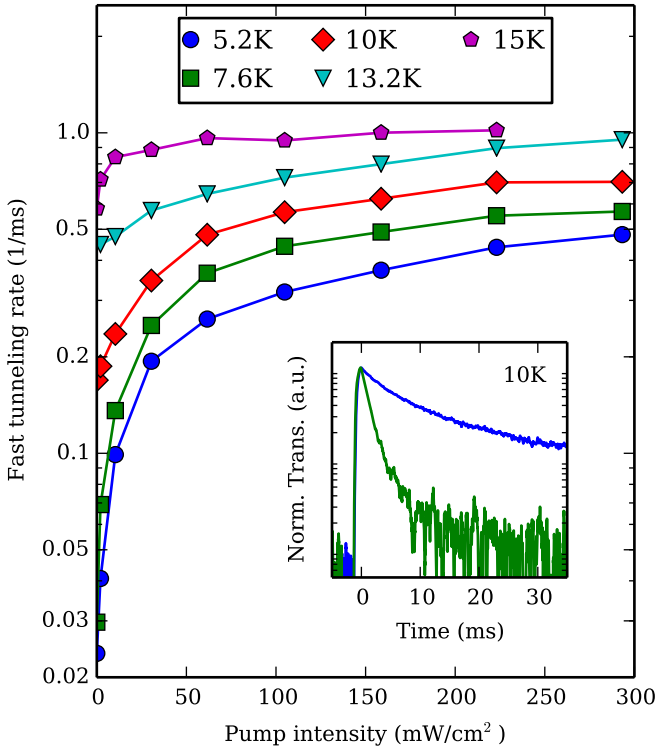


FIGURE 5.6. Fast component of hole tunneling rate vs. pump intensity and temperature. Shown on a logarithmic scale, as a function of pump intensity, for several temperature conditions. At high exciton densities, the hole tunneling rate is accelerated. This effect is more pronounced at lower temperatures. Inset: Time-resolved transmission at the heavy-hole exciton resonance of the WW in the presence of a HeNe laser pulse 1 ms in duration and 5 mW/cm² in peak intensity. Hole tunneling is accelerated in the presence of a CW pump beam with an intensity of 0.2 W/cm² at the LH exciton (green line) relative to without exciton pumping (blue line). Vertical scale is logarithmic.

ranging from 5 to 15 K. These results are shown in Figure 5.6. At lower temperatures, the tunneling rate is slower and more sensitive to the enhancement induced by the exciton correlation. At 5 K, the rate can be made twelve times faster by applying a pump 100 mW/cm² in intensity, whereas at 15 K the rate may only be made twice as fast. Note that the enhancement in the tunneling rate levels off when the pump beam reaches a modest intensity of 0.1 W/cm².

These results support the interpretation that heating is not the mechanism by which excitons accelerate tunneling, since most of the increase in the tunneling is observed at the lowest exciton densities. Furthermore, the enhancement levels off at relatively high exciton densities, and the maximally-accelerated tunneling rate is a function of the temperature. Note that the results of Fig. 5.6 show that while the hole tunneling rate is faster with increasing temperature, the degree of enhancement by the exciton correlations (indicated by the vertical range spanned by the traces) is reduced with increasing temperature, a finding consistent with the temperature dependence of analogous correlation effects described in the quantum Hall experiments [45].

### 5.5.2. Magnetic field

To get a better understanding of the exciton-correlation induced hole tunneling, we have also carried out experimental studies in the presence of a high magnetic field (5 to 20 T) perpendicular to the QW plane (see Fig. 5.7). Under these magnetic fields, the hole tunneling rate becomes nearly independent of the injection of excitons in the WW. The strong magnetic field effectively quenches the enhanced hole tunneling induced by the exciton injection in the WW.

This quenching provides additional physical insights into the interlayer Coulomb correlation, especially on the important role of exciton mobility. If the correlation is indeed due to a local exciton-hole interaction rather than some nonlocal process (e.g., an overall bending of the dispersion relations leading to changes in the subband overlaps) then it will be limited by the ability of both particles to diffuse and find one another.

Excitons in quantum wells have a large spatial extent, which has the effect of averaging out imperfections in the quantum well that are smaller than its wavefunction. As a result, zero-field excitons can see a smooth quantum well even when it contains imperfections on the length scale of a few tens of angstroms. Recall from section 2.7 that at high magnetic field the spatial extent of the magnetoexciton is set by the magnetic length $l_0 = \sqrt{\hbar/eB}$. Relative to the zero-field 2D exciton,

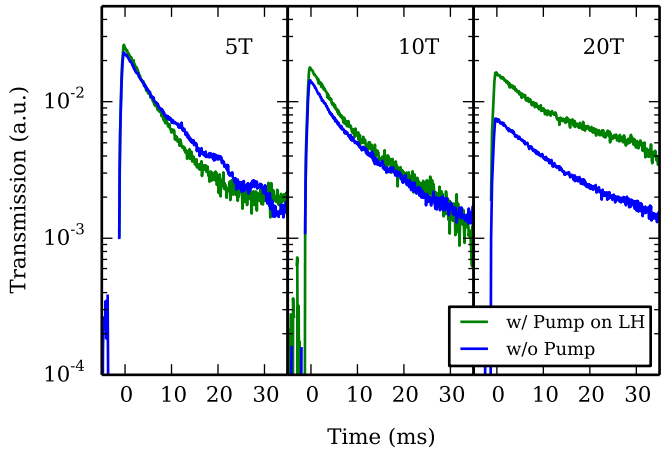


FIGURE 5.7. Quench of exciton-correlated tunneling. Time-resolved transmission at the heavy-hole exciton resonance of the WW at 10 K, in response to a 1 ms HeNe pulse with a peak intensity of 4 mW/cm². Experiment performed at 10 K in the presence (green lines) and absence (blue lines) of an 100 mW/cm² exciton injection beam tuned to the LH exciton resonance, in various perpendicular magnetic fields. The tunneling rate enhancement evident in Fig.5.6a is not observed at these magnetic fields.

this decreases the effective area over which well-width fluctuations are averaged, and the exciton is more liable to be stuck in a potential minimum. This can result in greatly reduced exciton mobility, as shown by an earlier experimental study on the diffusion coefficient of excitons in the presence of a magnetic field [92].

At the relatively high magnetic field used in Fig. 5.7, the excitons are effectively localized such that within the short ns lifetime, they cannot migrate to regions that are opposite to or near holes in the NW. In this regard, the magnetic freeze-out of the excitons effectively quenches the interlayer Coulomb correlation between the holes in the NW and the excitons in the WW.

## 5.6. Discussion

The evidence presented in the preceding section points toward a local exciton-hole correlation as the origin of exciton-correlated tunneling. Since the holes are spatially localized by the fluctuations in the width of the NW, they induce a weak coulomb potential on the other side of the barrier which is felt by the WW excitons. The depth of this potential, while not sufficient to bind the exciton, is enough to increase its probability density opposite the position of the localized hole. When opposite the hole, the exciton modifies the tunnelling parameters in a way that enhances the rate at which it occurs. This interaction is shown schematically by the dark correlation arrow in Fig. 5.8.

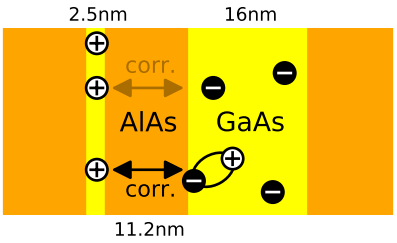


FIGURE 5.8. Schematic view of interlayer Coulomb correlation of WW excitons with NW holes. These correlations can lead to accelerated hole tunneling.

Were this interaction strong enough to result in a bound state, it would be called a positively charged indirect exciton – that is, a trion having one of its constituents localized in a separate well. This is in analogy to the "indirect excitons" present in symmetric coupled quantum well bilayers with a thin barrier [39, 40]. This would be the trion species that is opposite the ones observed in Chapter IV (having two holes as opposed to two electrons), but its binding energy would likely be comparable.

It's important to emphasize that we have not observed, or even looked for, positively charged trions in this sample. Furthermore, a bound indirect trion can be ruled out simply on account of the large 11.2nm barrier. However, the Coulomb correlations leading to the correlated tunneling process can be considered to be a scattering state of the indirect trion. In that respect, exciton-correlated hole tunneling is another example of a trion-mediated optical process in semiconductors.

With the evidence of interlayer exciton-hole correlation, a question naturally arises why there is no evidence of interlayer correlations between electrons and holes in the MTQW. This "missing" correlation is shown by the weak correlation arrow in Fig. 5.8. Using the method in Ref. [93], we estimate the binding energy for indirect excitons in our sample to be $\sim$ 1 meV or smaller, and we have not observed them in experiments.

Still, intuition would dictate that the attraction felt by the exciton would be even less than that felt by a negative point charge, since it carries no net charge. This is somewhat misleading, since excitons regularly have Bohr radii on the order of 100 Å, the same length scale as the barrier thickness, so they present a large dipole [50]. Furthermore, the interface roughness inherent in a QW leads to relatively small exciton mobility or ambipolar diffusion coefficient [94–96]. In essence, excitons are much heavier than the electrons and thus are much less mobile amid the interface potential

fluctuations. Hence, exciton-hole correlations are more evident than electron-hole correlations by virtue of their longer interaction time.

## 5.7. Summary

We have presented a study of a surprising exciton-hole Coulomb correlation which manifests in dramatic optical nonlinearity. Superficially, the reversal of bleaching resulting from this process in steady state has potential application as a "reset latch" on the low-power optical nonlinearity for which the MTQW was designed. However, a full understanding of exciton-correlated hole tunneling reveals a much deeper potential: this interaction provides a mechanism for using optical excitations to manipulate tunneling processes, thus enabling optical control of carrier transport.

The basis of this correlated tunneling in a local interaction between excitons and holes serves as another example of the trion interaction providing a platform for a nonlinear optical process. While in this case the three constituent quasiparticles are not strictly bound, the scattering state of their interaction plays a crucial role in accelerating the hole tunneling.

MTQW were designed to exhibit low-power optical nonlinearities, the full richness of which were not fully anticipated. In this dissertation they have served as an instructive new platform for studying manybody physics. The processes described in this chapter have been discovered, not engineered, but nevertheless lead to dramatic effects. Understanding the manybody processes at work in semiconductor structures is key to unlocking their full potential.

# CHAPTER VI

# CONCLUSION

In this dissertation, we have presented experimental studies on the physics of excitons and trions in semiconductor quantum wells. These bodies have profound influence on the optical behavior of semiconductors, and also provide a platform for studying the physics of interactions across a broad range of conditions. The experiments conducted as part of this work both reveal details about trion structure, and demonstrate their utility in optical and transport applications.

In Chapter III, we demonstrated the ability of the trion to act as an optical excited state for electron spins, the coherence properties of which are highly desirable. While electromagnetically induced transparency has been demonstrated in this system previously, this study focused on optimizing the degree of transparency achieved in an optically dense spin ensemble, which is important for many applications. This was pursued by exploring high magnetic field regimes in a CdTe sample with which large Zeeman splittings could be achieved. Under the condition of a high Voigt field, we have revealed that the trion state becomes unbound.

This finding stands in contrast to the stronger trion binding typically observed in high Faraday fields, the configuration which is typically studied in the literature. In Chapter IV we explored this subject by conducting a measurement of direct absorption by trions in a GaAs mixed-type quantum well. The results are reflective of well-known excitonic properties at high magnetic fields: the formation of magnetoexcitons, the diamagnetic shift, and the binding of a triplet trion state. In contrast to many previous studies based on photoluminescence, our measurement reveals the oscillator strengths of these states directly. This makes other effects clear: The reduction of the exciton wavefunction by the field, as reflected in its stronger absorption profile, as well as a weak Pauli blocking effect. Of particular interest in our results is the strong absorption by the triplet trion state, which suggests a large electron-hole overlap in the spatial wavefunction. This datum is of value since the actual three-body wavefunction is notoriously difficult to calculate.

Finally, we have extensively characterized the exciton-correlated tunneling effect in mixed-type quantum wells. The data presented in Chapter V represent the most comprehensive assessment to date of this phenomenon under varying conditions of temperature, electron density, exciton density, and magnetic field. From these we conclude that the exciton-correlated tunneling is a result of a local,

cross-barrier interaction between exciton and hole. In that sense, this interaction can be considered the scattering state of an indirect trion, and one more example of a trion-mediated optical process: in this case, one which gives optical control of an electron transport process.

Taken together, these three studies form a broad survey of several trion-based optical processes in quantum wells, and contribute new knowledge in our understanding of each.

### 6.1. Future Work

In terms of furthering our understanding of the processes at work in these systems, the conclusions heretofore stated represent only incremental advances. In striving for answers, the process of science inevitably stumbles on ever more challenging questions, whether or not the original line of inquiry is ever satisfied. In this respect, the experiments in this dissertation have left no lack of considerations unexamined. We close by naming a few of the most obvious ones.

The unbinding of the trion reported in Chapter III merits a more detailed examination. While the physics of trions in magnetic fields has been extensively examined in the Faraday geometry, we know of few studies which apply a high magnetic field in the Voigt direction, and none which would have indicated that the trion would break down. Whether this happens due to disruption of the trion's orbital structure, or perhaps due to the effects of valence band mixing, remains an open question. Experimental study would require a full set of experimental data from the same sample, in both Faraday and Voigt geometries.

The experimental work of Chapter IV would be enhanced by a rigorous theoretical or numerical examination of the three-body wavefunctions under those conditions. The arguments put forth in interpreting those data are based upon an understanding of the relatively simple two-body wavefunction, considering the trionic effects only by analogy. The relevance of these data to confirming existing three-body models of trions merits a fuller theoretical collaboration.

It is understood that the significance of the exciton-correlated tunneling effect (Chapter V) is a sample-dependent property. That is, minute variations in the valence-subband alignment between the two wells can have profound effects. This can be surveyed experimentally by applying an electric potential across the sample, so that the subband alignments are tuned through one another. This was not prioritized in this study due to the challenges inherent in fabricating the necessary electrodes, but

would be a worthwhile investigation. In addition, some experiments not presented here indicate that crystal strain plays a significant role as well, but this has not been investigated in any controlled way.

It is hoped that the findings of this dissertation lead to further investigation and deeper understanding, whether along the directions named here or not.

APPENDIX A

SPECTROSCOPY OF QUANTUM SYSTEMS

### A.0.1. The electromagnetic field

We treat light as classical electromagnetic waves, where the electric-field oscillation at a certain point in space is given by

$$\vec{\mathcal{E}}(t) = \hat{\varepsilon} E_0 \cos(\omega t - \phi) \tag{A.1}$$

where $\hat{\varepsilon}$ is the polarization unit vector and $\omega$ is the angular frequency of the wave. $E_0$ is the amplitude of the electric field oscillation, which we'll treat as a constant for now. We decompose this real wave into counter-rotating complex waves:

$$\vec{\mathcal{E}}(t) = \underset{\circlearrowleft}{\frac{\hat{\varepsilon} E_0}{2} \exp(-i\omega t)} + \underset{\circlearrowright}{\frac{\hat{\varepsilon} E_0^*}{2} \exp(+i\omega t)} \tag{A.2}$$

so that the first term rotates with frequency $+\omega$ in the complex plane, and the second rotates with frequency $-\omega$. We've absorbed the phase offset $\phi$ into the electric field amplitude $E_0$, which is now a complex number.

Note that each of these terms contains complete information about the field. The expression for the real electric field can be obtained by adding either one to its complex conjugate.

### A.0.2. The quantum system

Consider a basic two-level quantum system – for example, an atom with only two levels. An electron bound to this atom may occupy two states: a ground state $|g\rangle$ at $E = 0$ and an excited state $|e\rangle$ at $E = \hbar\omega_0$. The free-evolution Hamiltonian is given by

$$H_0 = \hbar\omega_0 |e\rangle\langle e|. \tag{A.3}$$

This atom presents a coulombic dipole which couples to the EM field, leading to an interaction potential

$$V = -\vec{d} \cdot \vec{\mathcal{E}}. \tag{A.4}$$

Using symmetry arguments [97, p. 5.1.1], this dipole vector $\vec{d} = -e\vec{r_e}$ may be written in terms of the atomic raising and lowering operators:

$$\vec{d} = \langle g|\vec{d}|e\rangle(\sigma + \sigma^\dagger) \tag{A.5}$$

where $\sigma = |g\rangle\langle e|$ is the lowering operator, and $\sigma^\dagger$ is its hermitian conjugate, the raising operator.

These two components of the dipole operator rotate in opposite directions, just like the components of the EM field above. To see this, we evolve them according to the Heisenberg equation

$$\dot{A} = \frac{-i}{\hbar}[A, H]. \tag{A.6}$$

Using $H = H_0$, we see that

$$\dot{\sigma} = -i\omega_0\sigma \qquad\qquad \dot{\sigma}^\dagger = +i\omega_0\sigma^\dagger \tag{A.7}$$

which implies that the raising and lowering operators counter-rotate at $\omega_0$:

$$\sigma \sim \exp(\underset{\circlearrowleft}{-i\omega_0 t}) \qquad\qquad \sigma^\dagger \sim \exp(\underset{\circlearrowright}{+i\omega_0 t}). \tag{A.8}$$

This is counterintuitive to think about since the definition of $\sigma$ contains no explicit time dependence, as was the case for the fields, so it's not immediately clear in what sense $\sigma$ is rotating at $\omega_0$. The rotation frequency $\omega_0$ is not so much a property of $\sigma$ as it is a tendency – it arises out of its evolution under $H_0$. Since $\sigma$ is an operator, what's really rotating is its expectation value ( and the specifics will depend on the state, the Hamiltonian, etc.). Informed by the understanding that the general behavior of $\sigma$ and $\sigma^\dagger$ is to counter-rotate, we can justify splitting the dipole operator as we did the field:

$$\vec{d} = \vec{d}_{ge}(\underset{\circlearrowleft}{\sigma} + \underset{\circlearrowright}{\sigma^\dagger}). \tag{A.9}$$

### A.0.3. A dipole interaction in the rotating-wave approximation

Suppose the atom is subject to a near-resonant field, $\omega \approx \omega_0$. Writing out the interaction term,

$$V = -\vec{d} \cdot \vec{E} \tag{A.10}$$

$$= -\frac{\vec{d_{ge}} \cdot \hat{\varepsilon}}{2}(\underset{\circlearrowleft}{\sigma} + \underset{\circlearrowleft}{\sigma^\dagger}) \times (E_0 \underset{\circlearrowleft}{\exp}(-i\omega t) + E_0^* \underset{\circlearrowleft}{\exp}(+i\omega t)). \tag{A.11}$$

We can multiply this out into four terms. The first and last of these will rotate at $\pm(\omega + \omega_0)$, far beyond the optical range. In the rotating wave approximation (RWA), we ignore these terms, focusing our attention on terms which describe the slow dynamics.

$$V = -\frac{\vec{d_{ge}} \cdot \hat{\varepsilon}}{2}(\sigma E_0 \exp(+i\omega t) + \sigma^\dagger E_0^* \exp(-i\omega t)) \tag{A.12}$$

To make things cleaner, we wrap up the polarization, dipole strength, and field amplitude in the "Rabi frequency"

$$\Omega := -\vec{d_{ge}} \cdot \hat{\varepsilon}\frac{E_0}{\hbar} \tag{A.13}$$

so that the interaction term reads

$$V = \frac{\hbar}{2}(\sigma\Omega \exp(+i\omega t) + \sigma^\dagger \Omega^* \exp(-i\omega t)). \tag{A.14}$$

### A.0.4. The rotating frame

To make things convenient, we boost this Hamiltonian into a rotating frame. This is basically a change of basis defined by the unitary operator

$$U = \exp(i\omega t|e\rangle\langle e|). \tag{A.15}$$

Which maps basis states $|\alpha\rangle$ to new states $|\tilde{\alpha}\rangle = U|e\rangle$, and time-invariant matrices $M$ to $\tilde{M} = UMU^\dagger$. It can be shown (cite this) that Hamiltonians must transform according to

$$\tilde{H} = UHU^\dagger + i\hbar(\dot{U})U^\dagger. \tag{A.16}$$

Piece by piece, we find

$$i\hbar(\dot{U})U^\dagger = -\hbar\omega|e\rangle\langle e| \tag{A.17}$$

$$UH_0U^\dagger = H_0 \tag{A.18}$$

$$UVU^\dagger = \frac{\hbar}{2}(\Omega\sigma + \Omega^*\sigma^\dagger). \tag{A.19}$$

So the full, transformed Hamiltonian is

$$\tilde{H} = -\hbar\Delta|e\rangle\langle e| + \frac{\hbar}{2}(\Omega\sigma + \Omega^*\sigma^\dagger) \tag{A.20}$$

where we have defined the field detuning $\Delta := (\omega - \omega_0)$. The first term represents free evolution in the ground state, and the second represents coupling to the EM field. This is useful because it removes all explicit time dependence.

### A.0.5. Equations of motion, decoherence

We can get the equations of motion for a pure state $|\tilde{\psi}\rangle$ via the Schrödinger equation or, more generally, using the Heisenberg equation for a density operator $\tilde{\rho}$

$$\dot{\tilde{\rho}} = \frac{-i}{\hbar}[\tilde{H}, \tilde{\rho}]. \tag{A.21}$$

The elements of $\tilde{\rho}$ represent populations ($\tilde{\rho}_{ee}, \tilde{\rho}_{gg}$) in the two states, and coherences ($\tilde{\rho}_{eg}, \tilde{\rho}_{ge}$) between them. The twiddles remind us that we're working in the rotating frame.

Taking matrix elements of the Heisenberg equation (lots of algebra), we find the *optical Bloch equations*

$$\dot{\tilde{\rho}}_{ee} = \frac{i}{2}(\Omega\tilde{\rho}_{eg} - \Omega^*\tilde{\rho}_{ge}) \qquad -\Gamma\tilde{\rho}_{ee} \tag{A.22}$$

$$\dot{\tilde{\rho}}_{gg} = -\frac{i}{2}(\Omega\tilde{\rho}_{eg} - \Omega^*\tilde{\rho}_{ge}) \qquad +\Gamma\tilde{\rho}_{ee} \tag{A.23}$$

$$\dot{\tilde{\rho}}_{eg} = i\Delta\tilde{\rho}_{eg} - i\frac{\Omega^*}{2}(\tilde{\rho}_{gg} - \tilde{\rho}_{ee}) \qquad -\gamma\tilde{\rho}_{eg} \tag{A.24}$$

$$\dot{\tilde{\rho}}_{ge} = -i\Delta\tilde{\rho}_{ge} + i\frac{\Omega}{2}(\tilde{\rho}_{gg} - \tilde{\rho}_{ee}) \qquad -\gamma\tilde{\rho}_{ge}. \tag{A.25}$$

Actually, the Hamiltonian evolution only yields the terms on the left. We insert the terms on the right "by hand" to represent effects of spontaneous emission and decoherence. This kind of evolution is non-unitary – it would turn pure states into mixed states, so it can't be described by a self-adjoint Hamiltonian.

The $\Gamma$ terms remove population from the excited state and place it back in the ground state at rate $\Gamma$ (the spontaneous emission rate). The other two terms represent decay in the coherence. The dephasing rate $\gamma$ is bounded from below by $\Gamma/2$, So we can introduce $\gamma_c$ to represent "pure" dephasing, such that

$$\gamma = \frac{\Gamma}{2} + \gamma_c. \tag{A.26}$$

### A.0.6. Aside: The Lindblad operator

In the operator representation, inserting these terms is equivalent to modifying the Heisenberg equation to read

$$\dot{\tilde{\rho}} = \frac{-i}{\hbar}[\tilde{H}, \tilde{\rho}] + \Gamma\mathcal{D}[\sigma]\tilde{\rho} + \gamma_c\mathcal{D}[\sigma_z]\tilde{\rho} \tag{A.27}$$

such that two extra terms handle the non-unitary decay in $\tilde{\rho}$. The first handles spontaneous emission, and the second handles any extra dephasing (beyond that caused by spontaneous emission). Here, $\sigma_z = |e\rangle\langle e| - |g\rangle\langle g|$ and $\mathcal{D}$ is the *Lindblad superoperator*

$$\mathcal{D}[c]\tilde{\rho} = c\tilde{\rho}c^\dagger - \frac{1}{2}(c^\dagger c\tilde{\rho} + \tilde{\rho}c^\dagger c). \tag{A.28}$$

This operator is "super" in the sense that it transcends the noncommutative rules of operator algebra by acting on both sides of its target $\tilde{\rho}$.

### A.0.7. Steady state

Now that we've included damping rates on the atomic oscillator, we can find the steady-state behavior of the system. This amounts to solving the optical Bloch equations (A.22)–(A.25) for the equilibrium condition $\dot{\tilde{\rho}} = 0$.

By setting $\dot{\tilde{\rho}}_{eg} = 0$, we find

$$\tilde{\rho}_{eg} = \frac{\Omega^* \left(\frac{1}{2} - \tilde{\rho}_{ee}\right)}{\Delta + i\gamma} \tag{A.29}$$

where we have used $\tilde{\rho}_{gg} = 1 - \tilde{\rho}_{ee}$. Likewise, the complex conjugate of this equation,

$$\tilde{\rho}_{ge} = \frac{\Omega\left(\frac{1}{2} - \tilde{\rho}_{ee}\right)}{\Delta - i\gamma}, \tag{A.30}$$

follows from setting $\dot{\tilde{\rho}}_{ge} = 0$. The quantity

$$\Omega\tilde{\rho}_{eg} - \Omega^*\tilde{\rho}_{ge} = -\frac{2i\gamma|\Omega|^2\left(\frac{1}{2} - \tilde{\rho}_{ee}\right)}{\Delta^2 + \gamma^2} \tag{A.31}$$

will be useful in computing the steady-state excited population $\tilde{\rho}_{ee}$:

$$\dot{\tilde{\rho}}_{ee} = 0 = \frac{i}{2}(\Omega\tilde{\rho}_{eg} - \Omega^*\tilde{\rho}_{ge}) - \Gamma\tilde{\rho}_{ee} \tag{A.32}$$

$$= -\frac{i}{2}\left(\frac{2i\gamma|\Omega|^2\left(\frac{1}{2} - \tilde{\rho}_{ee}\right)}{\Delta^2 + \gamma^2}\right) - \Gamma\tilde{\rho}_{ee} \tag{A.33}$$

$$\implies \tilde{\rho}_{ee} = \frac{\frac{1}{2}\gamma|\Omega|^2}{\gamma|\Omega|^2 + \Gamma(\Delta^2 + \gamma^2)}. \tag{A.34}$$

This can, in turn, be plugged back into the expression for the steady-state coherence (A.29):

$$\tilde{\rho}_{eg} = \frac{\Omega^*/2}{\Delta + i\gamma}\left(1 - \frac{\gamma|\Omega|^2}{\gamma|\Omega|^2 + \Gamma(\Delta^2 + \gamma^2)}\right) \tag{A.35}$$

$$= \frac{\Omega^*/2}{\Delta + i\gamma}\left(\frac{\Gamma(\Delta^2 + \gamma^2)}{\gamma|\Omega|^2 + \Gamma(\Delta^2 + \gamma^2)}\right). \tag{A.36}$$

The other two matrix elements, of course, follow from $\tilde{\rho}_{gg} = 1 - \tilde{\rho}_{ee}$ and $\tilde{\rho}_{ge} = \tilde{\rho}^*_{eg}$.

Diagonal elements of the density matrix correspond to the fractional occupation of each level. In Fig. A.1 the excited state population, $\tilde{\rho}_{ee}$, is plotted as a function of the scaled detuning $\Delta/\Gamma$. This is maximal when driven on resonance ($\Delta = 0$), and the sharpness of this resonance is set by $\gamma_c$. By increasing $\Omega$, the excited state population is seen to saturate at a value of $1/2$, at which point the resonance exhibits power broadening behavior. This indicates that a population inversion is not achievable by pumping a single dipole transition.

Off-diagonal elements represent the *coherences* between the two levels: the extent to which the system behaves as a pure (as opposed to mixed) state. This term is less intuitive to think about, but it contains important information with regard to the optical behavior of the medium.

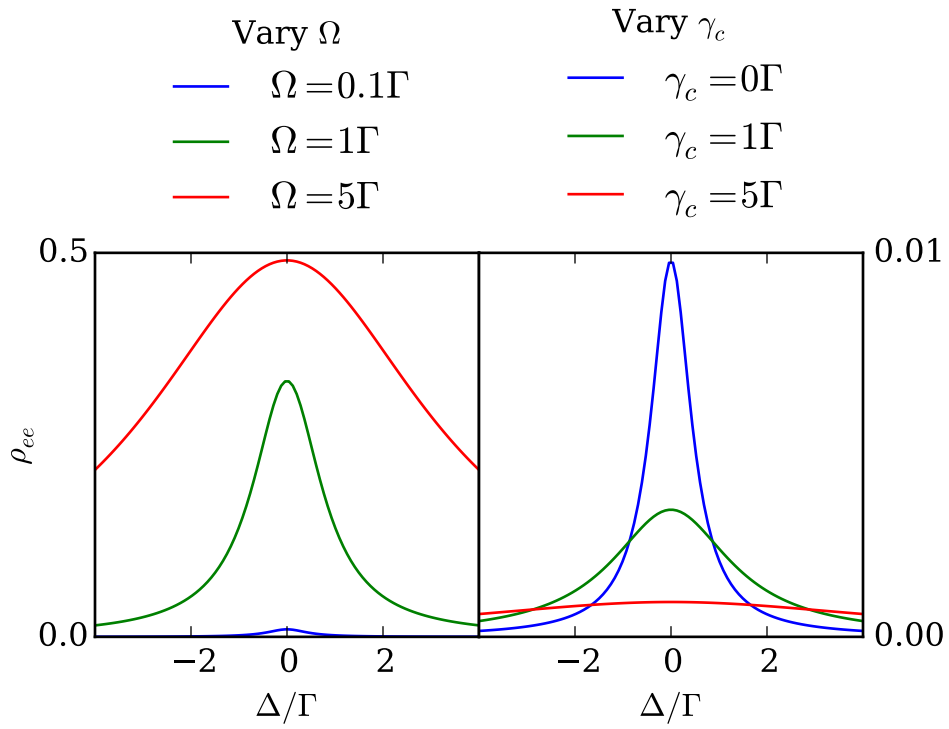


FIGURE A.1. Simulated excited-state population of a two-level medium in steady state. Steady-state population term, $\tilde{\rho}_{ee}$, as a function of the scaled detuning $\Delta/\Gamma$. In the left column, various values of the Rabi frequency $\Omega$ are shown. On the right, various values of the dephasing rate $\omega_c$ are shown.

### A.0.8. Optical properties of the two-level medium

In experiments, we don't always observe populations and coherences directly. We learn about these quantities by measuring properties of the transmitted laser. To complete our analysis, we need to understand how the matrix elements of $\tilde{\rho}$ are linked to the optical properties of the medium.

In solids and gases, the medium for electromagnetic waves is the electric displacement

$$\mathcal{D} = \epsilon_0 \mathcal{E} + \mathcal{P}, \tag{A.37}$$

where $\epsilon_0$ is the vacuum permittivity [98, Appendix A]. The second term, the polarization $\mathcal{P}$, accounts for the presence of dipoles in the medium, which can also carry waves.

The polarization is the dipole moment per unit volume:

$$\mathcal{P} = N\langle \vec{d} \rangle \tag{A.38}$$

where N is the number density of atoms, and the $\langle\ \rangle$ represents an expectation value. In quantum mechanics, expectation values are obtained from the density operator by

$$\langle A \rangle = \mathrm{Tr}[A\rho] \tag{A.39}$$

where $\mathrm{Tr}[\ ]$ represents the trace operation (summing the diagonal elements of a matrix). Note that the twiddle is gone from the density operator – we're back to working in the lab frame, where our measurements are made. Recalling that $\vec{d} = \vec{d}_{ge}(\sigma + \sigma^\dagger)$,

$$\begin{aligned} \langle \vec{d} \rangle &= \mathrm{Tr}[\vec{d}\rho] && \text{(A.40)} \\ &= \langle g|\vec{d}_{ge}(\sigma + \sigma^\dagger)\rho|g\rangle + \langle e|\vec{d}_{ge}(\sigma + \sigma^\dagger)\rho|e\rangle && \text{(A.41)} \\ &= \vec{d}_{ge}\langle e|\rho|g\rangle + \vec{d}_{ge}\langle g|\rho|e\rangle. && \text{(A.42)} \end{aligned}$$

In the last step, $(\sigma + \sigma^\dagger)$ acted left on the bras. In the first term, the $\langle g|$ bra picked out the lowering operator $\sigma$ , while the $\langle e|$ bra picked out the raising operator $\sigma^\dagger$ in the second term.

Note that the only dipoles in our medium of two-level systems are those induced by the interaction potential. $\mathcal{P}$ exists only as a response to $\mathcal{E}$. When this is the case, and that response is

parallel to the field polarization and linear in the electric field amplitude, it's common to express the polarization in terms of the linear susceptibility $\chi$:

$$\mathcal{P} = \epsilon_0 \chi \mathcal{E}. \tag{A.43}$$

Our expression for $\mathcal{E}$ was given in (A.2), so this relation tells us

$$N\left(\vec{d}_{ge}\langle e|\rho|g\rangle + \vec{d}_{ge}\langle g|\rho|e\rangle\right) = \epsilon_0 \chi \left(\frac{\hat{\varepsilon}E_0}{2}\exp(-i\omega t) + \frac{\hat{\varepsilon}E_0^*}{2}\exp(+i\omega t)\right). \tag{A.44}$$

Note that both bracketed quantities are real – so $\chi$, as defined in (A.43), is real too.

It'd be nice to write the matrix elements $\langle\alpha|\rho|\beta\rangle$ in terms of the rotating-frame matrix elements we computed for the steady state in the last section. We do that by inserting the identity $U^\dagger U$:

$$\langle\alpha|\rho|\beta\rangle = \langle\alpha|U^\dagger \underbrace{U\rho U^\dagger}_{\tilde{\rho}} U|\beta\rangle \tag{A.45}$$

where $U$ is the transformation matrix (A.15). We find

$$\langle e|\rho|g\rangle = \tilde{\rho}_{eg}\exp(-i\omega t) \qquad\qquad \langle g|\rho|e\rangle = \tilde{\rho}_{ge}\exp(+i\omega t) \tag{A.46}$$

and write (A.44) as

$$N\left(\vec{d}_{ge}\tilde{\rho}_{eg}\underset{\circlearrowleft}{\exp}(-i\omega t) + \vec{d}_{ge}\tilde{\rho}_{ge}\underset{\circlearrowright}{\exp}(+i\omega t)\right) = \epsilon_0\chi\left(\frac{\hat{\varepsilon}E_0}{2}\underset{\circlearrowleft}{\exp}(-i\omega t) + \frac{\hat{\varepsilon}E_0^*}{2}\underset{\circlearrowright}{\exp}(+i\omega t)\right). \tag{A.47}$$

Rather than solving this, we can equate the coefficients of the counter-rotating terms:

$$N\vec{d}_{ge}\tilde{\rho}_{eg} = \epsilon_0\chi\frac{\hat{\varepsilon}E_0}{2}. \tag{A.48}$$

It's worth stopping to reexamine our assumptions here. We're equating two complex quantities, $\tilde{\rho}_{eg}$ and $E_0$, by a real proportionality factor $\chi$. We're free to make $E_0$ real, by choosing the origin of $t$ such that $\phi = 0$ in (A.1) (and many treatments do this). However, it's clear from inspecting (A.36) that $\tilde{\rho}_{eg}$ can ***still*** be complex under those conditions, in which case (A.48) cannot hold unless we let $\chi$ be complex.

This means that our linearity assumption (A.43) is, essentially, bad – but only in one respect. That definition was for the case where the material polarization is parallel to the field, linear in the field, and *in phase* with the field – given that it states a direct proportionality between $\mathcal{P}$ and $\mathcal{E}$.

Our material of two-level systems responds to the field like a set of driven oscillators – so their oscillation may lag behind that of the electric field. To allow for this possibility, we let $\chi$ be defined by

$$\mathcal{P}^+ = \epsilon_0 \chi \mathcal{E}^+. \tag{A.49}$$

where $(+)$ denotes the positive-rotating part – for example, $\mathcal{E}^+$ would denote the first term in (A.2), while $\mathcal{E}^-$ would denote the second. We can split up $\mathcal{P}$ in a similar manner.

Here $\chi$ can be complex, and when it is, it denotes a material whose oscillatory response is shifted somewhat in phase.

As noted in A.0.1, it's sufficient to work with just the $(+)$ terms, since they contain complete information about the field. They don't describe the physically-observable field until they're added to their complex conjugate, but in the meantime they're mathematically much easier to deal with. Describing phase-laggy materials would have been trigonometrically nasty using the expressions for the real field, but with complex exponentials it's as easy as letting $\chi$ carry a phase.

We can write the now-complex susceptibility $\chi$ is given in terms of the steady-state coherence as

$$\chi = \frac{2N}{\epsilon_0}(\vec{d}_{ge} \cdot \hat{\varepsilon}) \frac{\tilde{\rho}_{eg}}{E_0} \tag{A.50}$$

$$= \frac{-2N}{\hbar \epsilon_0} |\vec{d}_{ge} \cdot \hat{\varepsilon}|^2 \frac{\tilde{\rho}_{eg}}{\Omega} \tag{A.51}$$

where in the second step we used the definition of the Rabi frequency (A.13).

### A.0.9. Complex refractive index

In view of (A.43), (A.37) becomes

$$\mathcal{D} = \epsilon_0 \underbrace{(1+\chi)}_{=:n^2} \mathcal{E} \tag{A.52}$$

where $n$ is the refractive index – the ratio by which waves are slowed in the medium relative to the vacuum.

For example, a plane wave propogating along $z$

$$\vec{\mathcal{E}}(t) = \frac{\hat{\varepsilon}E_0}{2}\exp(ikz - i\omega t) + \text{c.c.} \tag{A.53}$$

has $k = \omega/c$ modified to $k_n = n\omega/c$ when it enters the medium:

$$\vec{\mathcal{E}}(t) = \frac{\hat{\varepsilon}E_0}{2}\exp(inkz - i\omega t) + \text{c.c.} \tag{A.54}$$

If $n$ is complex, as we've shown it must be for our system the imaginary part leads to an exponentially decaying amplitude along the propogation direction at rate $\text{Im}[n]k$:

$$\vec{\mathcal{E}}(t) = \frac{\hat{\varepsilon}E_0}{2}\exp(-\text{Im}[n]kz)\exp(i\text{Re}[n]kz - i\omega t) + \text{c.c.} \tag{A.55}$$

Hence, the intensity will decay at rate

$$\alpha = 2\text{Im}[n]\omega/c \tag{A.56}$$

where $\alpha$ is the coefficient in Beer's Law

$$I(z) = I_0\exp(-\alpha z) \tag{A.57}$$

since $k = \omega/c$, and the intensity is the square of the amplitude.

The susceptibility $\chi$ is related to the refractive index $n$ by

$$n = \sqrt{1+\chi} \overset{\chi \ll 1}{\approx} 1 + \frac{\chi}{2}. \tag{A.58}$$

So, at least for small $\chi$, the absorption coefficient is given by

$$\alpha = \text{Im}[\chi]\omega/c. \tag{A.59}$$

For the two-level system, we can use (A.51) to find

$$\alpha = \frac{-2N\omega}{\hbar\epsilon_0 c}|\vec{d}_{ge}\cdot\hat{\varepsilon}|^2\mathrm{Im}\left[\frac{\tilde{\rho}_{eg}}{\Omega}\right] \tag{A.60}$$

while the real refractive index is given by

$$n = \frac{-N}{\hbar\epsilon_0}|\vec{d}_{ge}\cdot\hat{\varepsilon}|^2\mathrm{Re}\left[\frac{\tilde{\rho}_{eg}}{\Omega}\right]. \tag{A.61}$$

These expressions characterize the absorption and refraction behavior of the two-level dipole transition.

### A.0.10. Lineshape of dipole transitions

Hence, we can get two measurable optical properties – the refractive index and the absorption coefficient – from the real and imaginary parts of the scaled coherence $\tilde{\rho}_{eg}/\Omega$, respectively. The prefactors in eqs. (A.60) and (A.61) set the units and overall scale of these measurable quantities, but their dependence on physical parameters ($\Delta$, $\Omega$, $\gamma$, $\Gamma$) is all wrapped up in the coherence term $\tilde{\rho}_{eg}/\Omega$. This is not strictly true in the case of $\alpha$, which has the laser frequency $\omega = \omega_0 + \Delta$, but for small detunings it is good enough.

Recall the steady-state form of the coherence for a two-level atom (A.36). Choosing $\Omega$ to be real, we can write

$$\frac{\tilde{\rho}_{eg}}{\Omega} = \frac{\frac{\Gamma}{2}(\Delta - i\gamma)}{\gamma|\Omega|^2 + \Gamma(\Delta^2+\gamma^2)} \tag{A.62}$$

from which follow equations describing the refractive index

$$n \propto \mathrm{Re}\left[\frac{\tilde{\rho}_{eg}}{\Omega}\right] = \frac{\Delta/2}{\frac{\gamma}{\Gamma}|\Omega|^2 + \Delta^2 + \gamma^2} \tag{A.63}$$

and absorption coefficient

$$\alpha \propto \mathrm{Im}\left[-\frac{\tilde{\rho}_{eg}}{\Omega}\right] = \frac{\gamma/2}{\frac{\gamma}{\Gamma}|\Omega|^2 + \Delta^2 + \gamma^2} \tag{A.64}$$

of the two-level medium. Recall that $\gamma = \gamma_c + \Gamma/2$. When $\gamma_c = 0$ and in the limit of a weak driving field ($\Omega \to 0$), (A.64) yields a Lorentzian profile in $\Delta$, having full-width at half maximum $\Gamma$.

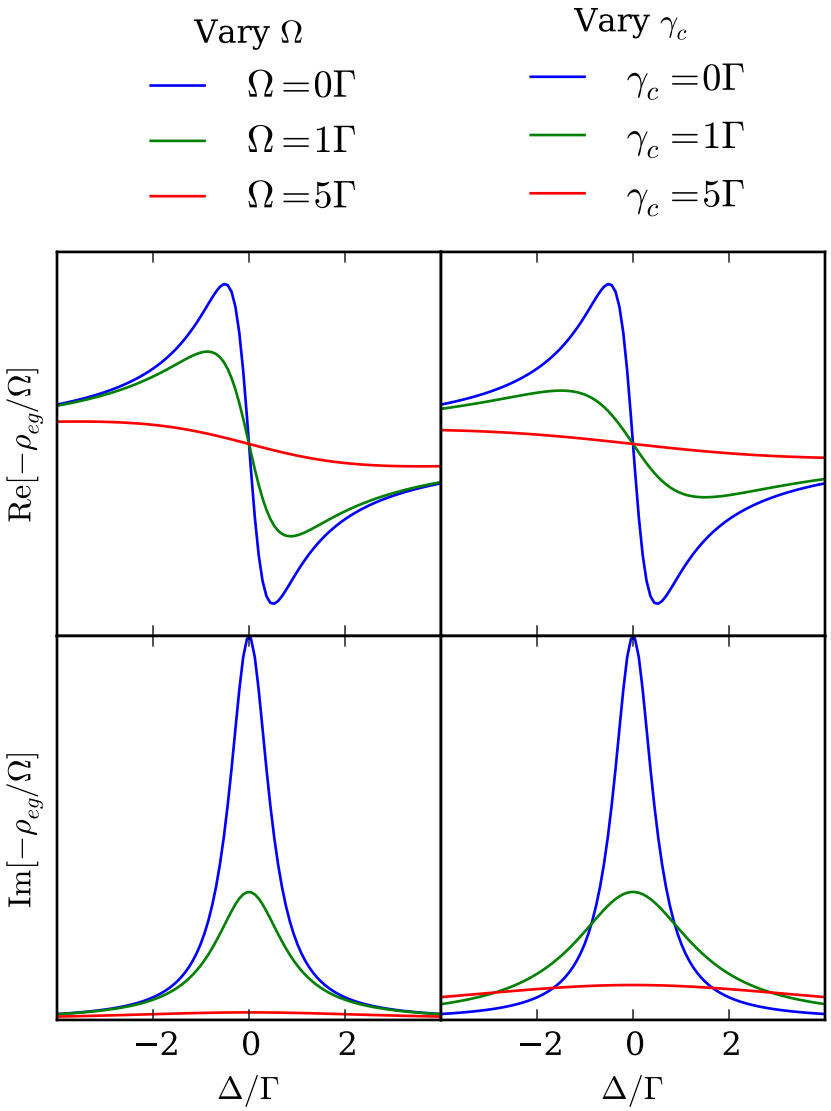


FIGURE A.2. Simulated refractive index and absorption coefficient of a two-level medium. Real and imaginary parts of the scaled steady-state coherence term, $\tilde{\rho}_{eg}/\Omega$, as a function of the scaled detuning $\Delta/\Gamma$. In the left column, various values of the Rabi frequency $\Omega$ are shown. On the right, various values of the dephasing rate $\omega_c$ are shown.

In Fig. A.2 both terms are plotted as a function of the scaled detuning $\Delta/\Gamma$. These are illustrative of the refractive index (top row) and absorption coefficient (bottom row) of the two-level medium near resonance. By increasing the amplitude, $\Omega$, of the incident light, we see that less of it is absorbed or refracted (saturation behavior). Adding an extra dephasing rate $\gamma_c$ results in less pronounced attenuation of the absorption spectrum, but much more noticeable broadening.

### A.0.11. Summary

In this section we reviewed the foundations of semiclassical quantum optics, to establish the link between measurements of optical absorption and off-diagonal entries in the density matrix of the underlying quantum system. In particular, we showed that a two-level system has an absorption lineshape with a Lorentzian profile, and displays straightforward saturation and broadening behaviors.

APPENDIX B

# CIRCUMVENTING DECOHERENCE USING DRESSED STATES

In ensembles of quantum systems, or any time-averaged observation of a single quantum system, inhomogeneity of the environment can contribute to broadening of the transitions of interest. In the case of NV centers, a fluctuating charge environment leads to spectral diffusion of the $E_x$ and $E_y$ lines, and randomly configured $C^{13}$ nuclear spins lead to a varying Zeeman splitting in the ground-state triplet. In either case, the observed lineshape is a convolution of a Lorentzian (having a width corresponding to the coherence between the two states) with the distribution of transition energies resulting from the inhomogeneity.

Many techniques, such as spectral hole burning, exist for extracting the homogeneous linewidth from the inhomogeneously broadened line, and thereby measuring the coherence. However, if we're interested in utilizing this coherence for some application (such as a quantum bit or nanoscale sensor), we need to perform some state engineering and actually reduce the effect of the inhomogeneous broadening.

In essence, this amounts to choosing the basis states for our application so that their energies do not shift in response to the perturbations of the environment – or at the very least, that they shift together. In this way, the transitions between them are less sensitive to the background, and the observed lineshape approaches that of the homogeneous transition.

### B.0.1. In a two level system

A two-level optical system provides a simple, if imperfect, example. A rotating-frame Hamiltonian for this system is given by

$$H^{(ge)} = \begin{bmatrix} 0 & \frac{\Omega}{2} \\ \frac{\Omega}{2} & \Delta \end{bmatrix} \tag{B.1}$$

where $\Omega$ is the Rabi frequency and $\Delta$ is the detuning of an optical field coupling the two states. For simplicity, $\hbar = 1$. In this representation, a state is described by a 2-element vector containing amplitudes for the ground ($g$) and excited ($e$) states, respectively.

This Hamiltonian is diagonalized by applying the rotation

$$R(\theta) = \begin{bmatrix} \cos\theta & -\sin\theta \\ \sin\theta & \cos\theta \end{bmatrix} \tag{B.2}$$

to the bare-state basis representation of $H$, which results in

$$R(\theta)H^{(ge)}R(-\theta) = \frac{1}{2}\begin{bmatrix} (\Delta\sin 2\theta - \Omega\cos 2\theta - \Omega)\tan\theta & \Omega\cos 2\theta - \Delta\sin 2\theta \\ \Omega\cos 2\theta - \Delta\sin 2\theta & \Delta\cos 2\theta + \Delta + \Omega\sin 2\theta \end{bmatrix}. \tag{B.3}$$

By inspecting the off-diagonal elements, we see that the transformed Hamiltonian is diagonal when

$$\Omega\cos 2\theta = \Delta\sin 2\theta \tag{B.4}$$

In the resonant ($\Delta = 0$) case, this is satisfied for $\theta = \pi/4$; otherwise $\theta$ can be chosen to satisfy $\frac{\Omega}{\Delta} = \tan 2\theta$ (Stückelberg relation). In either case, the diagonalized Hamiltonian can be written

$$H^{(lu)} = \begin{bmatrix} \frac{\Delta}{2} - \frac{1}{2}\sqrt{\Delta^2+\Omega^2} & 0 \\ 0 & \frac{\Delta}{2} + \frac{1}{2}\sqrt{\Delta^2+\Omega^2} \end{bmatrix}. \tag{B.5}$$

The lower ($l$) and upper ($u$) energy eigenstates now form the basis in place of the bare ground/excited states. This is the ***dressed-state basis*** – the eigenbasis of the system when being modified, or ***dressed***, by the optical field $\Omega$. Under this condition, the energy of the transition depends on the strength of the driving field:

$$\Delta E(\Delta, \Omega) = \sqrt{\Delta^2 + \Omega^2}. \tag{B.6}$$

In physical systems where the excited-state energy is subject to spectral diffusion, such as the $E_y$ or $E_x$ level in an NV center, $\Delta$ becomes a fluctuating parameter. We can represent this using

$$\Delta = \Delta_0 + \delta \tag{B.7}$$

where $\Delta_0$ is the average detuning and $\delta$ is a zero-mean random variable. For the undressed states, where the transition energy $\Delta E(\Delta, 0) = \Delta$, the variations of $\delta$ map directly onto variations in the

transition energy $\Delta E$ with scaling factor 1. In other words, the energetic width of the inhomogeneous distribution is exactly the width of the distribution of the random variable $\delta$.

For the dressed states, this scaling factor is reduced, leading to a narrower inhomogeneous distribution. Linearizing our expression for the transition energy about $\Delta = \Delta_0$,

$$\Delta E(\Delta_0, \Omega, \delta) = \sqrt{\Delta_0^2 + \Omega^2} + \frac{\Delta_0}{\sqrt{\Delta_0^2 + \Omega^2}}\delta + \mathcal{O}(\delta^2). \tag{B.8}$$

Here, the scaling factor in the linear term

$$\frac{\Delta_0}{\sqrt{\Delta_0^2 + \Omega^2}} \tag{B.9}$$

is less than unity for $\Omega > 0$. As a result, the energetic width of the inhomogeneously broadened line is reduced by this factor up to the point that it is limited by the homogeneous linewidth.

### B.0.2. Three-level state dressing

In a three-level system, such as the ground-state triplet of the NV center, an even better suppression of the broadening is possible. If the two excited states are each coupled to a shared ground state by two independent optical fields having equal Rabi frequencies and detunings, the bare-state Hamiltonian takes the form

$$H^{(g+-)} = \begin{bmatrix} 0 & \frac{\Omega}{2} & \frac{\Omega}{2} \\ \frac{\Omega}{2} & \Delta & 0 \\ \frac{\Omega}{2} & 0 & \Delta \end{bmatrix}. \tag{B.10}$$

In this system, the asymmetric linear combination of the two excited states famously forms a "dark state" which is decoupled from the field. The transformation from the bare-state basis to the bright/dark basis is given by the unitary transformation matrix

$$U = \begin{bmatrix} 1 & 0 & 0 \\ 0 & \frac{1}{\sqrt{2}} & \frac{1}{\sqrt{2}} \\ 0 & -\frac{1}{\sqrt{2}} & \frac{1}{\sqrt{2}} \end{bmatrix}. \tag{B.11}$$

Incidentally, this is the rotation matrix $R(\theta)$ applied between the two excited states with $\theta = -\pi/2$, mixing them into symmetric and antisymmetric linear combinations. The transformed Hamiltonian

reads

$$H^{(gbd)} = UH^{(g+-)}U^\dagger = \begin{bmatrix} 0 & \frac{\Omega}{\sqrt{2}} & 0 \\ \frac{\Omega}{\sqrt{2}} & \Delta & 0 \\ 0 & 0 & \Delta \end{bmatrix}. \tag{B.12}$$

Here the ground, bright, and dark states are represented by the first, second and third columns. In this block-diagonal form, the upper block forms a two-level system that has no couplings into the dark state at all.

Within this two-level subsystem, we can proceed identically to the case of a two-level subsystem discussed in the previous section, making the replacement $\Omega \to \sqrt{2}\Omega$. The dressing field mixes the ground and bright states to form upper/lower eigenstates separated by

$$\Delta E(\Delta, \Omega) = \sqrt{\Delta^2 + 2\Omega^2}. \tag{B.13}$$

For symmetric fluctuations in the twin detunings $\Delta$, all the same principles apply: by dressing the states with a field of sufficient Rabi frequency $\Omega$, the inhomogeneous distribution's mapping onto the energy scale can be compressed by the factor

$$\frac{\Delta_0}{\sqrt{\Delta_0^2 + 2\Omega^2}} \tag{B.14}$$

Except for the helpful factor of 2, this is no more effective in the 3-level system as it was in the 2-level system.

### B.0.3. Antisymmetric fluctuations in three-level systems

Symmetric fluctuations are not necessarily the most relevant fluctuations, however. In cases where the two legs of the three-level system have opposite spin, a fluctuating magnetic field will induce antisymmetric shifts. This is the case in the ground-state triplet of the NV center, where stray fields from lattice $C^{13}$ nuclei contribute to fluctuations in the Zeeman splitting. Fortunately, dressed states are even more robust against these kinds of shifts.

We can represent these shifts with the perturbing Hamiltonian

$$H_p^{(g+-)} = \begin{bmatrix} 0 & 0 & 0 \\ 0 & \delta & 0 \\ 0 & 0 & -\delta \end{bmatrix} \tag{B.15}$$

in the original, bare-state basis, where $\delta$ is a zero-mean random variable shifting the excited states apart. In the bright-dark basis, there is no shift at all:

$$H^{(gbd)} = U H_p^{(g+-)} U^\dagger = \begin{bmatrix} 0 & 0 & 0 \\ 0 & 0 & -\delta \\ 0 & -\delta & 0 \end{bmatrix}. \tag{B.16}$$

Instead, $\delta$ manifests as a coupling between the bright and dark states. In the dressed state basis, the perturbing Hamiltonian takes the form

$$H_p^{(lud)} = \delta \begin{bmatrix} 0 & 0 & \sin\theta \\ 0 & 0 & -\cos\theta \\ \sin\theta & -\cos\theta & 0 \end{bmatrix}. \tag{B.17}$$

where $\theta$ is defined by the modified Stückelberg relation

$$\sqrt{2}\frac{\Omega}{\Delta} = \tan 2\theta \tag{B.18}$$

and the remixed ground/bright states have been relabeled lower/upper. Since there are no diagonal elements in the perturbing Hamiltonian, so the first-order corrections to the dressed-state energies $E_n^{(1)} = \langle n| H_p |n\rangle$ vanish. Corrections enter first at second order, where

$$E_n^{(2)} = \sum_{m \neq n} \frac{|\langle m| H_p |n\rangle|^2}{E_n - E_m}. \tag{B.19}$$

## REFERENCES CITED


[1] D. A. Golter, T. K. Baldwin, and H. Wang, "Protecting a solid-state spin from decoherence using dressed spin states", Physical Review Letters **113**, 237601 (2014).

[2] T. K. Baldwin, C. Phelps, H. Wang, and J. P. Prineas, "Persistence of trions and quenching of excitons in optically induced two-dimensional electron gases in mixed-type GaAs/AlAs quantum wells", Journal of the Optical Society of America B **31**, 3138 (2014).

[3] T. K. Baldwin, S. A. McGill, and H. Wang, "Exciton-correlated hole tunneling in mixed-type GaAs quantum wells", Physical Review B **90**, 035304 (2014).

[4] D. Golter, T. K. Baldwin, and H. Wang, "Suppression of Spin Dephasing in Diamond NV Centers with Microwave-Dressed Spin States", in Conference on Lasers and Electro-Optics 2014 (2014), FW1B.3.

[5] T. K. Baldwin, S. McGill, and H. Wang, "Manybody-Correlated Tunneling in Mixed-Type Quantum Wells at High Magnetic Field", in Conference on Lasers and Electro-Optics 2013 (2013), QM2D.2.

[6] T. K. Baldwin, S. O'Leary, and H. Wang, "Electromagnetically Induced Transparency of Spin Ensembles in a Two-Dimensional Electron Gas", in Conference on Lasers and Electro-Optics 2012 (2012), QM3G.5.

[7] T. M. Sweeney, T. Baldwin, and H. Wang, "Probing Heavy-Hole and Light-Hole Excitonic Beats in a GaAs Quantum well with Phase-Locked Raman Pulse Pairs", in Conference on Lasers and Electro-Optics 2010 (2010), QFI4.

[8] A. Imtiaz, T. Baldwin, H. T. Nembach, T. M. Wallis, and P. Kabos, "Near-field microwave microscope measurements to characterize bulk material properties", Applied Physics Letters **90**, 243105 (2007).

[9] D. S. Chemla and J. Shah, "Many-body and correlation effects in semiconductors", Nature **411**, 549–557 (2001).

[10] I. Bar-Joseph, "Trions in GaAs quantum wells", Semiconductor Science and Technology **20**, R29–R39 (2005).

[11] M. A. Lampert, "Mobile and immobile effective-mass-particle complexes in nonmetallic solids", Physical Review Letters **1**, 450–453 (1958).

[12] K. Kheng, R. T. Cox, M. Y. d' Aubigné, F. Bassani, K. Saminadayar, and S. Tatarenko, "Observation of negatively charged excitons $X^-$ in semiconductor quantum wells", Physical Review Letters **71**, 1752–1755 (1993).

[13] B. Stébé and A. Ainane, "Ground state energy and optical absorption of excitonic trions in two dimensional semiconductors", Superlattices and Microstructures **5**, 545–548 (1989).

[14] D. D. Awschalom and J. M. Kikkawa, "Electron spin and optical coherence in semiconductors", Physics Today **52**, 33 (1999).

[15] C. Phelps, T. Sweeney, R. T. Cox, and H. Wang, "Ultrafast coherent electron spin flip in a modulation-doped CdTe quantum well", Physical Review Letters **102**, 237402 (2009).

[16] T. M. Sweeney, C. Phelps, and H. Wang, "Quantum control of electron spins in the two-dimensional electron gas of a CdTe quantum well with a pair of raman-resonant phase-locked laser pulses", Physical Review B **84**, 075321 (2011).

[17] S. O'Leary, H. Wang, and J. P. Prineas, "Coherent zeeman resonance from electron spin coherence in a mixed-type GaAs/AlAs quantum well", Optics Letters **32**, 569–571 (2007).

[18] X. Xu, B. Sun, P. R. Berman, D. G. Steel, A. S. Bracker, D. Gammon, and L. J. Sham, "Coherent population trapping of an electron spin in a single negatively charged quantum dot", Nature Physics **4**, 692–695 (2008).

[19] E. A. Zhukov, D. R. Yakovlev, M. Gerbracht, G. V. Mikhailov, G. Karczewski, T. Wojtowicz, J. Kossut, and M. Bayer, "Spin coherence of holes and electrons in undoped CdTe/(cd,mg)te quantum wells", Physical Review B **79**, 155318 (2009).

[20] L. K. Castelano, D. F. Cesar, V. Lopez-Richard, G. E. Marques, O. D. D. Couto, F. Iikawa, R. Hey, and P. V. Santos, "Zeeman splitting and spin dynamics tuning by exciton charging in two-dimensional systems", Physical Review B **84**, 205332 (2011).

[21] G. Finkelstein, H. Shtrikman, and I. Bar-Joseph, "Shakeup processes in the recombination spectra of negatively charged excitons", Physical Review B **53**, 12593–12596 (1996).

[22] A. J. Shields, M. Pepper, M. Y. Simmons, and D. A. Ritchie, "Spin-triplet negatively charged excitons in GaAs quantum wells", Physical Review B **52**, 7841–7844 (1995).

[23] G. Finkelstein, H. Shtrikman, and I. Bar-Joseph, "Negatively and positively charged excitons in $GaAs/Al_xGa_{1-x}As$ quantum wells", Physical Review B **53**, R1709–R1712 (1996).

[24] D. M. Whittaker and A. J. Shields, "Theory of $X^-$ at high magnetic fields", Physical Review B **56**, 15185–15194 (1997).

[25] A. Wójs, J. J. Quinn, and P. Hawrylak, "Energy spectra and photoluminescence of charged magneto-excitons", Physica E: Low-dimensional Systems and Nanostructures **8**, 254–259 (2000).

[26] B. Stébé, A. Moradi, and F. Dujardin, "Theoretical comparative study of negatively and positively charged excitons in $GaAs/Ga_{1-x}Al_xAs$ semiconductor quantum wells", Physical Review B **61**, 7231–7232 (2000).

[27] A. Wójs, J. J. Quinn, and P. Hawrylak, "Charged excitons in a dilute two-dimensional electron gas in a high magnetic field", Physical Review B **62**, 4630–4637 (2000).

[28] A. Dzyubenko, H. Nickel, T. Yeo, B. McCombe, and A. Petrou, "Charged magnetoexcitons in two dimensions: isolated x— and many-electron effects", physica status solidi (b) **227**, 365–379 (2001).

[29] F. M. Munteanu, Y. Kim, C. H. Perry, D. G. Rickel, J. A. Simmons, and J. L. Reno, "Crossing behavior of the singlet and triplet state of the negatively charged magnetoexciton in a $GaAs/Al_{0.55}Ga_{0.45}As$ quantum well", Physical Review B **61**, 4731–4738 (2000).

[30] G. V. Astakhov et al., "Definitive observation of the dark triplet ground state of charged excitons in high magnetic fields", Physical Review B **71**, 201312 (2005).

[31] F. Peeters, C. Riva, and K. Varga, "Trions in quantum wells", Physica B: Condensed Matter **300**, 139–155 (2001).

[32] C. Riva, F. M. Peeters, and K. Varga, "Magnetic field dependence of the energy of negatively charged excitons in semiconductor quantum wells", Physical Review B **63**, 115302 (2001).

[33] P. Redliński, "Binding energy of negative trions in a CdTe quantum well at high magnetic fields", Journal of Applied Physics **99**, 063702–063702–4 (2006).

[34] J. Z. Mezei, A. T. Kruppa, and K. Varga, "Charged exciton resonances in two and three dimensions", Few-Body Systems **41**, 233–244 (2007).

[35] A. Wójs and J. J. Quinn, "Exact-diagonalization studies of trion energy spectra in high magnetic fields", Physical Review B **75**, 085318 (2007).

[36] C. Schüller, K.-B. Broocks, C. Heyn, and D. Heitmann, "Oscillator strengths of dark charged excitons at low electron filling factors", Physical Review B **65**, 081301 (2002).

[37] D. Andronikov, V. Kochereshko, A. Platonov, T. Barrick, S. A. Crooker, and G. Karczewski, "Singlet and triplet trion states in high magnetic fields: photoluminescence and reflectivity spectra of modulation-doped CdTe□ $Cd_{0.7}Mg_{0.3}Te$ quantum wells", Physical Review B **72**, 165339 (2005).

[38] G. Bartsch et al., "Positively versus negatively charged excitons: a high magnetic field study of $CdTe/Cd_{1-x}Mg_xTe$ quantum wells", Physical Review B **83**, 235317 (2011).

[39] D. W. Snoke, "Coherence and optical emission from bilayer exciton condensates", Advances in Condensed Matter Physics **2011** (2010) 10.1155/2011/938609.

[40] L. V. Butov, "Condensation and pattern formation in cold exciton gases in coupled quantum wells", Journal of Physics: Condensed Matter **16**, R1577–R1613 (2004).

[41] C. Schindler and R. Zimmermann, "Analysis of the exciton-exciton interaction in semiconductor quantum wells", Physical Review B **78**, 045313 (2008).

[42] A. A. High, J. R. Leonard, A. T. Hammack, M. M. Fogler, L. V. Butov, A. V. Kavokin, K. L. Campman, and A. C. Gossard, "Spontaneous coherence in a cold exciton gas", Nature **483**, 584–588 (2012).

[43] S. Denev, V. Negoita, D. W. Snoke, B. Laikhtman, K. Eberl, and L. Pfeiffer, "Optical detection of magnetic fields using giant magnetoresistance in undoped coupled quantum wells", Physical Review B **66**, 205304 (2002).

[44] I. B. Spielman, J. P. Eisenstein, L. N. Pfeiffer, and K. W. West, "Resonantly enhanced tunneling in a double layer quantum hall ferromagnet", Physical Review Letters **84**, 5808–5811 (2000).

[45] J. P. Eisenstein and A. H. MacDonald, "Bose-einstein condensation of excitons in bilayer electron systems", Nature **432**, 691–694 (2004).

[46] C. Phelps, J. Prineas, and H. Wang, "Excitonic nonlinear optical response from correlation-enhanced tunneling in mixed-type GaAs quantum wells", Physical Review B **83**, 153302 (2011).

[47] H. Ibach, *Solid-state physics an introduction to principles of materials science*, in collab. with H. Lüth, 4th extensively updated and enl. ed., Advanced texts in physics (Springer, Berlin ; New York, 2009).

[48] W. A. Harrison, *Electronic structure and the properties of solids : the physics of the chemical bond* (Freeman, San Francisco, 1980).

[49] C. F. Klingshirn, *Semiconductor optics*, 4th ed., Graduate Texts in Physics (Springer, Dordrecht, 2012), 866 pp.

[50] P. Harrison, *Quantum wells, wires and dots: theoretical and computational physics of semiconductor nanostructures*, 2nd (Wiley-Interscience, Sept. 12, 2005), 508 pp.

[51] H. Haug and S. W. Koch, *Quantum theory of the optical and electronic properties of semiconductors* (World Scientific, River Edge, N.J., 2004).

[52] X. L. Yang, S. H. Guo, F. T. Chan, K. W. Wong, and W. Y. Ching, "Analytic solution of a two-dimensional hydrogen atom. i. nonrelativistic theory", Physical Review A **43**, 1186–1196 (1991).

[53] P. Dawson, I. Galbraith, A. I. Kucharska, and C. T. Foxon, "Low-power, all-optical nonlinear absorption in asymmetric double quantum wells", Applied Physics Letters **58**, 2889–2891 (1991).

[54] I. Galbraith, P. Dawson, and C. T. Foxon, "Optical nonlinearities in mixed type i–type II GaAs/AlAs multiple quantum wells", Physical Review B **45**, 13499–13508 (1992).

[55] P. Dawson and M. J. Godfrey, "Recombination dynamics of spatially separated electron-hole plasmas in GaAs/AlAs mixed type-i/type-II quantum well structures", Physical Review B **68**, 115326 (2003).

[56] A. M. Malik, M. J. Godfrey, and P. Dawson, "Tunneling of heavy holes in semiconductor microstructures", Physical Review B **59**, 2861–2866 (1999).

[57] A. Ron, H. Yoon, M. Sturge, A. Manassen, E. Cohen, and L. Pfeiffer, "Thermodynamics of free trions in mixed type GaAsAlAs quantum wells", Solid State Communications **97**, 741–745 (1996).

[58] A. Manassen, E. Cohen, A. Ron, E. Linder, and L. N. Pfeiffer, "Exciton and trion spectral line shape in the presence of an electron gas in GaAs/AlAs quantum wells", Physical Review B **54**, 10609–10613 (1996).

[59] H. W. Yoon, A. Ron, M. D. Sturge, and L. N. Pfeiffer, "Diffusion of free trions in mixed type GaAsAlAs quantum wells", Solid State Communications **100**, 743–747 (1996).

[60] M. Kozhevnikov, E. Cohen, A. Ron, H. Shtrikman, and L. N. Pfeiffer, "Comparative cyclotron resonance and luminescence study of photoexcited particles in mixed type-I–type-II GaAs/AlAs multiple quantum wells", Physical Review B **56**, 2044–2051 (1997).

[61] A. Nazimov, E. Cohen, A. Ron, E. Linder, H. Shtrikman, and L. Pfeiffer, "Interacting separately confined two-dimensional electron and hole gases: magnetic field dependence of the circularly polarized photoluminescence", Physica E: Low-dimensional Systems and Nanostructures **6**, 650–654 (2000).

[62] R. Rapaport, R. Harel, E. Cohen, A. Ron, E. Linder, and L. Pfeiffer, "Density dependent coupling of negatively charged excitons with confined photons in a GaAs/AlAs microcavity", physica status solidi (a) **178**, 481–487 (2000).

[63] T. Yeo, B. D. McCombe, B. M. Ashkinadze, and L. Pfeiffer, "Metal–insulator transition of spatially separated electrons and holes in mixed type I–type II GaAs/AlAs quantum wells", Physica E: Low-dimensional Systems and Nanostructures **12**, 620–623 (2002).

[64] M. Koch, R. Hellmann, G. Bastian, J. Feldmann, E. O. Göbel, and P. Dawson, "Enhanced energy and phase relaxation of excitons in the presence of bare electrons", Physical Review B **51**, 13887–13890 (1995).

[65] J. Sólyom, "Electrons in strong magnetic fields", in *Fundamentals of the physics of solids*, edited by J. Sólyom (Springer Berlin Heidelberg, 2009), pp. 277–327.

[66] I. D. Vagner, V. M. Gvozdikov, and P. Wyder, "Quantum mechanics of electrons in strong magnetic field", HIT Journal of Science and Engineering **3**, 5–55 (2006).

[67] S. N. Walck and T. L. Reinecke, "Exciton diamagnetic shift in semiconductor nanostructures", Physical Review B **57**, 9088–9096 (1998).

[68] L. Gor'kov and I. Dzyaloshinskii, "Contribution to the theory of the mott exciton in a strong magnetic field", Journal of Experimental and Theoretical Physics **26**, 449 (1968).

[69] I. Lerner and Y. E. Lozovik, "Mott exciton in a quasi-two-dimensional semiconductor in a strong magnetic field", Journal of Experimental and Theoretical Physics **51**, 588 (1980).

[70] Y. E. Lozovik, I. V. Ovchinnikov, S. Y. Volkov, L. V. Butov, and D. S. Chemla, "Quasi-two-dimensional excitons in finite magnetic fields", Physical Review B **65**, 235304 (2002).

[71] V. Kharchenko, "Radiative recombination of localized mott excitons in a strong magnetic field", Journal of Experimental and Theoretical Physics **56**, 1140 (1982).

[72] S. .-.-R. E. Yang and L. J. Sham, "Theory of magnetoexcitons in quantum wells", Physical Review Letters **58**, 2598–2601 (1987).

[73] G. E. W. Bauer and T. Ando, "Theory of magnetoexcitons in quantum wells", Physical Review B **37**, 3130–3133 (1988).

[74] R. L. Greene and K. K. Bajaj, "Binding energies of wannier excitons in GaAs-$Ga_{1-x}Al_xAs$ quantum-well structures in a magnetic field", Physical Review B **31**, 6498–6502 (1985).

[75] A. I. Lvovsky, B. C. Sanders, and W. Tittel, "Optical quantum memory", Nat Photon **3**, 706–714 (2009).

[76] S. E. Harris, "Electromagnetically induced transparency", Physics Today **50**, 36 (1997).

[77] M. C. Phillips, "Electromagnetically induced transparency in semiconductors", PhD thesis (University of Oregon, Dec. 2002).

[78] S. A. Crooker, D. D. Awschalom, J. J. Baumberg, F. Flack, and N. Samarth, "Optical spin resonance and transverse spin relaxation in magnetic semiconductor quantum wells", Physical Review B **56**, 7574–7588 (1997).

[79] S. O'Leary, "Coherent optical manipulation of electron spins in semiconductor nanostructures", PhD thesis (University of Oregon, Sept. 2008).

[80] D. K. Loginov, V. P. Kochereshko, A. V. Platonov, J. J. Davies, D. Wolverson, L. C. Smith, R. T. Cox, J. Cibert, and H. Mariette, "Exciton polaritons in quantum wells in a transverse magnetic field", Physics of the Solid State **51**, 1649–1655 (2009).

[81] A. B. Dzyubenko and A. Y. Sivachenko, "Charged magnetoexcitons in two-dimensions: magnetic translations and families of dark states", Physical Review Letters **84**, 4429–4432 (2000).

[82] O. Akimoto and H. Hasegawa, "Interband optical transitions in extremely anisotropic semiconductors. II. coexistence of exciton and the landau levels", Journal of the Physical Society of Japan **22**, 181–191 (1967).

[83] D. C. Mattis, *The theory of magnetism*, Corr. 2nd print., Springer series in solid-state sciences ; 17, etc (Springer-Verlag, Berlin ; New York, 1988).

[84] M. V. Durnev, M. M. Glazov, and E. L. Ivchenko, "Giant zeeman splitting of light holes in GaAs/AlGaAs quantum wells", Physica E: Low-dimensional Systems and Nanostructures **44**, 797–802 (2012).

[85] C. Phelps, "Ultrafast coherent electron spin control and correlated tunneling dynamics of two-dimensional electron gases", PhD thesis (University of Oregon, June 2011).

[86] D. J. Griffiths, *Introduction to quantum mechanics*, 2nd ed (Pearson Prentice Hall, Upper Saddle River, NJ, 2005), 468 pp.

[87] L. L. Chang, L. Esaki, and R. Tsu, "Resonant tunneling in semiconductor double barriers", Applied Physics Letters **24**, 593–595 (1974).

[88] E. E. Mendez, W. I. Wang, B. Ricco, and L. Esaki, "Resonant tunneling of holes in AlAs-GaAs-AlAs heterostructures", Applied Physics Letters **47**, 415–417 (1985).

[89] M. Remeika, J. C. Graves, A. T. Hammack, A. D. Meyertholen, M. M. Fogler, L. V. Butov, M. Hanson, and A. C. Gossard, "Localization-delocalization transition of indirect excitons in lateral electrostatic lattices", Physical Review Letters **102**, 186803 (2009).

[90] C. Latta et al., "Quantum quench of kondo correlations in optical absorption", Nature **474**, 627–630 (2011).

[91] D. Gammon, E. S. Snow, B. V. Shanabrook, D. S. Katzer, and D. Park, "Fine structure splitting in the optical spectra of single GaAs quantum dots", Physical Review Letters **76**, 3005–3008 (1996).

[92] M. Jiang, H. Wang, R. Merlin, D. G. Steel, and M. Cardona, "Nonlinear optical spectroscopy in GaAs: magnetic freezeout of excitons", Physical Review B **48**, 15476–15479 (1993).

[93] K. Sivalertporn, L. Mouchliadis, A. L. Ivanov, R. Philp, and E. A. Muljarov, "Direct and indirect excitons in semiconductor coupled quantum wells in an applied electric field", Physical Review B **85**, 045207 (2012).

[94] J. Hegarty, L. Goldner, and M. D. Sturge, "Localized and delocalized two-dimensional excitons in GaAs-AlGaAs multiple-quantum-well structures", Physical Review B **30**, 7346–7348 (1984).

[95] H. Wang, M. Jiang, and D. G. Steel, "Measurement of phonon-assisted migration of localized excitons in GaAs/AlGaAs multiple-quantum-well structures", Physical Review Letters **65**, 1255–1258 (1990).

[96] H. Tang, "Influence of interface roughness on excitonic diffusion in semiconductor quantum well", Journal of Physics: Condensed Matter **15**, 8137 (2003).

[97] D. A. Steck, *Quantum and atom optics* (available online at http://steck.us/teaching (revision 0.8.2, 6 December 2011)).

[98] M. Fox, *Optical properties of solids*, 1st (Oxford University Press, USA, Jan. 17, 2002), 318 pp.